BRNO UNIVERSITY OF TECHNOLOGY
VYSOKÉ UČENÍ TECHNICKÉ V BRNĚ

FACULTY OF MECHANICAL ENGINEERING
INSTITUTE OF SOLID MECHANICS, MECHATRONICS AND BIOMECHANICS

FAKULTA STROJNÍHO INŽENÝRSTVÍ
ÚSTAV MECHANIKY TĚLES, MECHATRONIKY A BIOMECHANIKY

COMPUTATIONAL MODELLING OF PISTON RING DYNAMICS

MASTER'S THESIS
DIPLOMOVÁ PRÁCE

AUTHOR Bc. JOZEF DLUGOŠ
AUTOR PRÁCE

BRNO 2014

BRNO UNIVERSITY OF TECHNOLOGY
VYSOKÉ UČENÍ TECHNICKÉ V BRNĚ

FACULTY OF MECHANICAL ENGINEERING
INSTITUTE OF SOLID MECHANICS, MECHATRONICS AND BIOMECHANICS

FAKULTA STROJNÍHO INŽENÝRSTVÍ
ÚSTAV MECHANIKY TĚLES, MECHATRONIKY A BIOMECHANIKY

COMPUTATIONAL MODELLING OF PISTON RING DYNAMICS

VÝPOČTOVÉ MODELOVÁNÍ DYNAMIKY PÍSTNIHO KROUŽKU

MASTER'S THESIS
DIPLOMOVÁ PRÁCE

AUTHOR
AUTOR PRÁCE
Bc. JOZEF DLUGOŠ

SUPERVISOR
VEDOUCÍ PRÁCE
doc. Ing. PAVEL NOVOTNÝ, Ph.D.

BRNO 2014

Vysoké učení technické v Brně, Fakulta strojního inženýrství

Ústav mechaniky těles, mechatroniky a biomechaniky
Akademický rok: 2013/2014

ZADÁNÍ DIPLOMOVÉ PRÁCE

student(ka): Bc. Jozef Dlugoš

který/která studuje v **magisterském navazujícím studijním programu**

obor: **Inženýrská mechanika a biomechanika (3901T041)**

Ředitel ústavu Vám v souladu se zákonem č.111/1998 o vysokých školách a se Studijním a zkušebním řádem VUT v Brně určuje následující téma diplomové práce:

Výpočtové modelování dynamiky pístního kroužku

v anglickém jazyce:

Computational Modelling of Piston Ring Dynamics

Stručná charakteristika problematiky úkolu:

Vytvořte výpočtový model pístního kroužku v Multi-body systému tak, aby dostatečně přesně popsal jeho dynamické chování. Proveďte řešení vynuceného kmitání kroužku se zahrnutím kontaktních a třecích sil včetně uvažování sil od tlaků spalin. Navrhněte další postupy ke zpřesnění výpočtových modelů.

Cíle diplomové práce:

1) Rešerše technických experimentů a výpočtových přístupů k řešení dynamiky pístních kroužků
2) Návrh výpočtového modelu pístního kroužku
3) Řešení vynuceného kmitání pístního kroužku
4) Zhodnocení výsledků
5) Závěr

Seznam odborné literatury:

[1] Andersson, P., Tamminen, J., Sandström, C. Piston ring tribology, VTT Research Notes 2178, 2002. ISBN 951–38–6107–4
[2] Macek, J. A Simple Physical Model of ICE Mechanical Losses, SAE Paper 2011-01-0610, 2011
[3] Wannatong, K. at al. Simulation Algorithm for Piston Ring Dynamics. Simulation Modelling Practice and Theory, pp. 127-146. 2008, ISSN 1569-190X
[4] Ortjohann, T. Simulation der Kolbenringdynamik auf der Basis expliziter FEM-Software, Dissetation. Aachen, 2006
[5] NOVOTNÝ, P. Virtual Engine – A Tool for Powertrain Development. Brno, 2009. Habilitační práce. VUT v Brně.

Vedoucí diplomové práce: doc. Ing. Pavel Novotný, Ph.D.

Termín odevzdání diplomové práce je stanoven časovým plánem akademického roku 2013/2014.

V Brně, dne 22.11.2013

L.S.

_____	_____
prof. Ing. Jindřich Petruška, CSc.	prof. RNDr. Miroslav Doupovec, CSc., dr. h. c.
Ředitel ústavu	Děkan fakulty

Abstract

Piston rings are installed in the piston and cylinder wall, which does not have a perfect round shape due to machining tolerances or external loads e.g. head bolts tightening. If the ring cannot follow these deformations, a localized lack of contact will occur and consequently an increase in the engine blow-by and lubricant oil consumption. Current 2D computational methods can not implement such effects – more complex model is necessary.

The presented master's thesis is focused on the developement of a flexible 3D piston ring model able to capture local deformations. It is based on the Timoshenko beam theory in cooperation with MBS software Adams. Model is then compared with FEM using software ANSYS. The validated piston ring model is assembled into the piston/cylinder liner and very basic simulations are run. Finally, future improvements are suggested.

Keywords

piston ring pack, Timoshenko beam theory, multibody system, finite element method, mechanical loss

Abstrakt

Pístní kroužky jsou instalovány do pístu a vložky válce, která nemá dokonale kruhový tvar v důsledku výrobních tolerancí a vnejšího zatížení jako například utažení šroubů hlavy motoru. Jestli se kroužek není schopen přizpůsobit těmto deformacím, nastane lokální ztráta kontaktu a následně zvýšený profuk spalin a spotřeba oleje. Současné 2D výpočtové metody nedokáží implementovat tyto efekty – více komplexní model je nevyhnutelný.

Předkládaná diplomová práce je zaměřená na vývoj 3D poddajného modelu pístního kroužku schopného zachytit lokální deformace. Ten je založený na Timoshenkové teorii prutů v kooperaci s MBS softwarem Adams. Model je následně porovnaný se softwarem ANSYS využívající metodu konečných prvků. Ověřený model pístního kroužku je vložený do sestavy píst/vložka válce a jsou provedeny základní simulace. Nakonec jsou navrhnuty další zlepšení.

Klíčová slova

sada pístních kroužků, prutová teorie podle Timoshenka, multi-body systém, metoda konečných prvků, mechanické ztráty

DLUGOŠ, J. *Computational Modelling of Piston Ring Dynamics*: master's thesis. Brno: Brno University of Technology, Faculty of Mechanical Engineering, Institute of solid mechanics, mechatronics and biomechanics, 2014. 104 p. Supervised by doc. Ing. PAVEL NOVOTNÝ, Ph.D.

Declaration

I declare that I have written my master's thesis on the subject of *Computational Modelling of Piston Ring Dynamics* independently, under the guidance of the master's thesis supervisor and using the technical literature and other sources of information which are all quoted in the thesis and detailed in the list of literature at the end of the thesis.

Brno 22. May 2014

.....

Bc. Jozef Dlugoš

Acknowledgement

I would like to honestly express my gratitude to my supervisor doc. Ing. Novotný Pavel Ph.D. for time and patience, he invested in me. I also want to thank my mom, who have always supported me throughout my studies. One great thanks belongs to my friends for making last few years at the University unforgettable. Last of all, I thank God for guidance.

CONTENTS

LIST OF FIGURES

LIST OF TABLES

INTRODUCTION

A piston ring is a split ring used in internal combustion engines to fulfill three main functions:

- seal the combustion chamber from transferring gasses into the crankcase,
- assure the heat flow from the piston to the cylinder and
- prevent the oil, not needed for lubrication, from passing from the crankcase to the combustion chamber and to provide a uniform oil film on the cylinder bore surface.

The piston rings have to meet all the requirements of a dynamic seal for linear motion that operates under demanding thermal and chemical conditions. In short, the following requirements for piston rings can be identified [1]:

- low friction, for supporting a high power efficiency rate,
- low wear of the ring, for ensuring a long operational lifetime,
- low wear of the cylinder liner, for retaining the desired surface texture of the liner,
- emission suppression, by limiting the flow of engine oil to the combustion chamber,
- good sealing capability and low blow-by for supporting the power efficiency rate,
- good resistance against thermo-mechanical fatigue, chemical attacks and hot erosion and
- reliable operation and cost effectiveness for a significantly long time.

As usual, many of above listed requirements are contradictory. Therefore the piston rings have to be optimized for a specific application in terms of sealing ability, low friction and system wear since the dynamics of the engine, and its subgroup piston rings as well, have significant impact on today's biggest concerns – economy and ecology.

Fig. 1: Typical ring pack for internal combustion engine [2]

MOTIVATION

For cars, manufacturers are obliged to ensure that their new car fleet does not emit more than an average of 130 gCO_2/km by 2015 and 95 gCO_2/km by 2020. Last limits were 160 gCO_2/km in 2007 and 135.7 gCO_2/km in 2011. In terms of fuel consumption, the 2015 target is approximately equivalent to 5.6 l/100km of petrol or 4.9 l/100km of diesel. The 2020 target equates to approximately 4.1 l/100km of petrol or 3.6 l/100km of diesel [3].

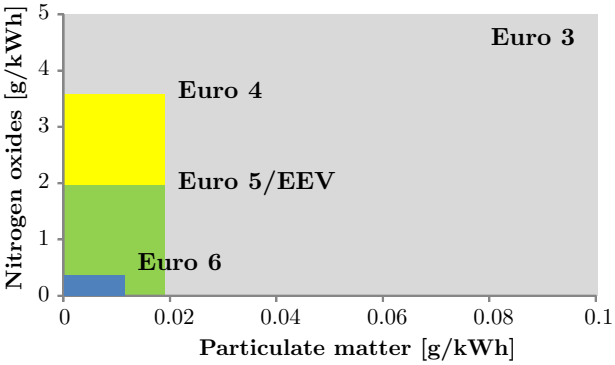

Fig. 2: Emission restrictions [4]

Mechanical efficiency (ratio of output power to power, transformed into work from the fuel thermal energy) of gasoline engines ranges from 0.75 to 0.92 and for diesel engines from 0.70 to 0.87. The biggest portion of engine mechanical losses can be linked to the piston assembly (Fig. 3) due to the friction forces between piston/cylinder liner and piston ring pack/cylinder liner. The primary benefit of friction reduction is obvious, less fuel consumption and hence reduction of CO_2 emissions.

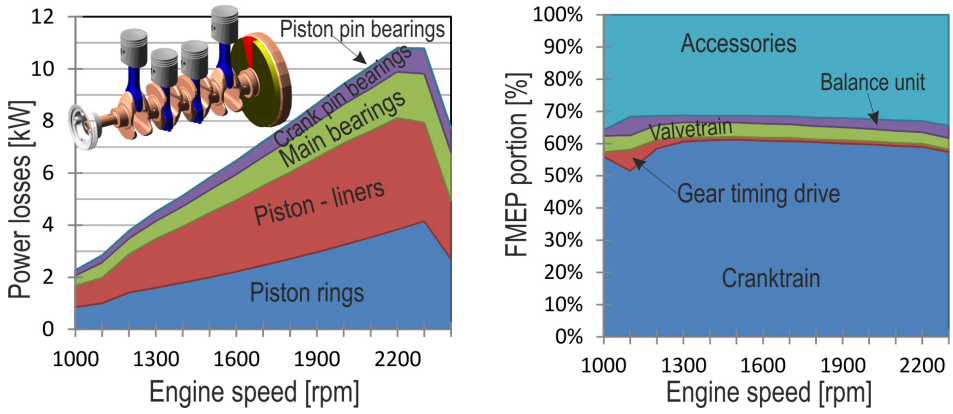

Fig. 3: Mechanical loss contribution in a 4.2L diesel engine [5]

Current research offers these methods for mechanical loss investigation:

- empirical – depends on the specific engine and cannot be used in general, may lose essential principles of the observed phenomenon,
- experimental – trial and error method, very time and money consuming,
- computational – can be very complicated especially for the early stage of design,
- others – simplified model with calibration based on the measured data.

For the best results, the issue has to be understood absolutely perfectly. Computational models with a sufficient level of simplification can clarify the essence of certain principles of piston ring dynamics. The development of such models is initially difficult, but once it is done, it can solve very general problems for various applications.

FORMULATION OF PROBLEMS AND GOALS

Novotny et al. at the Institute of Automotive Engineering Brno University of Technology have developed a 2D computational model of piston ring dynamics [33]. It is unable to describe the piston ring non axisymmetric deformation and motion, because the piston ring is represented by a planar cross section area. In addition, the cylinder liner is considered axisymmetric as well. A real cylinder liner shape depends on the size and location of tolerances, on the assembling procedure (tightening of the head bolts etc.) or on thermal expansion. The current piston ring model cannot take into account these aspects. The automotive community is pushing engineers to have more complex models, which could describe piston ring dynamics more accurately – 3D model is inevitable.

Main goals are :

- to study state-of-the-art experimental and computational modeling of piston ring dynamics,
- to develop a computational model of a piston ring,
- to solve the forced vibration of the piston ring,
- to present and explain the results,
- to propose additional improvements.

1 PISTON RING FUNDAMENTALS

1.1 Piston ring history

The first need for minimizing the fluid leakage between the piston and the cylinder bore occurred in many types of machinery, water pumps, combustion engines, air compressors, hydraulic motors, hydraulic pumps and others. In the early steam engines no piston rings were used. The temperatures and the steam pressures were not so high. Increasing power demands required higher temperatures, which caused stronger heat expansion of the piston material. Initial attempt to make an extremely narrow gap resulted in very low efficiency. The solution was found in isolating the sealing function and making a separate element – the piston ring – that could better conform to the contact surface of the cylinder bore or cylinder liner. The very first piston ring was made of rope and assembled into a steam engine in 1774 – thermal efficiency increased to 1.4 %. It had the sole task of sealing off the combustion chamber, thus preventing the combustion gases from trailing down into the crankcase. This development increased the effective pressure on the piston [6].

Ramsbottom [7], [8] and Miller [9] were among the pioneers to investigate the behavior of the piston rings in steam engines. Ramsbottom, in 1854, constructed a single-piece, metallic piston ring. The free diameter of the ring was 10 % larger than the diameter of the cylinder bore. When fitted in a groove in a piston, the ring was pressed against the cylinder bore by its own elasticity. The previous piston rings had consisted of multiple pieces and with springs to provide an adequate sealing force against the cylinder bore. Miller, in 1862, introduced a modification to the Ramsbottom ring. This modification consisted of allowing the steam pressure to act on the backside of the ring, hence providing a higher sealing force. This new solution enabled the use of more flexible rings, which conformed better to the cylinder bore.

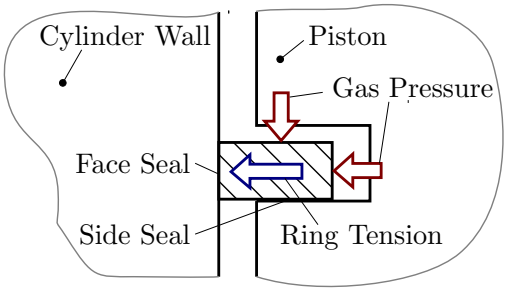

Fig. 1.1: Piston ring general function

1.2 Piston ring design

As said above, piston rings are metallic seals which have the function of sealing the combustion chamber from the crankcase and assuring the flow of heat from the piston to the cylinder. Other functions are to prevent the oil not needed for lubrication from passing from the crankcase to the combustion chamber and to provide a uniform oil film on the cylinder bore surface. To achieve this, the piston rings must be in contact with the cylinder wall and the piston groove side. Radial contact is achieved by means of the inherent elastic force of the ring, by means of the external spring integrated in the piston ring or by gas pressure acting on the back side of the piston ring. Piston rings are categorized into three basic types:

- compression rings,
- scraper rings and
- oil control rings.

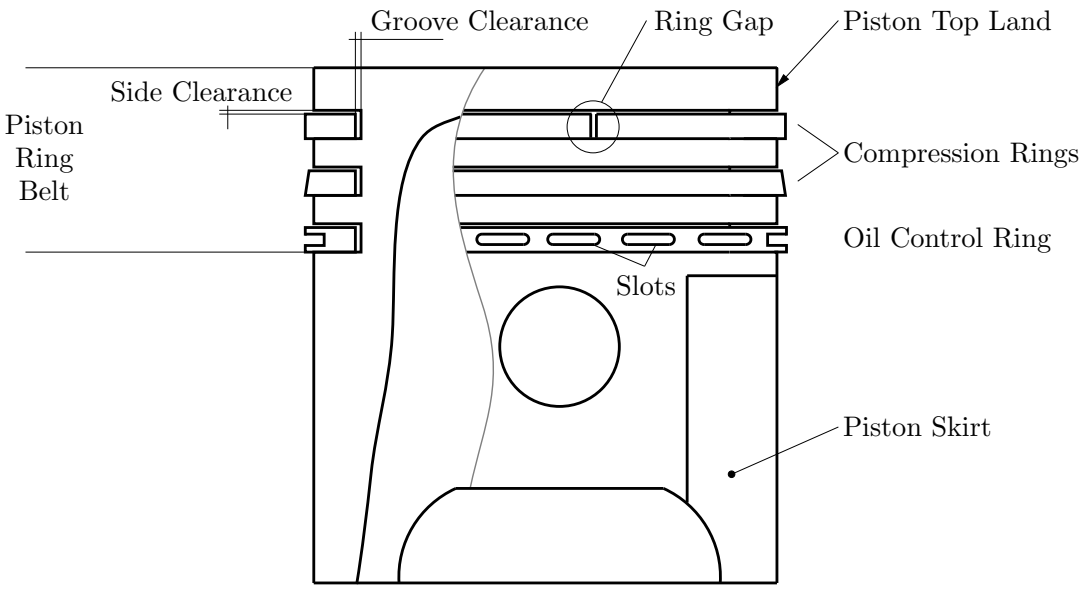

Fig. 1.2: Piston and piston ring (reprint from [1])

The piston rings form a ring pack, which usually consists of 2-5 rings, including at least one compression ring. The number of rings in the ring pack depends on the engine type, but usually comprises 2-4 compression rings and 0-3 oil control rings (two-stroke spark-ignited engines do not have an oil control ring because they have lubrication mixed in the fuel).

1.2.1 Compression ring

The main function of the compression ring is to create a seal between the piston and the liner wall, preventing the combustion gases from trailing down to the crankcase. The rings have a certain pretension, i.e. they have a larger free diameter than the cylinder liner, which assists the ring in conforming to the liner. The cylinder gas pressure acts on the back-side of the ring, especially on the top ring, pressing it against the liner.

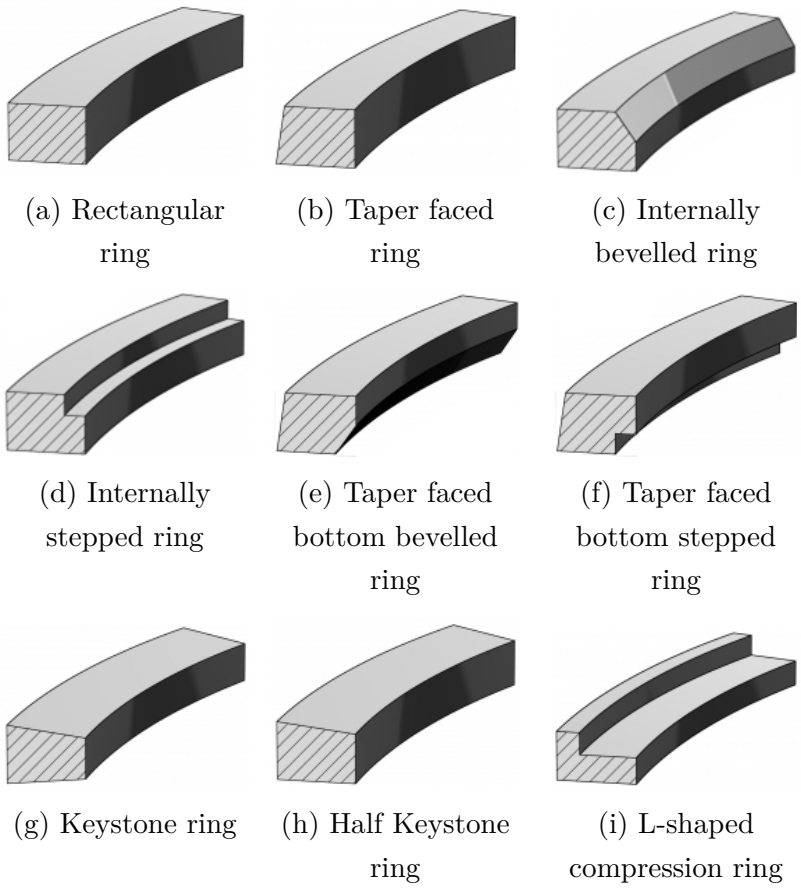

(a) Rectangular ring (b) Taper faced ring (c) Internally bevelled ring

(d) Internally stepped ring (e) Taper faced bottom bevelled ring (f) Taper faced bottom stepped ring

(g) Keystone ring (h) Half Keystone ring (i) L-shaped compression ring

Fig. 1.3: Compression ring designs [13]

The most basic piston ring is rectangular shaped (Fig. 1.3a). This ring performs the necessary sealing functions under normal operating conditions and due to its simplicity it is used for all computations in this master's thesis. The bevel or step made on the top side of the piston ring will cause the ring to twist positively and oppositely, the bottom side results in a negative twist (Fig.1.4) [10], [11]. The L-shaped ring was used in 2-stroke engines, in some cases it has been installed in automotive diesel engines in order to minimize the crevice volume in the combustion chamber [12].

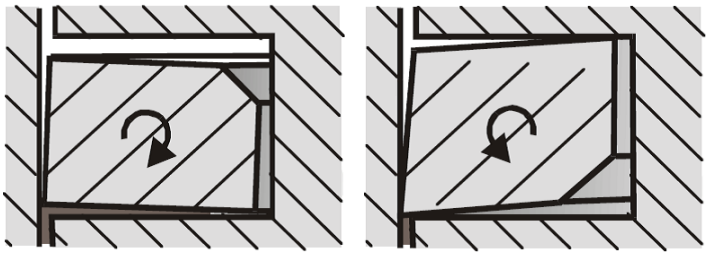

(a) Positive (b) Negative

Fig. 1.4: Piston ring twist [14]

1.2.2 Scraper ring

The scraper ring has the task of sealing and scraping off the oil from the liner wall. Therefore practically all of this type of rings are with a step recessed into the bottom outer face - beak. This assures an extremely effective oil scraping, by increasing the unit pressure and causing a positive twist. The volume created by the beak is beneficial in allowing large amounts of oil to be stored there. This means that the favourable characteristics of a ring with a stepped bottom outer edge can be adjusted by varying the size of the step. Rings with a beak have a higher oil scraping effect than taper faced rings, but this is usually coupled with higher blow-by (section 1.7).

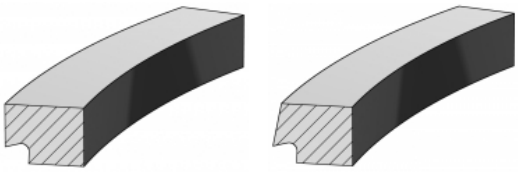

(a) Napier Ring (b) Taper Faced Napier Ring

Fig. 1.5: Scraper Ring designs [13]

1.2.3 Oil control ring

A proper lubricant film on the piston, piston rings and cylinder wall is required in order to prevent damage and reduce friction. The oil control rings are specially designed to appropriately distribute the oil on the cylinder liner and to scrape off surplus oil to be returned to the crankcase.

Since the oil control ring has the lowest pressure on its back side (Fig. 1.6), the contact pressure is mainly caused by the tangential (pretension) force from inherent inner tension – single-piece – or by an additional self-supporting spring -multi-piece oil control ring.

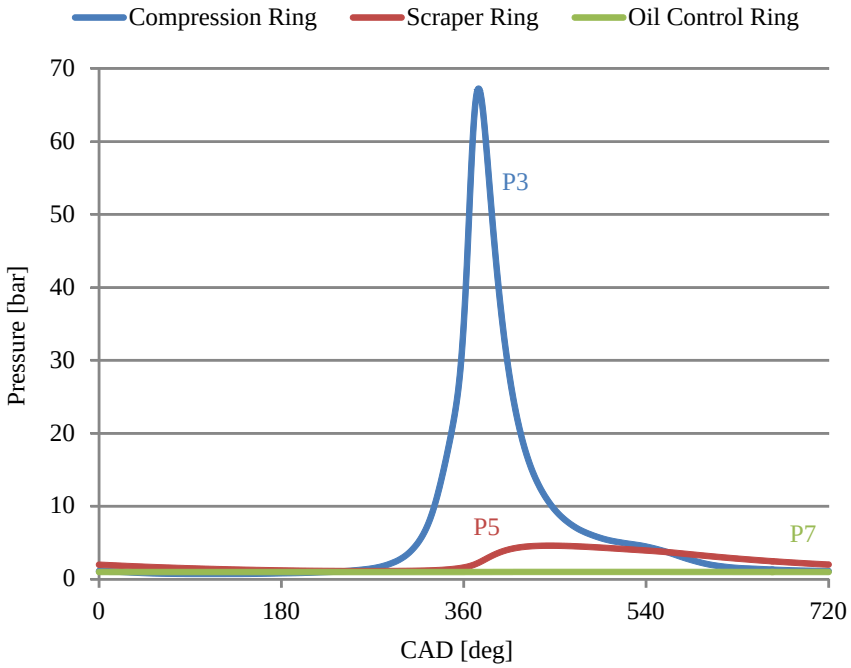

Fig. 1.6: Pressure on the back side of the rings

For example, the theoretical contact pressure used in the calculation of the tangential forces of rectangular and half Keystone compression rings made of steel is approximately 0.19 Nmm^{-2}. In the case of coil-spring-loaded oil control rings, the pressure is approximately 1 Nmm^{-2} [15]. The values of nominal contact pressures and specific tangential forces for various piston rings are tabulated in the standards ISO 6621...6626 (ISO 6621-4) [1].

Another characteristic of oil control rings that is at least as important as the contact pressure at the running face is their ability to conform to the bore distortions of an engine – highly flexible rings (i.e. rings with a low moment of inertia across the wall thickness) with sufficient unit pressure needed. Multi-piece oil control rings have much more conformability than single-piece ones.

The three-piece oil control rings consist of two thin steel rings, known as rails (segments), and anexpander – spacer – which holds the rails at the required relative axial distance while simultaneously pressing them against the cylinder wall (Fig. 1.8). For further information find [13], where the ring joints and joint notches are also described.

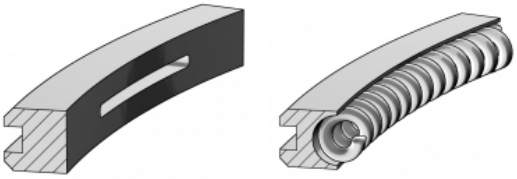

(a) Single-piece oil control ring (b) Two-piece oil control ring

Fig. 1.7: Oil control ring designs [13]

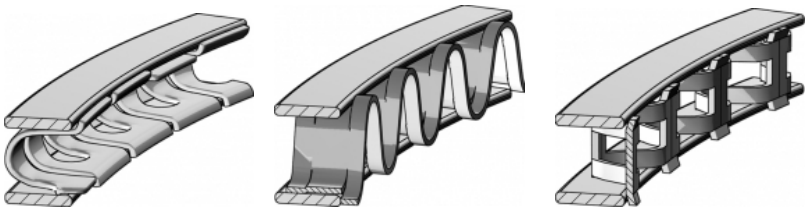

(a) VF System (b) MF System (c) S S50 System

Fig. 1.8: Three-piece oil control ring designs [13]

1.2.4 Radial pressure distribution

Non-uniform radial pressure distribution is achieved by the ovality of a piston ring (section 1.3.2). A constant characteristic and a piston ring with positive ovality (Fig. 1.9a and Fig. 1.9b) are used in 4-stroke engines. Piston rings with negative ovality (Fig. 1.9c) are common in 2-stroke engines due to a lower radial contact pressure that allows the pass of the ring end gap by the exhaust and inlet ports.

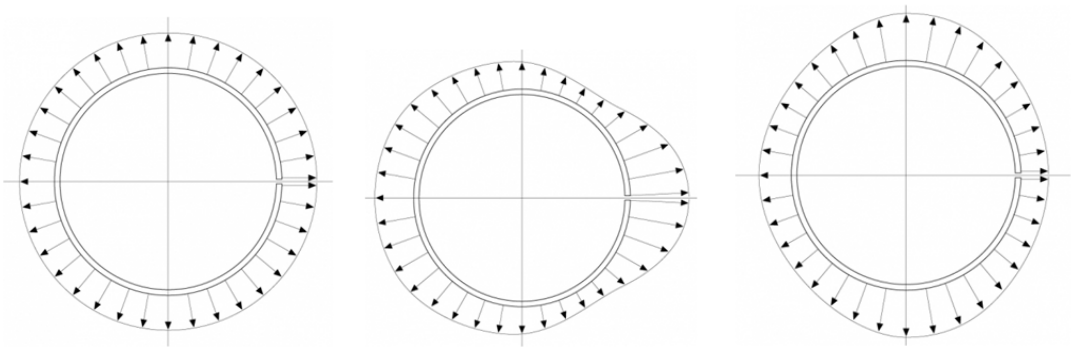

(a) Constant characteristic (b) Four-stroke characteristic (c) Two-stroke characteristic

Fig. 1.9: Different radial pressure distributions [13]

1.3 Piston ring parameters and relationships

The ring is pressed against the cylinder wall under a contact pressure p. The measurement of the contact pressure is extremely difficult. Therefore, in practice it is calculated from the tangential force F_t. This is the force which, when applied tangentially to the ends of the ring, is sufficient to compress the ring to the specified closed gap.

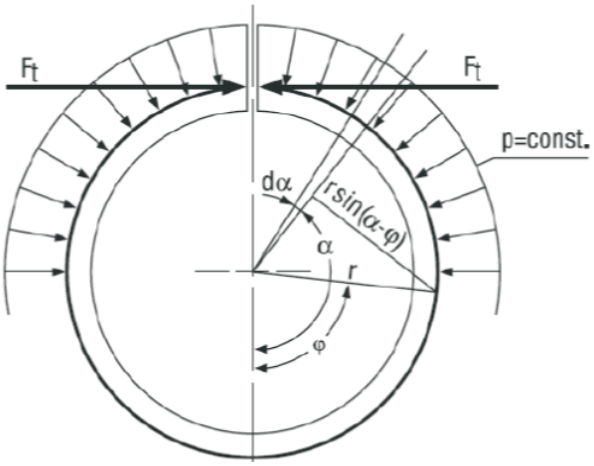

Fig. 1.10: Relantion between constant contact pressure and tangential force

By solving the internal forces and moments, the following expressions are obtained:

$$M = phr^2(1 + cos\varphi) \tag{1.1}$$

$$M = F_t r(1 + cos\varphi) \tag{1.2}$$

where M is the bending moment and h is the axial width (Fig. 1.11). By comparing the bending moment of the constant contact pressure (1.1) against that of the tangential force (1.2), the following relationship is established

$$p = \frac{2F_t}{dh} \tag{1.3}$$

where d is the nominal diameter. The contact pressure of compression rings on account of their inherent tension generally lies between 0.12 and 0.25 Nmm^{-2} for rings conforming to DIN/ISO standard (section 1.2.3). The actual contact pressure is many times greater due to the gas pressure acting behind the ring.

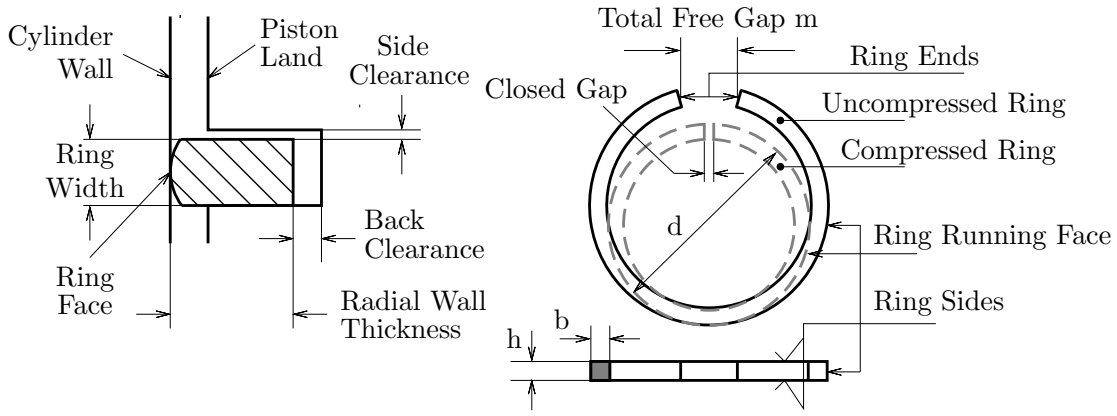

Fig. 1.11: Piston ring nomenclature

The cylinder wall, where the piston rings are installed, does not have a perfect round shape due to machining tolerance or the assembly and working loads causing deviations from the circular shape. If the ring cannot follow these deformations, a localized lack of contact will occur and consequently an increase in the engine blow-by and lubricant oil consumption.

1.3.1 k parameter

Some of the factors affecting the ring capacity to conform to a deformed bore are included in the k parameter also called the conformability coefficient and the piston ring parameter.

$$k = \frac{F_t(d-b)^2}{4EJ} \tag{1.4}$$

where E is the modulus of elasticity and J is the moment of inertia of the ring cross section. The k parameter is often used as a function of the total free gap for rectangular section rings

$$k = \frac{2}{3\pi}\frac{m}{d-b} \tag{1.5}$$

A higher k value means a higher ring conformability – ability to conform to a deformed cylinder wall. The usual k values for compression rings are between 0.02 and 0.04, oil rings have a higher k (up to 1.00 in some two-piece oil rings).

1.3.2 Ring ovality parameter

It is used to represent the contact pressure distribution of the ring. The piston ring is closed by a flexible steel band and the ring ovality is the difference between the diameter through the gap and the diameter at 90 deg from the gap (Fig. 1.12). A positive ovality indicates a higher pressure through the gap axis and a negative ovality the opposite (Fig. 1.9).

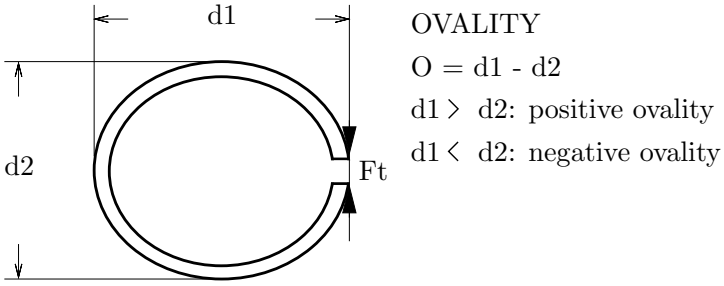

Fig. 1.12: Piston ring ovality (reprint from [16])

For more information about the piston ring conformability see paper [16], where simple conformability criteria were verified by the experimental measurements and a new semi-empirical criterion was proposed. Basic expressions with brief notes are also available in [13].

1.4 Piston ring material

The piston ring materials have to meet tough demands – strength at a high temperature, low tangential force decrease due to temperature or fatigue, corrosion resistance, good thermal conductivity (for good heat transferability to the cylinder wall) and also good sliding characteristics for operation in normal and dry lubrication conditions - in order to withstand the thermal and mechanical loads during the running conditions (section 1.5). Ring materials are selected from cast irons and steels according to the stated stresses and their use as compression or oil control rings. Besides steel materials, the grey (flake graphite) or ductile (nodular graphite) cast irons are used in a non-heat-treated condition or hardened and tempered state. The advantage of cast irons is in their graphite phase which can act as an oil reservoir that supplies oil at dry starts or in similar conditions of oil starvation. On the other hand the steel piston rings have better mechanical characteristics, but for proper function the coating is mandatory. Detailed information about coatings can be found in [1], [17] and each piston ring material application is available in [13].

1.5 Piston ring mechanics

The ring motion and ring twist about the ring center affect the operation of the ring, the oil film formation and the friction between the ring and the liner, the wear of the ring and cylinder liner, and the blow-by across the ring pack [1].

1.5.1 Piston ring primary motion – kinematics

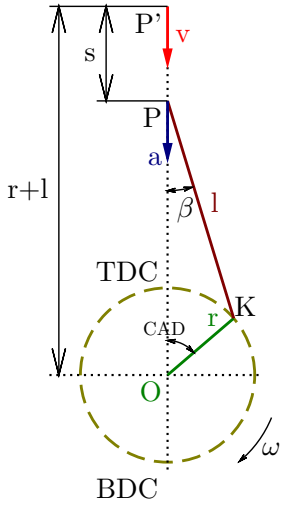

Fig. 1.13: Crank mechanism model

The piston ring primary motion is defined by the motion of the piston. First of all, it is the reciprocating motion along the cylinder axis. It is well described by the crank mechanism (Fig. 1.13). Equation construction for the wrist pin displacement, using the crank parameters followed by the application of the binomial theorem, lead to the expression:

$$s(\alpha) = r\left(1 - cos\alpha + \frac{\lambda}{4}\left(1 - cos\left(2\alpha\right)\right)\right) \tag{1.6}$$

where r is a half of the stroke, l is the rod length and λ is the half of stroke to rod ratio defined as $\frac{r}{l}$. The velocity and acceleration are obtained as the first and the second derivative of the displacement (1.6):

$$v(\alpha) = r\omega\left(sin\alpha + \frac{\lambda}{2}sin2\alpha\right) \tag{1.7}$$

$$a(\alpha) = r\omega^2\left(cos\alpha + \lambda cos2\alpha\right) \tag{1.8}$$

Another motion of the piston is made up of the translation perpendicular to the cylinder and the piston pin axis (usually called the piston lateral motion), and rotation about the piston pin axis (usually called the piston tilt). It is the most important source of mechanically induced noise [18].

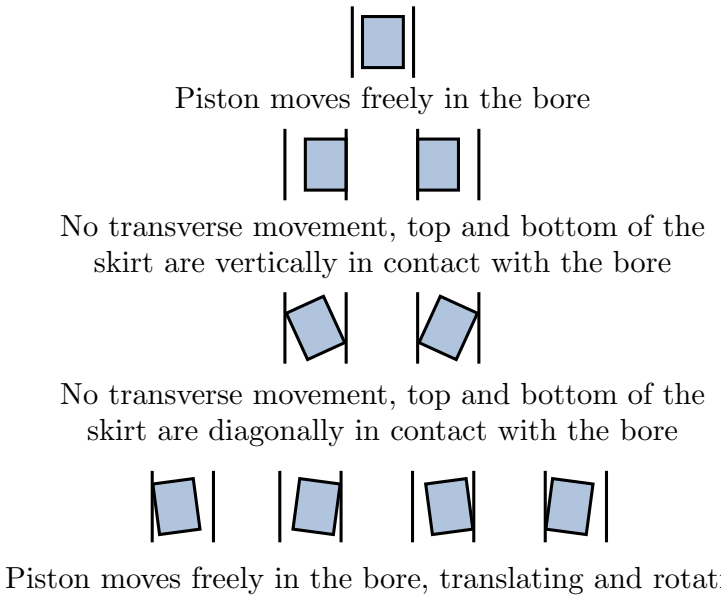

Fig. 1.14: Basic modes of piston motion in the bore (reprint from [18])

1.5.2 Piston ring secondary motion – dynamics

During an engine cycle, the ring is subjected to different kinds of loads changing over time (Fig. 1.15):

- gas pressure loads due to pressure difference,
- inertia loads due to piston acceleration and deceleration,
- friction loads due to ring contact with the cylinder liner,
- hydrodynamic forces and oil damping forces,
- forces due to asperities contacts,
- tangential forces due to the pretension of the ring,
- contact forces between the piston ring and the piston.

The elastic distortion of the piston and liner can affect the effective geometry of the ring face and cylinder liner contact, which causes a non-uniform distribution of the contact pressure between the cylinder liner and the piston ring face and can thus lead to increased blow-by and oil consumption [15].

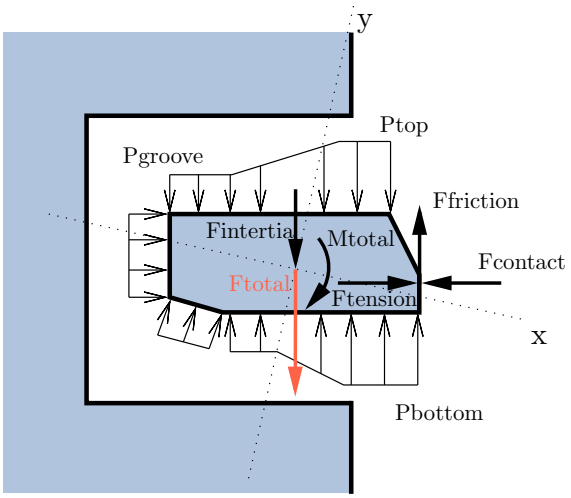

Fig. 1.15: Forces acting on the ring (reprint from [1])

1.5.3 Piston ring thermal load

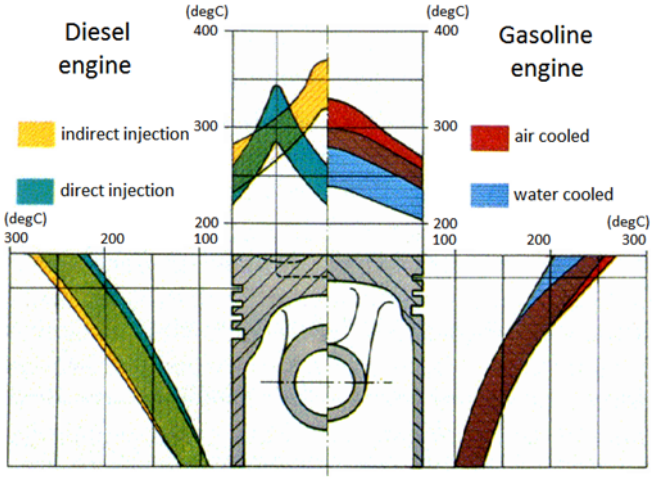

Fig. 1.16: Piston temperature distribution [19]

The most thermally affected areas of the piston are the piston deck and the top land. Peak gas temperatures in the combustion chamber are in the interval between 2000 and 2500 °C according to different engines types [17]. The main portion of the piston heat is transferred by conduction through the piston rings, the piston ring lands and the piston skirt into the cylinder wall and coolant. The piston is especially designed to keep the temperatures in the top ring groove bellow 220 °C for mineral oil or bellow 240-260 °C for synthetic oil. Otherwise, oil coking is very likely to

happen. During this effect, the oil changes its state from a fluid to a more solid state and constrain the piston ring motion so it will lose functionality – increase in blow-by, oil consumption seen as a black smoke from the exhaust and overheating of the piston due to insufficient thermal flux via the contact of the piston ring and the cylinder wall.

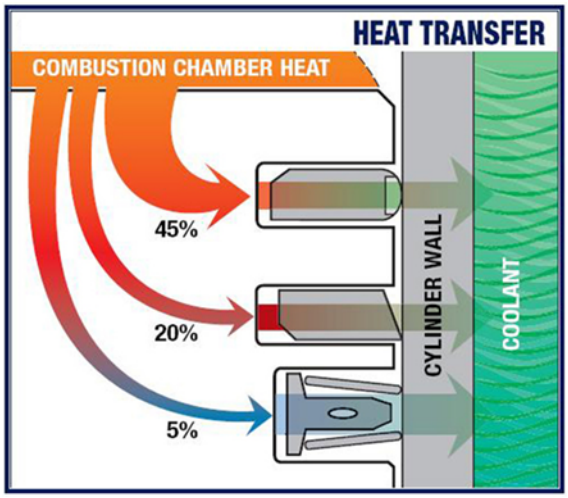

Fig. 1.17: Piston cooling via piston rings [20]

1.6 Piston ring friction

Friction is defined as a resistance against the relative movement of contacting surfaces. Contact occurs directly (contact between solids – asperity contact), indirectly (lubrication) or by a combination of both in the case of mixed friction. Frictional forces are a function of material properties and physical and chemical system characteristics. Other contributory effects are the surface structures, manifested by the ring running face contour, the roughness, and the deviation from the ideal cylinder shape. These structures do not have full-face contact, so the local contact pressures diverge significantly from the specific contact pressure. In the presence of contact and mixed friction, wear mechanisms occur which are accompanied by a loss of energy. Frictional heat can reach very significant levels locally and may trigger material damage which can result in the failure of tribological systems (scuffing, seizure) [13], [21].

The Stribeck diagram depicts the relation between the friction coefficient C and other variables, defining tribological conditions, like:

- Sommerfeld numbers So as:

$$So = \frac{\eta n}{P} \tag{1.9}$$

where η is the dynamic viscosity, n is the rotational speed and P is the nominal pressure. Or:

$$So = \frac{\eta u}{Ph} \tag{1.10}$$

where u is the instantaneous piston velocity and h is the ring width (Fig. 1.11). Or:

$$So = \frac{|F_N|}{\eta u h} \tag{1.11}$$

where F_N is the normal loading force. Since the Sommerfeld number is the characteristic dimensionless number, countless others can be easily made and the choice depends only on the available Stribeck diagram for the current application.

- Thickness ratio λ [22]:

$$\lambda = \frac{effective\ film\ thickness}{surface\ roughness} \tag{1.12}$$

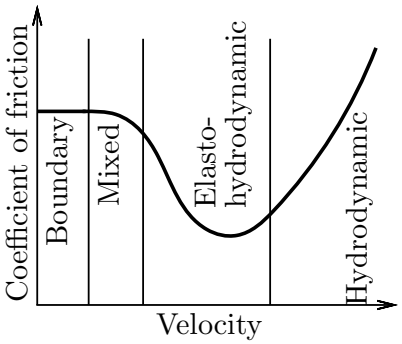

Fig. 1.18: Stribeck diagram for coefficient of friction-velocity relantion

In addition, the Stribeck curve demarcates different lubrication regimes like shown in the Fig. 1.18 – boundary, mixed, elastohydrodynamic and hydrodynamic. It is generally accepted that piston rings operate under hydrodynamic lubrication throughout most of the engine cycle. However, it is equally clear that the adverse conditions encountered near the reversal points will lead to very thin films and a transition from full-film to mixed or boundary lubrication. The operation of the piston rings in the mixed or boundary lubrication regime for a small portion of the engine cycle can have a disproportionate effect upon ring friction, and hence a power loss in the engine [23].

1.7 Blow-by

Blow-by is the unwanted effect when the gases travel from the combustion chamber into the crankcase. Blow-by negatively affects the engine efficiency and contaminates the lubricant. It cannot be totally prevented, only minimized. It can flow through:

- the piston ring gap (Fig. 1.19a) – due to essence of it's function it cannot be prevented,
- past the front side of the piston ring at starved lubrication conditions (Fig. 1.19b) – nonstandard situation,
- past the back side of the piston ring (Fig. 1.19c) – due to piston ring motion inside the piston groove.

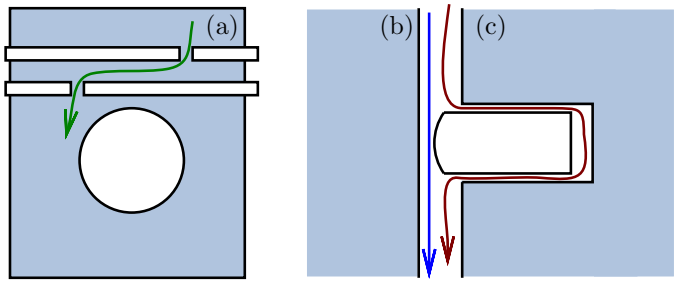

Fig. 1.19: Blow-by ways

1.8 Oil consumption

Another negative phenomenon observable mainly in the older combustion engines. Oil consumption, caused by the piston rings, has three different mechanisms as well:

- oil evaporates from the rings and the cylinder liner into the combustion chamber (Fig. 1.20a),
- oil is thrown off from the ring due to inertia (Fig. 1.20b),
- gas blowing back towards the combustion chamber entrains oil from the ring pack (Fig. 1.20c).

Since environmental regulations are becoming even stricter regarding the exhaust emissions of internal combustion engines, the oil flow into the combustion chamber has to be reduced. For further information see [25], [26] or [27].

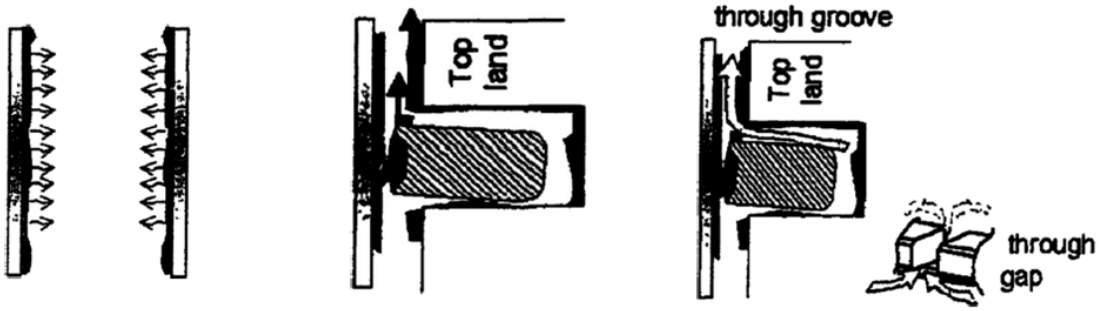

(a) (b) (c)

Fig. 1.20: Oil consumption phenomena [24]

2 PISTON RING DYNAMICS – – STATE-OF-THE-ART

2.1 Empirical

The purely empirical regression models aim to estimate the overall friction mean effective pressure (FMEP), making use of few global variables, one typically related to the engine load and the other related to the engine speed, in order to separately account both the energy dissipated by friction due to gas thrust and the energy losses influenced by the speed (e.g. those related to inertia forces). They are too dependent on a specific engine design, which was used for their initial development.

2.1.1 Original and modified Chen & Flynn model

One of the most common friction model encountered in literature and employed in commercial software is known as the Chen & Flynn model with four constants [42] according to which, the friction mean effective pressure (FMEP) depends on in-cylinder maximum pressure and engine speed by means of the following law:

$$FMEP = A + Bp_{max} + Cn + Dn^2 \tag{2.1}$$

where A and B are constants representing the maximum in-cylinder pressure p_{max}, C and D are constants related to the engine speed n. Constants A, B, C and D are determined by data fitting performed on the experimental values obtained at the engine test bed.

Pipitone [43] observed 4cylinder SI 1.2L engine fuelled with compressed natural gas (CNG). After the first series of tests, running the engine without load at different speeds, the constants C and D were estimated. A second series of tests were performed to determine the value of the constant A and B, running the engine on many different operative conditions of speed, load and spark advance. Hence, using an optimization procedure, the constants were fixed minimizing the maximum percentage error of the Chen & Flynn model (2.1) with respect to the experimental data.

It was found a bad matching between the model prediction and the experimental data for higher FMEP values. As mentioned in Tab. 2.1, the maximum error could not be lower than 35 %, and the maximum difference between the model prediction and the real FMEP reached 0.67 bar – an insufficient correlation with the test.

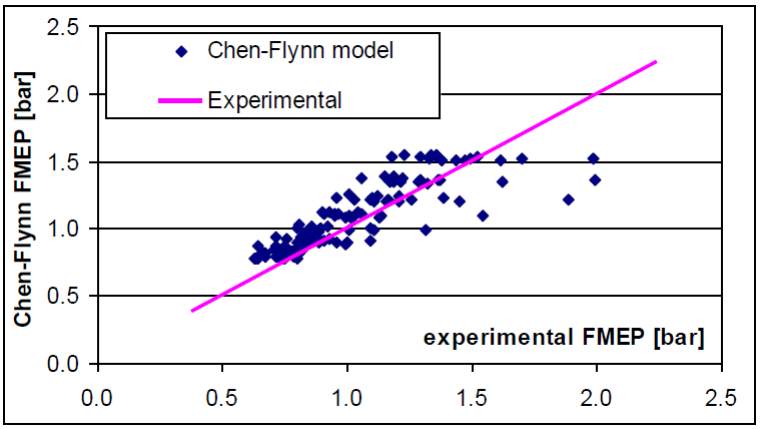

Fig. 2.1: Comparison between the Chen & Flynn model prediction and the experimental data [43]

Model	Chen-Flynn
mean % error	13 %
max % error	35 %
max error [bar]	0.668

Tab. 2.1: Overall results of the Chen & Flynn model [43]

A further attempt has been made trying to use up to a 3^{rd} order polynomial to account for the load factor, thus introducing the p^2_{max} and p^3_{max} terms; the equation (2.1) then becomes:

$$FMEP = A + Bp_{max} + Cp^2_{max} + Dp^3_{max} + En + Fn^2 \tag{2.2}$$

The result of the fitting however still showed an unsatisfying prediction: as listed in Tab. 2.2, the equation (2.2) is unable to provide a better FMEP evaluation than the original Chen & Flynn model (equation (2.1)); the attempt to obtain a better correlation with the load factor p_{max} by introducing the higher order terms p^2_{max} and p^3_{max} was revealed to be useless. Pipitone [43] also tried to adopt, in place of the maximum in-cylinder pressure, other load-linked variables, such as the manifold absolute pressure (MAP) or the indicated mean effective pressure (IMEP), but both attempts were revealed to be vain.

A deeper analysis of the experimental data was then carried out, aiming for a better understanding of the variables that really influence the FMEP. Pipitone [43] hence tried to express the load term of the friction model using as "load variable" the

Model	Chen-Flynn with p^2_{max} p^3_{max}
mean % error	13 %
max % error	33 %
max error [bar]	0.619

Tab. 2.2: Overall results of the equation (2.2) [43]

location of the pressure peak (LPP) instead of the p_{max}, using a 3^{rd} order polynomial; moreover, observing that the LPP effect is amplified by the engine speed, he decided to adopt the following formulation:

$$FMEP = A + FMEP_n + \frac{n}{1000}\left(aLPP + bLPP^2 + cLPP^3\right)$$
$$FMEP_n = Cn + Dn^2 \tag{2.3}$$

where $FMEP_n$ represents the speed related contribution to the friction losses. The calibration of the new friction model requires the determination of the constants A, a, b and c, (C and D being already fixed) which has been carried out minimizing the maximum percentage error with respect to the experimental data: the results obtained, shown in the graphs of Fig. 2.2 revealed the new model to have a better consistency with the experimental data than the original Chen & Flynn model (Fig. 2.1). Moreover, as exposed in Tab. 2.3, all evaluated errors reduced to a half of those obtained with the original Chen & Flynn model (Tab. 2.1).

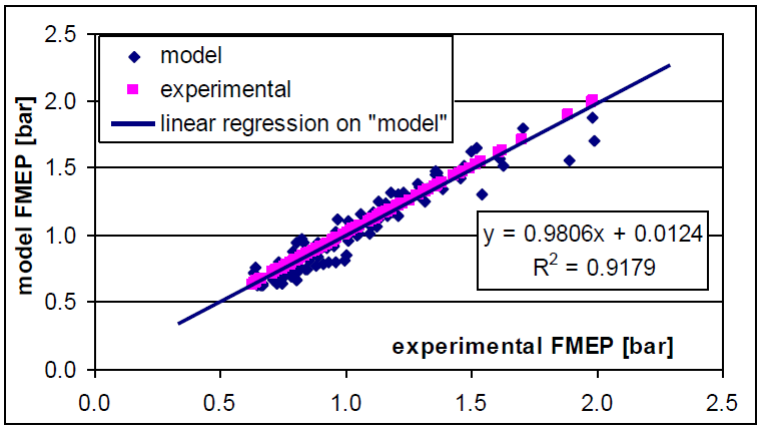

Fig. 2.2: Comparison between the new FMEP model prediction and the experimental data [43]

Model	based on LPP
mean % error	6 %
max % error	18 %
max error [bar]	0.336

Tab. 2.3: Overall results of the new FMEP model [43]

Pipitone [43] claims that p_{max} tends to have very little importance. It then can be concluded that, for the engine tested, the phase of the pressure cycle affects the friction losses more than the maximum pressure: the more the pressure cycle is retarded, the higher the friction loss is. This observation finds confirmation in literature, where it is often reported that, among the different contributions to the FMEP, the one which seems to have the stronger effect is the friction between the piston and the cylinder walls, which, depending on the lateral thrust, reduces if the pressure cycle is advanced.

It must be pointed out, however, that, even if the new model has been developed on the basis of experimental data also involving highly retarded pressure cycles (with LPP up to 26 crank angle degree after top dead centre – CAD ATDC), it does not lose validity even if these cycles are excluded: considering, in fact, only pressure cycles with LPP lower than 20 CAD ATDC.

One can see that the results of numerous experiments resulted in the enumeration of a few constants for the specific engine to find out the total friction as FMEP. However, the final calibrated equation uses only two variables – the character of change in FMEP is observable only with variations of LPP and crank rotation n. This does not capture the essence of the friction phenomenon since it does depend on variables such as the piston ring design and dynamics, oil viscosity and temperature and much more.

Another empirical model of the crankshaft friction, valve train friction or pumping losses can be found in [45], where the comparison with experimental data is also available. An empirical model [46] is used for an approximate determination of mechanical losses of the piston rings, created on the basis of measurements taken on a specific diesel engine:

$$F_{tk} = -sign(v)C_1\sqrt{|v|}\left(1 - C_2\frac{T - T_{bez}}{T_{bez}}\right)\left(1 + C_3\frac{p - p_{bez}}{p_{bez}}\right)\left(\frac{D}{D_M}\right)^2 \tag{2.4}$$

where v is piston velocity, T is oil temperature, T_{bez} is reference oil temperature, p is combustion pressure, p_{bez} is reference pressure, D is cylinder bore, D_M is reference cylinder bore and C_1, C_2, C_3 are constants.

2.2 Experimental

2.2.1 Instantaneous IMEP method for overall friction estimation

This method is very versatile and requires minor changes in the engine. It is using in-cylinder pressure indication on firing and motored engine combined with determining the brake torque – dynamometer needed. However this method estimates only the total engine friction characterized by FMEP as the difference of the indicated mean effective pressure (IMEP) and the brake mean effective pressure (BMEP). BMEP is calculated from the engine parameters and the reaction force of the dynamometer:

$$BMEP = \frac{4\pi M_t}{xV_1} \tag{2.5}$$

where M_t is the engine torque, V_1 is the engine one cylinder displacement volume and x is the number of cylinders. In-cylinder pressure measurement is performed to get IMEP at firing and motored engine using a spark plug with an integrated pressure transducer (Fig. 2.4).

$$IMEP = \oint_{cycle} \frac{pdV}{V_1} = \oint_{cycle} \frac{p(\alpha)A_p\frac{dS}{d\alpha}}{d\alpha} \tag{2.6}$$

where V_1 is the displacement of one cylinder, p is the in-cylinder pressure sampled on an angle-based trigger and dV is the cylinder volume differential. This evaluation method brings a well-known weakness – significant sensitivity to the top dead centre (TDC) position determination, since an error of 1 CAD can cause up to a 10 % evaluation error on IMEP and a 25 % error on the heat released by the combustion: TDC position should be then known within a precision of 0.1 CAD. For example 1.2HTP 4cylinder Skoda engine needs for a 0.1 mm piston movement from TDC 4 CAD (Fig. 2.3). Works [47], [49], [49] are focused directly on this issue.

Finally the friction mean effective pressure is calculated as:

$$FMEP = IMEP - BMEP \tag{2.7}$$

FMEP characterizes the overall friction losses and therefore the losses of valvetrain, fuel injection equipment and the accessories need to be substracted from the results. This may be done by decoupling motoring method and by re-calculting the power at lubricating oil pump according to pressure drop in the lubricating system.

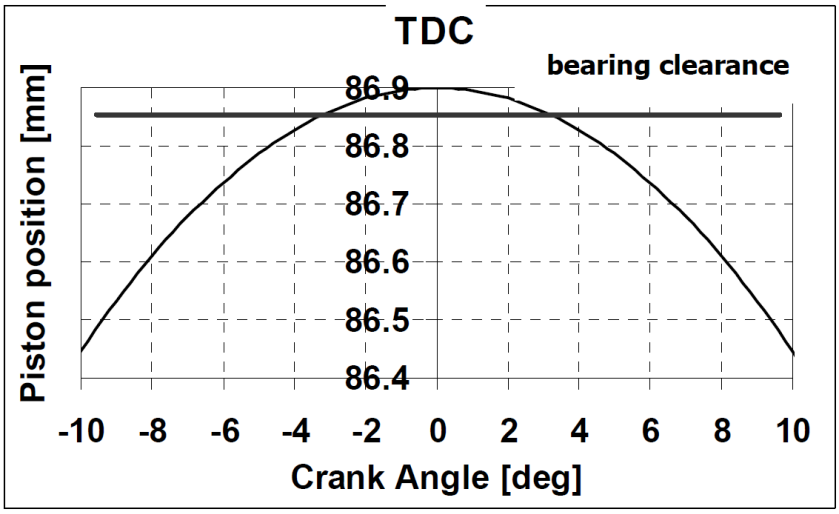

Fig. 2.3: Influence of bearing clearance to dynamics
TDC position (stroke 86.9 mm) [57]

2.2.2 Instantaneous IMEP method for piston assembly friction estimation

It is used to obtain the piston assembly friction data for both motoring and firing cases. According to Sethu et al. [50], their telemetry system provides excellent data even after 50+ hours of operation at speeds as high as 2000 rpm.

The IMEP method needs very accurate measurements of the in-cylinder gas pressure, the force transferred to the connecting rod, and the calculation of the inertial force of the piston assembly. With the knowledge of all these elements, piston assembly friction is calculated through an instantaneous force balance. The advantage of this technique is that it allows in-cylinder friction measurements to be made on production engines with relatively minor engine modifications.

The primary drawback of this technique is that the experimental error is very difficult to overcome. Without great care, the magnitude of the error associated with the measured forces can exceed the calculated in-cylinder friction forces. Consequently, highly accurate calibrations and signal processing is required. Another drawback is that it requires a telemetry system for transferring signals from the moving connecting rod. Wireless telemetry faces challenges related to signal noise and power supply, while in the case of mechanical linkage the wires that carry the strain signal out of the engine have a finite lifetime due to fatigue failure.

Engine modifications necessary for this technique include the installation of pressure transducers in the engine head (Fig. 2.4) and a telemetry system in the crankcase which is used to transmit strain gauge signals. Other minor modifications

include a slightly modified windage tray and an extended oil sump to accommodate the reciprocating motion of a four-bar linkage, which is part of the telemetry system.

Fig. 2.4: Pressure sensor Kistler 6125B [44]

A reciprocating linkage, featuring aluminum construction, is installed between the big end of the connecting rod and the lower cylinder block (Fig. 2.5). The linkage carries the strain gauge signal and the power supply wires from the connecting rod, where the strain gauge is mounted, to a small passage between the crankcase and the lower block leading out of the engine. Two strain gauges are mounted on each side of the connecting rod. The effects of elevated temperatures and strain perpendicular to the connecting rod's axis must be accounted for. Another option for measuring the connecting rod force is to use a grasshopper mechanism with the strain gauges installed like Fuente et al. [51] did on the sleeve valve engine.

Fig. 2.5: Instantaneous force balance schematic [50]

The calibration of the strain gauge signal measurement chain is critical. Therefore the calibration is done in-cylinder by pressurizing the cylinder with nitrogen gas. In order to keep the engine from turning over while the cylinder is pressurized, a locking bracket is designed and fixed to the flywheel. This set-up accurately represents the actual conditions the piston assembly will be in during engine operation. In-cylinder calibration is performed at different crank angle positions, namely TDC, 30deg ATDC and Bottom Dead Center (BDC).

The instantaneous engine speed (IES) is measured by the pulses from the crankshaft encoder to evaluate the constant engine speed assumption commonly used in the inertial force calculation. The friction force along the cylinder axis is calculated by a vector-subtracting inertial, gravity and connecting rod forces from the gas force (Fig. 2.6). The combination of gas, inertial, and gravity forces on the piston assembly is defined as the theoretical connecting rod force. This is the maximum possible force that can be transferred to the connecting rod. The difference between the theoretical and the measured connecting rod force is friction between the piston assembly and cylinder liner, the piston pin friction is neglected.

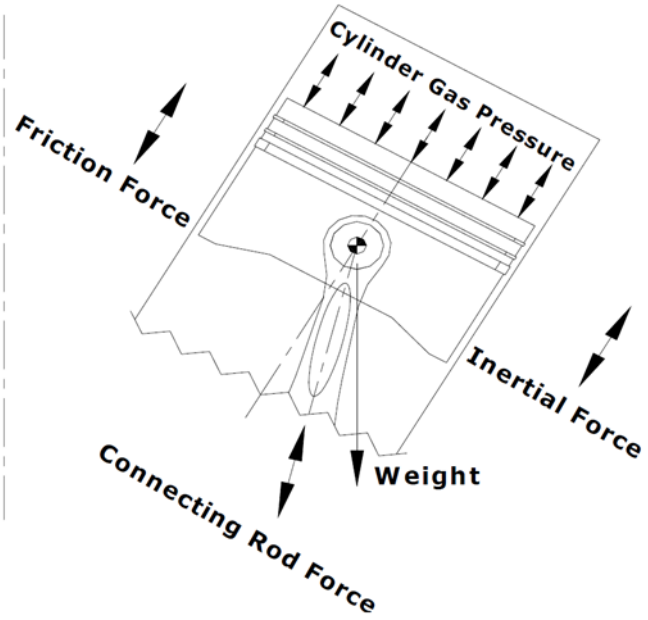

Fig. 2.6: The mechanical linkage telemetry system [50]

Error analysis

This method is based on the subtraction of two large numbers, namely the measured and the theoretical connecting rod force, to give a small number – friction force. This causes significant sensitivity to experimental error. The main error sources are the constant engine speed assumption, thermal shock on pressure transducers and error in the connecting rod force measurement.

- Constant engine speed assumption
  Calculating the inertial force requires knowledge of piston assembly component masses and their respective accelerations. An assumption, that is typically used in the application of the calculations, is that the intra-cycle (in-

stantaneous) engine speed (IES) is constant. This is not entirely accurate, the crankshaft accelerates and decelerates during each cycle. This assumption can have an impact on the inertial force calculation and consequentially the friction force measurements.

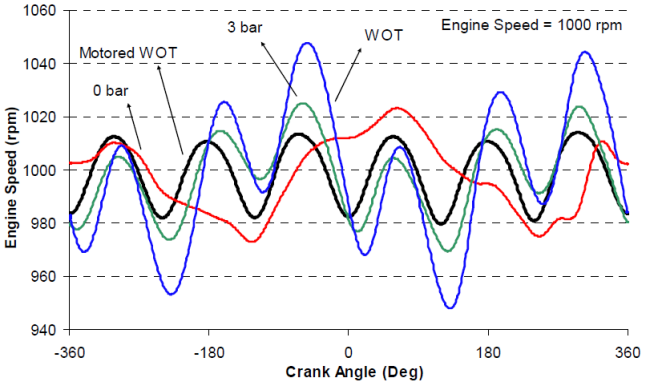

Fig. 2.7: Intra-cycle fluctations [50]

The inertial force correction terms are presented in [50]. As the engine speed increases there is less time between the combustion events, leaving less time for intra-cycle engine speed fluctuations. Consequently, the effect of the constant engine speed assumption on the friction force is reduced. As the load increases, the force transmitted during the power stroke of the engine increases, causing larger intra-cycle accelerations and greater errors in the calculated instantaneous friction force.

- Cylinder pressure error analysis
  Thermal shock is a major source of the cylinder pressure measurement error. A rapid change in temperature causes the diaphragm of the transducer to flex in a manner that is inconsistent with the applied pressure. These differences start at peak cylinder pressure, reache a maximum about 45 deg later, and recover over the next 360 deg to 450 deg, depending on the speed and load [52]. The thermal shock's severity depends on the transducer's design, mounting location, and in-cylinder conditions. The thermal shock effects are governed primarily by the engine speed, load, ignition timing, and to a lesser extent by the air/fuel ratio. The thermal shock makes the measured friction force appear too low during the expansion and intake strokes and too high during the exhaust stroke. The results presented in Fig. 2.8 indicate that $Kistler\ 6125B$ type transducers compensate thermal shock more effectively than $Kistler\ 6125A$.

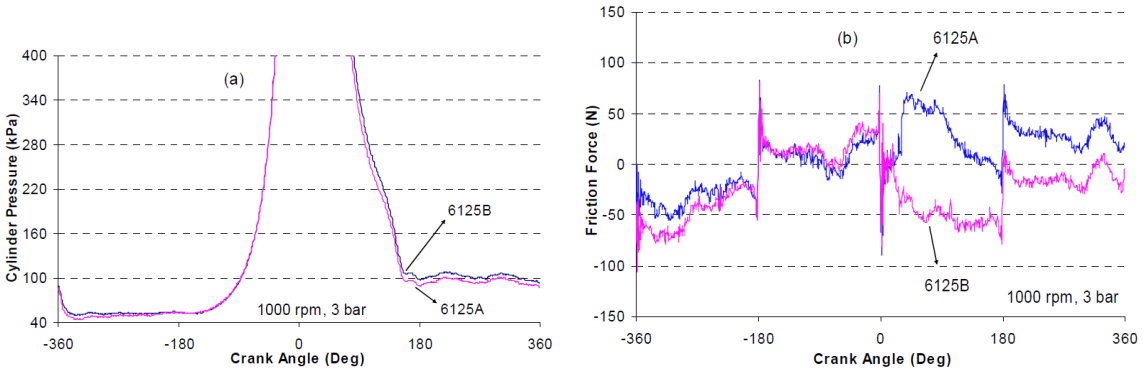

(a) Cylinder pressure

(b) Friction force

Fig. 2.8: Comparison of the effects of thermal shock on a 6125B and a 6125A pressure transducer [50]

- Connecting rod force measurement error
  A low signal to noise ratio is another source of uncertainty in the connecting rod force measurement. The strain gauge output is amplified over 2.5 million times by the time it is converted to force; hence the noise is also amplified by this value resulting in large errors in the measured forces. Another, smaller, source of error is the thermal dependency of the strain gauge. Although the gauge is "self temperature compensating," temperature effects still affect the output signal. The change in output over the operating temperature range is about 1 % and is non-linear.

Results of the study [50]

Before understanding the obtained results, it is advisable to review Stribeck's diagram (Fig. 1.18). As the engine speed increases, so does the in-cylinder friction shown in Fig. 2.9. In the 100 rpm case, it is clear from the very high gradients of the friction force at the dead centers that the lubrication regime is boundary. At 100 rpm, shortly after the dead centers, the friction force becomes nearly independent of the piston speed, which implies that the lubrication regime may be slightly mixed, but primarily boundary. At higher speeds, the piston assembly operates almost entirely in the hydrodynamic lubrication regime, except at the dead centers.

With accurate friction force results, in-cylinder friction mean effective pressure ($FMEP_{IC}$) can be calculated by integrating cycle resolved, in-cylinder engine friction over the incremental distance of the piston travel and dividing the result by cylinder volume. Fig. 2.10 shows an example of the instantaneous work loss based on the piston travel as a function of the crank-angle. This graph emphasizes the fact

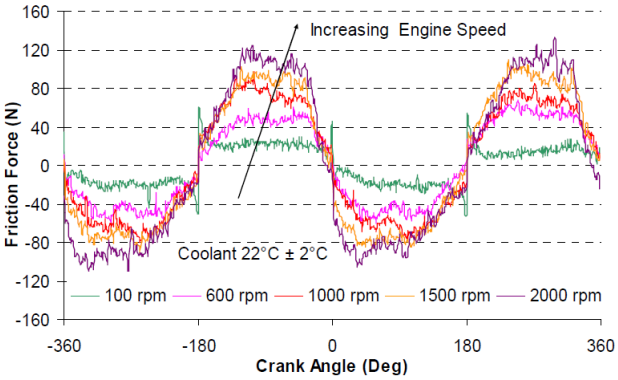

Fig. 2.9: Effect of speed on cycle resolved, in-cylinder friction at motored conditions with spark plugs removed [50]

that the majority of friction work loss occurs during the middle of the stroke, when the piston is traveling large distances. Work loss at the dead centers is minimal because the piston travel is minimal. Another advantage of this method of comparison is that it takes a complex curve and reduces it to a single number that can be easily communicated and compared to the total engine friction mean effective pressure $FMEP_{TOT}$. $FMEP_{TOT}$ is the difference between $BMEP$ and net indicated mean effective pressure ($IMEP_N$) for each cylinder analogous to the equation (2.7). This whole chapter was based on the work of Sethu et al. [50] who experimented with the 2.5L 60 deg V6 Ford Duratec SI engine. That explains the rotated piston position in Fig. 2.6.

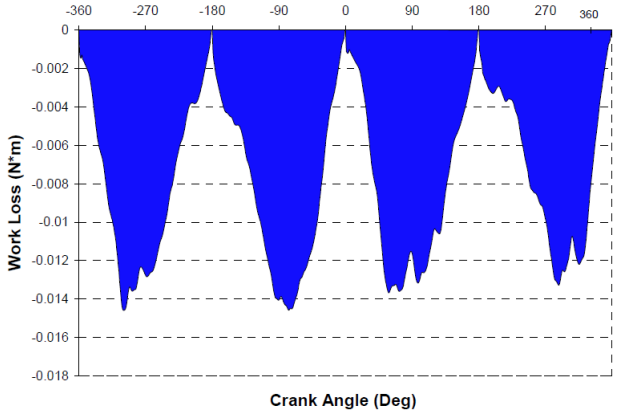

Fig. 2.10: In-cylinder work loss due to friction as a function of crank angle [50]

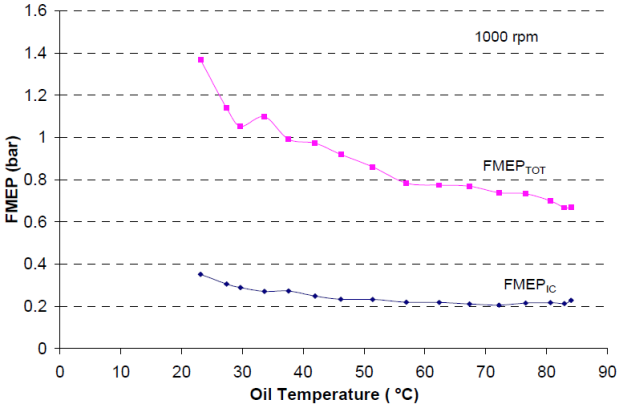

Fig. 2.11: Variation of FMEP with engine temperature during engine warm-up [50]

2.2.3 Wireless digital telemeter

Isarai et al. [53] have developed a measurement technique equipped with digital telemeter for strain, motion and temperature of engine parts under high speed running operation with high accuracy. This telemeter enables multi-point measurements at high engine speeds in small gasoline engines because of its compactness and light weight. It also enables long hours of engine testing without concern over battery life because of its low power consumption and selfcontained power generation.

Physical parameter	Temperature	Strain	Gap
Sensor	Thermistor or resistance temperature detector	Strain gauge (semiconductor type)	Eddy current gap sensor
Range	-30∼+400 °CC	-5000∼+3000 μstrain	0∼500 μm
Accuracy	±3 °C	±20 μstrain	± 5 μm
Time resolution	1.5 s	24 μs (1CAD at 7000 rpm)	
Number of measurement point	16 points/1 module (for temperature, strain, gap at user's choice)		
Transmission rate	400 μs/data (or 40 μs/data)		

Tab. 2.4: Measurement specifications [53]

Telemeter was applied between the piston skirt and the cylinder wall, and on the piston ring in order to investigate its behavior at high revolutions influenced by various forces such as in-cylinder pressure, inertia and friction. To enable the measurement of absolute values, gap sensors were used instead of generally used

capacitance sensors. To enable the measurement of the piston ring up-down movement and twisting behavior, 2 gap sensors were embedded in the sensor module at radially different distances from the piston center (Fig. 2.13).

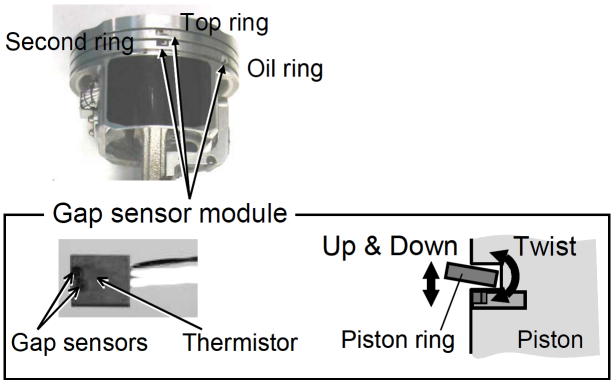

Fig. 2.12: Sensor layout [53]

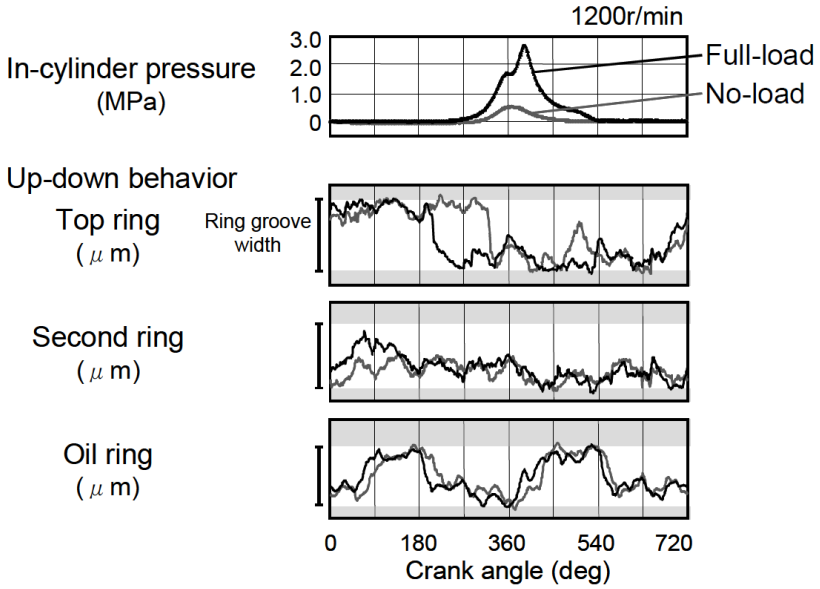

Fig. 2.13: Top ring behaviour in L4 cylinder 1.8L SI [53]

In the suction stroke at a low engine speed 2400 rpm, the top ring is stuck to the top by the negative pressure inside the cylinder, but it moves downward as the negative pressure changes to positive pressure as the compression stroke is entered. Afterward, in the exhaust stroke, the ring moves upward as the in-cylinder pressure drops and the inertia force increases. At a high engine speed of 6000 rpm, the effects of inertia increase, advancing the timing of the downward movement in the suction stroke and the upward movement in the exhaust stroke, compared with those at low

engine speeds. When the piston approaches compression TDC, moreover, the effects of the piston behavior come into play.

The developed telemeter is capable of multi-point measurement over long periods of time under high-speed, high-load conditions, and it is expected to make a contribution to the design and development by enabling the logical understanding of the actual-equipment phenomena [53].

2.2.4 Floating liner method

This method uses a special floating liner engine (FLE) designed and fabricated only for the piston assembly friction measurements. It can be said that the experiment is performed on a device different from the engine, for which the components are meant to be used. Therefore it has to be kept in mind that this set-up may slightly differ from the real operation conditions on the running engine.

In the FLE, the liner is constrained to move only in the vertical direction using the mounting guide studs (Fig. 2.14). When the piston is moving, the rubbing friction between the piston and the liner imparts a force which tends to move the liner along with the piston in the vertical direction. The force sensor restricts the movement of the liner and converts the movement into voltage signal [54].

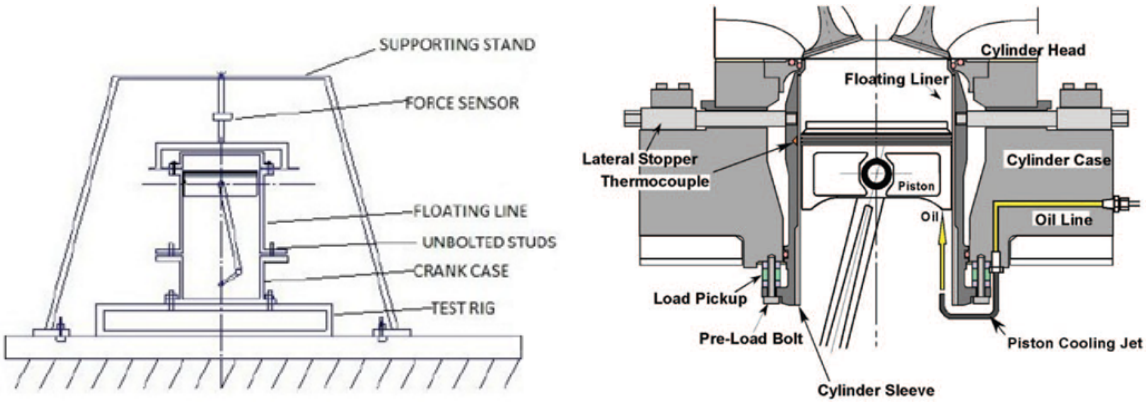

Fig. 2.14: Different FLE designs [54], [55]

Kwang-soo et al. [56] equipped FLE with a sapphire window (Fig. 2.15), which is after assembling on the specially designed engine block, honed with the cylinder bore, so that the overall bore surfaces are in the same geometric condition. The method of visualization measurement begins as ultraviolet light is flashed onto the oil film on the piston skirt surface. A high speed video camera records the visible light which is emitted by the fluorescent dye mixed in the lubricating oil. Reflected ultraviolet light is shut out by the filter before coming into the camera lens. Fig. 2.16 is the schematic diagram of the measuring device.

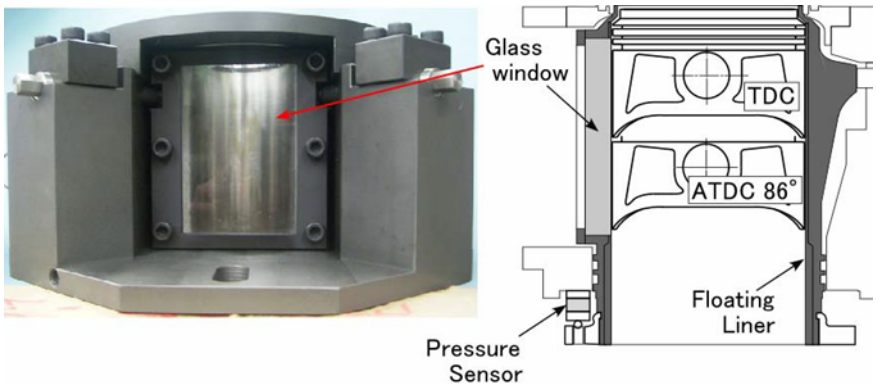

Fig. 2.15: Liner window for simultaneous piston/ring friction and oil film measurement [56]

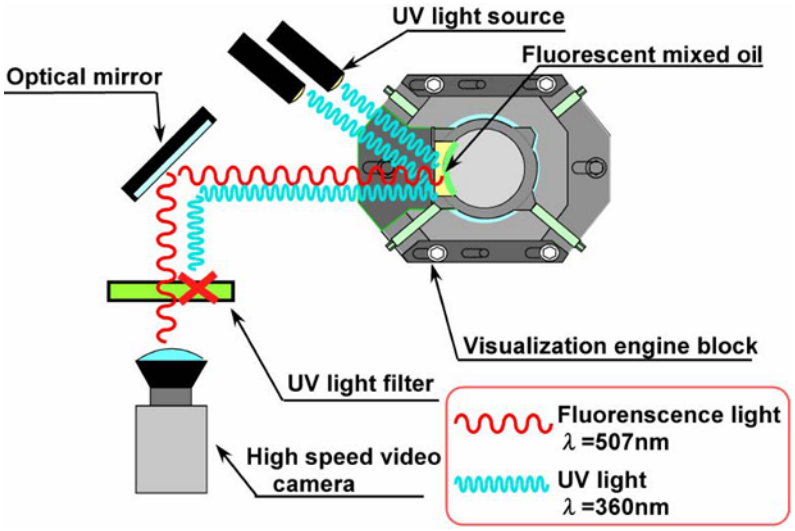

Fig. 2.16: Visualization measuring device [56]

The image of the oil film, taken at one degree crank angle steps, is then processed in order to convert it into a multi-layer contour map by filtering it into several color groups to analyze the oil film distribution. Fig. 2.17 (1500 rpm engine speed) shows the sequence of the image processing. The darker areas indicate thinner oil film. The output of such a device is a picture sequence of the oil film formation with related friction forces measured. For more detailed info see [56] where the description of the oil film behavior during each stroke is also mentioned.

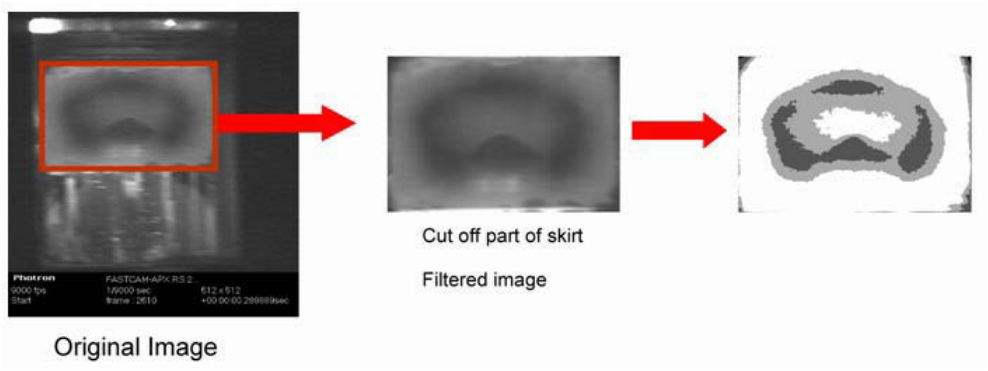

Fig. 2.17: Sequence of image processing [56]

2.2.5 The blow-by/blow-back flow experiment

For the blow-by/blow-back model validation, the cylindrical ring pack is represented by the three-plate model of a rectangular piston ring pack apparatus (Fig. 2.19). It consists of three plates: engine liner plate, piston ring plate, and piston plate. The dimensions of the piston, the piston ring and its groove are replicated from the original observed engine. In order to simulate the combustion pressure, pressurized natural gas in the single pulse chamber is injected into the rectangular piston ring pack apparatus by a fast acting valve actuator. Then, the pressures in the piston top land $P1$, piston second land $P2$, and piston third land $P3$, are monitored and recorded [30].

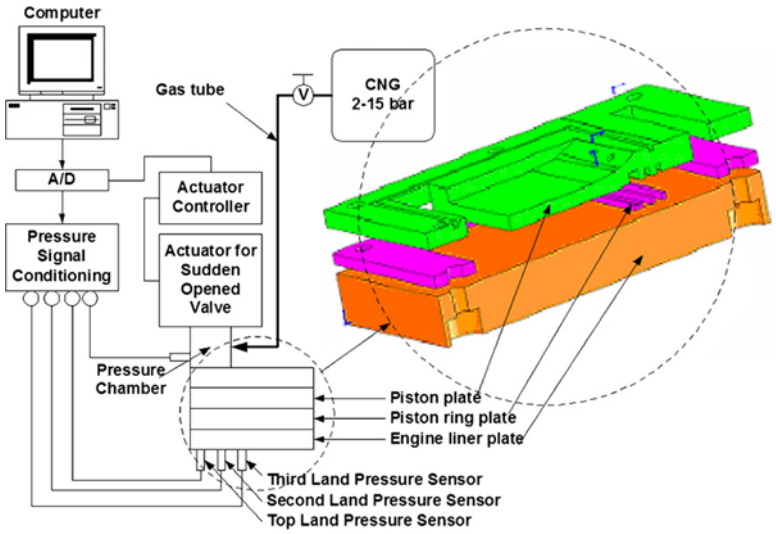

Fig. 2.18: Schematic diagram for investigating the flow through the custom-made three-plate rectangular piston ring pack [30]

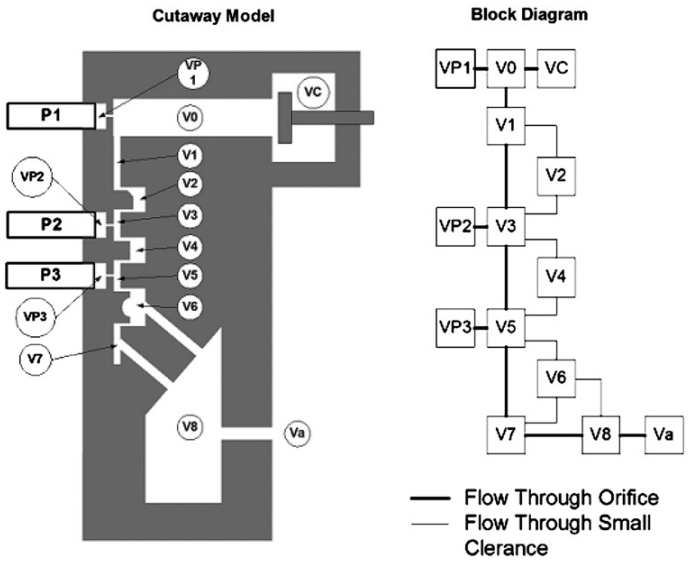

Fig. 2.19: The blow-by/blow-back gas flow cutaway model and block diagram [30]

Since there are no moving parts, and the gas composition and the gas temperature are being controlled, this model is good only for the validation of the computational model, but does not represent the actual engine operation conditions. For real blow-by evaluation, the overall gas flow is measured after the whole piston ring pack.

2.3 Experimentally calibrated physical cranktrain model for FMEP prediction

The accuracy of this type of a theoretical model is based on the calibration and usage of the data obtained in previous tests on different engines – long-term experiences – one of the negative aspects of this approach. Macek et al. [57] discovered semi-empirical tribological code, which predicts friction losses with good accuracy even during non-standart conditions, e.g. at low lubricating oil temperature.

First of all, a model for the simulation of mechanical losses has been developed. In this case the forces of the cranktrain are solved by standard, well-known body releasing method. The dynamic effects of a piston, piston pin and reciprocating part of the connecting rod are represented by the resulting inertia force in the centers of gravity of substituting bodies. The rotating vector of a centrifugal force describes a rotating mass of a connecting rod and those of crank web and its counter-weight. The resulting correction moment of the connecting rod inertia represents the added effects of the connecting rod tilting movement.

The coefficient of friction is calculated as:

$$C = \frac{F_t}{F_N} = f(So) \tag{2.8}$$

where F_t is the tangential force, F_N is the normal loading force and So is Sommerfeld number defined by (1.11). The most significant finding is a model of the Stribeck curve presented as an universal dependence of a friction coeffcient C on So, if the oil viscosity η influenced by the bearing temperature is taken into account:

$$\begin{gathered} F_t = -sign(u)C|F_N| = \\ = -sign(u)\left(C_{Coulomb}e^{-3\left|\frac{So_{lim}}{So}\right|^{2.5}} + \frac{K}{So}\right)|F_N| \\ if \quad F_N = 0 \quad F_t = -K\eta uL \end{gathered} \tag{2.9}$$

where three independent input variables have to be satisfied: zero-slip (Coulomb) friction coefficient $C_{Coulomb}$, transition So_{lim} defining the limit of the friction mode transition from mixed to purely a hydrodynamic one and the slope of the hydrodynamic friction line K. The coefficient K should be calibrated for a certain temperature and viscosity [28]. The change of viscosity influences both the transition So_{lim} and the slope of the hydrodynamic part of the Stribeck curve, K. An important factor for this friction is the wetted width perimeter L. Real dry friction does not occur even at zero velocity if stopping the movement is short and the oil film is thick enough because of the time needed for the oil film squeezing (e.g. on a piston skirt in both dead centers). The friction coefficient must be calibrated according to the measurements on a similar engine, not by the use of recommended friction coefficients from mechanical engineering handbooks. The example of the Stribeck curves for the piston rings is presented in Fig. 2.20.

In the case of the same type of friction surface pair with similar loads at a surface (rings or piston skirt or bearings with fast and almost continuous motion or bearings with slow and interrupted motion, etc.) the same transition So_{lim} should be found.

The next step is the implementation of the model into a powertrain simulation software. In the work [57] the GT-Suite, including GT-Power and GT-Crank [29] was used to evaluate the FMEP, where the friction code (2.3) was implemented into the calculation in order to consider the effect of the oil temperature. The default formula used as a first approximation of friction losses in this software is Chen & Flynn model described in section 2.1.1.

The Stribeck curves used in the model described above were calibrated using motoring data measured on various engines in the past. The fast and general method

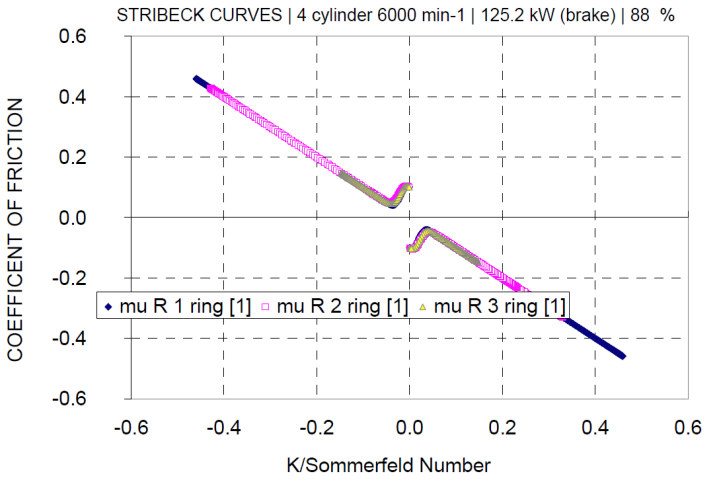

Fig. 2.20: Stribeck curve for piston ring [57]

uses a search of calibration parameters by the optimization of squared deviations between the simulation and measurement. However it is very important to use the correct temperature relations, not the oil tank temperature which does not describe conditions of the piston rings (Tab. 2.5).

Friction surface pair	Oil temperature °C
Compression rings	1^{st} ring: 160∼140 2^{nd} ring: 135∼120
Oil control ring, piston skirt and pin	$T_{oiltank}$-70
Bearings [bar]	$T_{oiltank}$

Tab. 2.5: Oil temperatures in each friction surface pair [57]

The potential of the code is highlighted in the paper [57]. Apart from being a good tool for validation, the analysis can continue from theoretical results to study the particular friction surfaces separately. In addition, the lubrication can be studied along engine cycle as seen for piston rings. As a result, the coupling thermodynamics and this mechanical model enables to search for the global optimum for each operating point by using optimization tools. Downsizing the engine or other changes in the design can also be analyzed by the code since the thermodynamic response is considered by the in-cylinder pressure and the geometry is easily modified by parameters. The experimental validation was done by the instantaneous IMEP method for overall friction estimation (section 2.2.1).

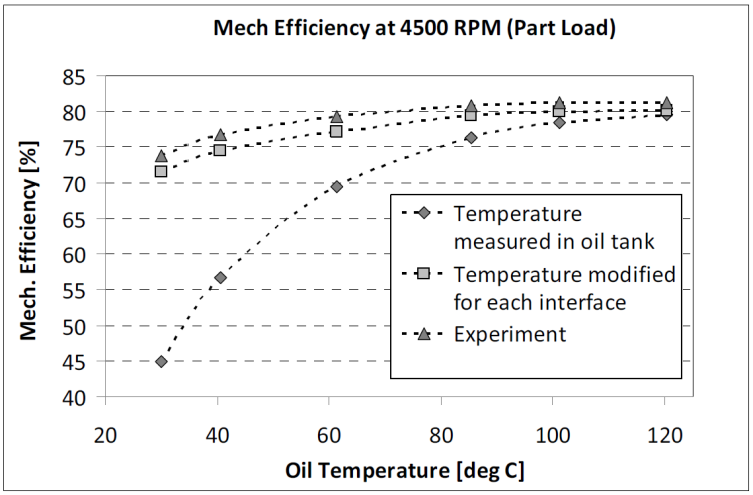

Fig. 2.21: Experimental and predicted mechanical efficiency in dependence on temperature [57]

2.4 Computational models

Computational simulations are hydrodynamic friction models, solving Reynolds-like lubrication equations for the complicated geometry of the piston ring/cylinder liner and piston with load and sometimes even with distorted shapes. The piston ring motion is caused by the static ring tension force F_k, torsion M_k from the installation of the piston ring in the cylinder liner, the inertia forces F_i and the moment M_i related to the component mass and engine speed, and the surface forces. Regarding the surface forces, there are four types of possible forces exerting on the piston ring surface. These forces depend on the piston ring surroundings as shown in Fig. 2.22.

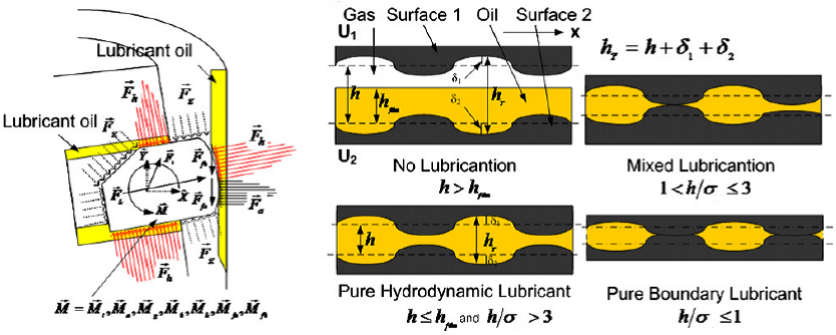

Fig. 2.22: The forces and moments exerting on a piston ring surface [30]

Parameter h, presented in Fig. 2.22, is the nominal film thickness; h_{min} is the minimum film thickness; σ is the composite root mean square (RMS) roughness, δ_1

and δ_1 are the local film roughness of surface 1 and surface 2, respectively. The four types of force exerting on a piston ring surface are:

1. No lubrication: $h > h_{film}$, the piston ring surface are exposed to gas pressure. The force and the moment for this condition are the F_g and M_g. The gas pressure may be generated by the cylinder pressure and/or the blow-by/blow-back flow.
2. Pure hydrodynamic lubrication: $h \leq h_{film}$ and $h/\sigma > 3$, a gap is fully lubricated. The forces and the moments for this condition are F_h, F_{fh}, M_h and M_{fh}.
3. Pure boundary lubrication: $h/\sigma \leq 1$, when the oil supply is insufficient, each surface partially contacting each other as so-called asperity contact. The forces and the moments for this condition are F_a, F_{fa}, M_a and M_{fa}.
4. Mixed lubrication: $1 < h/\sigma \leq 3$, both hydrodynamic and pure boundary lubrications occur in the gap [30].

Wannatong et al. [30] divided the piston ring into n sections (Fig. 2.23). At each section, the calculation nodes were assigned to the piston ring surface. Every node contains its own properties, which are the position, area and the normal direction. In each time step, the followings were investigated: the nodes position, the clearance between the nodes and the engine liner wall, and the clearance between the nodes and the groove surface. The surface pressure, depending on the boundary type, was determined and converted into surface forces and moments. The position of nodes were obtained as the results of the linear and angular equations.

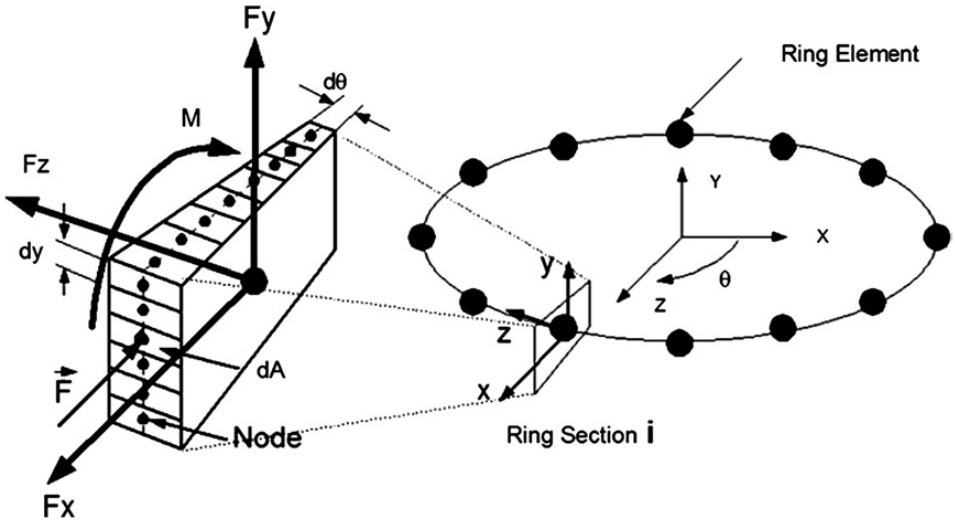

Fig. 2.23: Simulation concept of n sections of piston ring with nodes assigned [30]

Novotny et al. [33] work with the 2D axisymmetric piston ring model, where all loads and motions are considered constant along the circumference. This simplification allows a much faster and stable solution, which enables faster initial calculations. However, it cannot take into account the nonaxisymmetric partial motion which the piston ring surely does.

2.4.1 Hydrodynamic lubrication model

For the pure hydrodynamic lubrication model the Reynolds' equation is used. It is the relationship between the pressure and the film shape as a function of oil viscosity and relative velocity. Since the thickness between the piston ring and the cylinder wall is much smaller than the piston ring radius, the simplified modification of Reynolds' equation can be used:

$$\frac{\partial}{\partial x}\left(\phi_x \frac{h^3}{12\eta}\frac{\partial \bar{p}}{\partial x}\right) = \frac{U}{2}\frac{\partial \bar{h}_T}{\partial x} + \sigma\frac{U}{2}\frac{\partial \phi_s}{\partial x} + \frac{\partial \bar{h}_T}{\partial t} \tag{2.10}$$

where ϕ_x is the flow factor, η is the dynamic viscosity, $\bar{p}$ is the mean hydrodynamic pressure, U is the relative sliding surface velocity, $\bar{h}_T$ is the averaged film thickness and ϕ_s is the shear factor.

The pressure flow factors ϕ_x can be identified as the correction factors in the pressure flow term to incorporate the effects of surface roughness. The shear flow factor ϕ_s can be seen as the correction factor applied to the additional flow term to compensate for the combined effect of the sliding and roughness. The formulas for both of these factors are available in [34]. Fig. 2.25 shows the average ϕ_x and ϕ_s, ϕ_{fs} and ϕ_{fp} (needed in further calculations) values by Patir and Cheng [35] for the isotropic and the directional surfaces as a function of h/σ and the surface pattern parameter γ (Fig. 2.24) of the combined roughness.

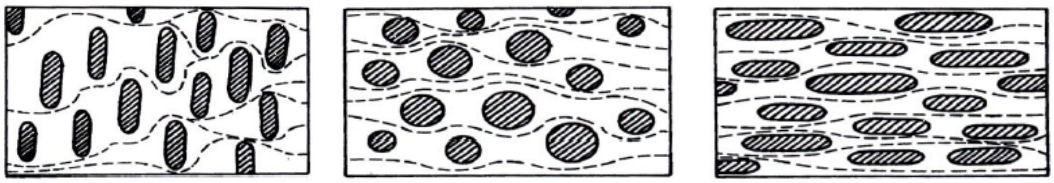

(a) $\gamma > 1$ (b) $\gamma = 1$ (c) $\gamma < 1$

Fig. 2.24: Surface pattern paramater γ

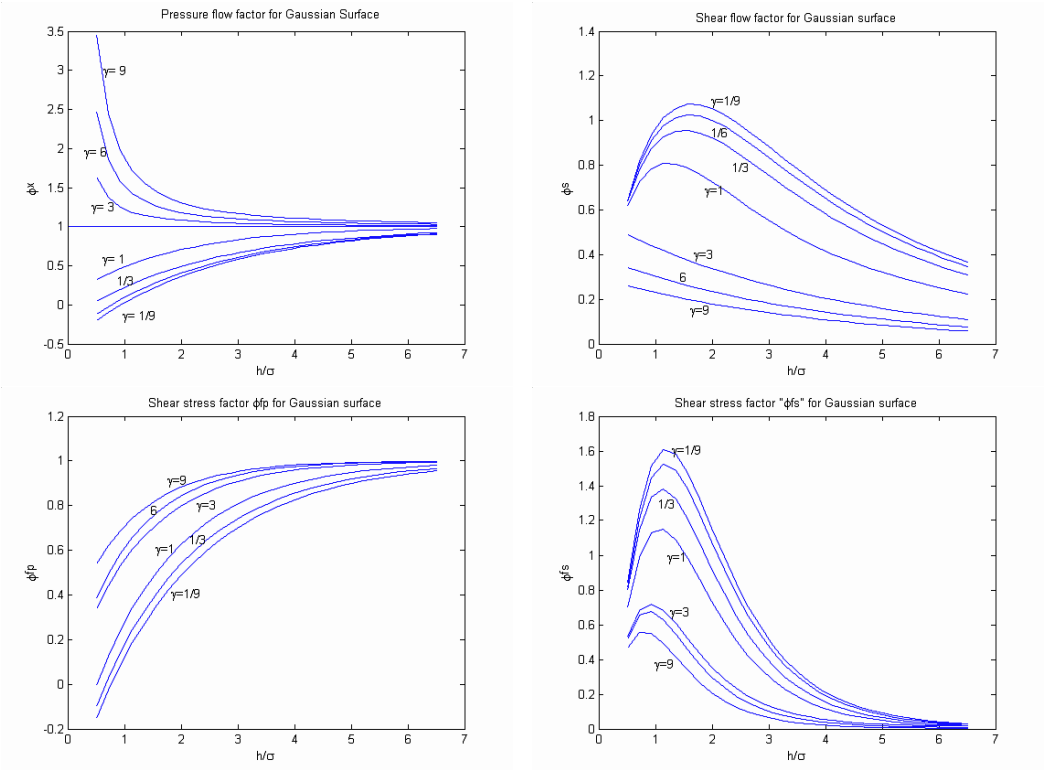

Fig. 2.25: Flow factors of Gaussian surface for different γ values [35]

The flow factor limit values are used in [33] so the average Reynolds' equation can be written:

$$\frac{\partial}{\partial x}\left(\frac{\rho h^3}{12\eta}\frac{\partial \bar{p}}{\partial x}\right) = \frac{U}{2}\frac{\partial \rho \bar{h}_T}{\partial x} + \frac{\partial \rho \bar{h}_T}{\partial t} \tag{2.11}$$

where ρ is the oil density. The dependency of oil density on pressure can be neglected easily like in (2.10), because the actual oil density ρ is only 1.34 times higher ($\rho = 1.34\rho_0$) for pressures approaching infinity ($p \to \infty$) [36].

The hydrodynamic force $F_{h,i,n}$, the mean hydrodynamic shear stress $\bar{\tau}_{i,n}$ and viscous friction $F_{fh,i,n}$ exerting on the area $dA_{i,n}$ for each section n and node i (Fig. 2.23) are obtained:

$$F_{h,i,n} = \bar{p}_i, ndA_{i,n} \tag{2.12}$$

$$\bar{\tau}_{i,n} = -\frac{\eta U}{h}\left(\sigma_f + \sigma_{fs}\right) + \sigma f p \frac{h}{2}\frac{\partial \bar{p}}{\partial x} \tag{2.13}$$

$$F_{fh,i,n} = \bar{\tau}_{i,n} dA_{i,n} \tag{2.14}$$

The Reynolds' equation (2.10) can be solved by numerical methods, e.g. backward time and central space [30] or the finite difference method [33]. The 2D axisymmetric model of the piston ring with limit values of the shear factors simplify hydrodynamical friction force calculation to:

$$F_{fh} = \int_{x_1}^{x_2} \left(-\frac{\eta U}{h} + \frac{h}{2}\frac{\partial \bar{p}}{\partial x} \right) \pi d.dx \tag{2.15}$$

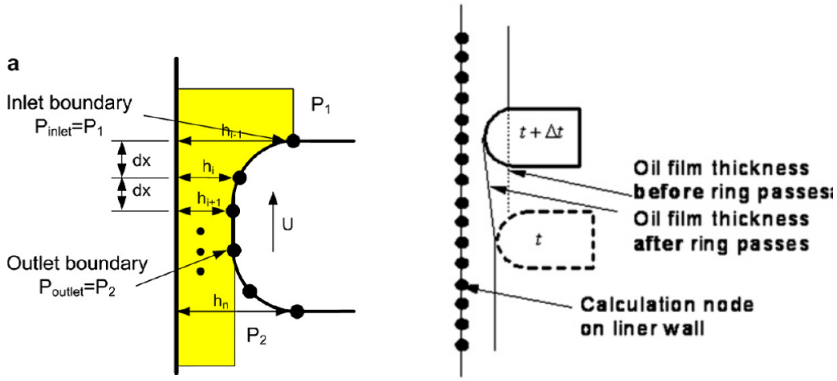

Fig. 2.26: Point approximation of Reynolds' equation [30]

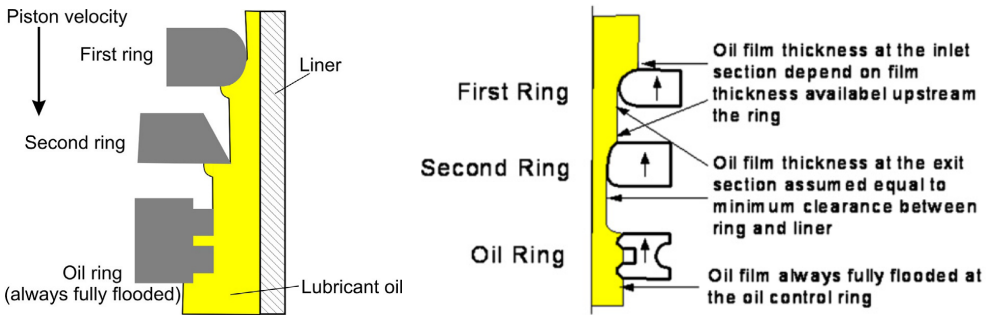

(a) upward motion (b) downard motion

Fig. 2.27: Oil film thickness available on the engine liner wall [33], [30]

It is a common fact that oil film thickness h changes during the engine cycle. This change can be derived from the piston ring motions, the oil film evaporation, etc. It affects the piston ring lubricant conditions, especially the inlet condition. As one can see in the Fig. 2.27, for the first and the second rings, the film inlet position is the first contact point between the oil film surface and the ring face profile. For the film exit position, the oil film thickness is assumed equal to the minimum clearance

between the ring surface and the cylinder wall. The oil control ring is supposed to be always soaked in oil. Thus, the fully flooded condition is applied to this ring.

2.4.2 Pure boundary lubrication model

When the oil supply is insufficient, the pure boundary lubrication (asperity contact) is used. It is well described by Greenwood and Tripp [37].

$$p_{a,i,n} = \frac{16\sqrt{2}\pi}{15} \left(\sigma_s \beta \eta_a\right)^2 E^* \sqrt{\frac{\sigma_s}{\beta}} F_{5/2}\left(h/\sigma_s\right) \tag{2.16}$$

$$F_{a,i,n} = p_{a,i,n} dA_{i,n} \tag{2.17}$$

$$F_{fa,i,n} = C_f F_{a,i,n} \tag{2.18}$$

where σ_s is the composite summit height standard deviation, β is the radius asperity summit, η_a is the surface density of asperity peaks, $F_{5/2}(h/\sigma_s)$ for Gaussian distribution surface and the details of asperity contact is shown in [38] and [39], C_f is the dry friction coefficient and E^* is the reduced elastic modulus:

$$\frac{2}{E^*} = \frac{1-\mu_1^2}{E_1} + \frac{1-\mu_2^2}{E_2} \tag{2.19}$$

where E_1 and E_2 are the elastic moduli, μ_1 and μ_2 are the Poisson's ratios of surfaces 1 and 2 respectively.

2.4.3 Mixed lubrication model

The state between pure hydrodynamic and pure boundary lubrication is called mixed lubrication. The normal load $F_{M,i,n}$ and its friction $F_{fM,i,n}$ are carried by the hydrodynamic and boundary force components:

$$F_{M,i,n} = F_{h,i,n} + F_{a,i,n} \tag{2.20}$$

$$F_{fM,i,n} = F_{fh,i,n} + F_{fa,i,n} \tag{2.21}$$

2.4.4 Gas pressure model

The gas pressure in the piston-cylinder system may be divided into several groups. The cylinder pressure is measured by a pressure transducer (Fig. 2.4) and the crevice pressure is simulated by the blow-by/blow-back model shown in Fig. 2.28. The flowing volume consists of the combustion chamber $V0$, piston top land $V1$, second land $V3$, third land $V5$, piston skirt $V7$, and the stagnation volumes behind each ring $V2$, $V4$, and $V6$. They are connected with either a small clearance or a piston ring gap.

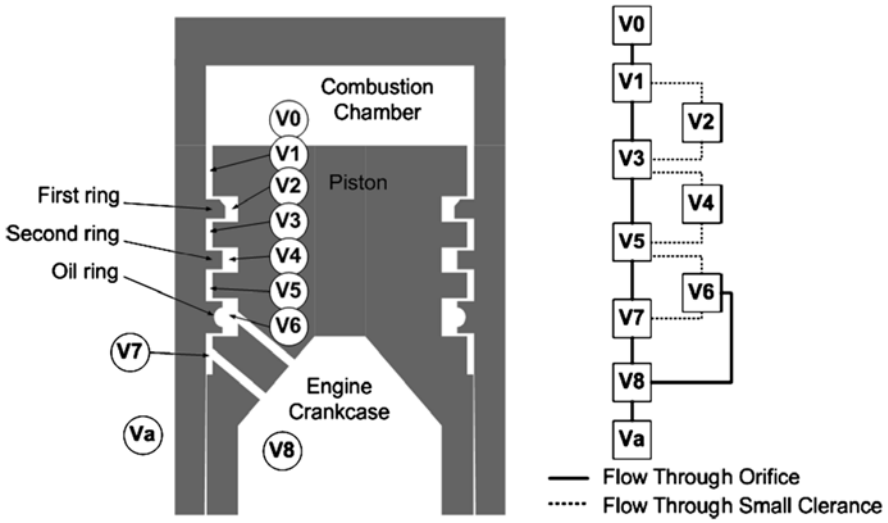

Fig. 2.28: Blow-by/blow-back flow cutaway and block diagram model [30]

- Gas flows through the piston ring gap
  This kind of phenomenon is shown in Fig. 1.19a. The isentropic orifice flow is assumed:

$$\dot{m} = A_E \rho_1 \sqrt{\kappa R T_1} \quad for \quad \left(\frac{p_1}{p_0}\right) \leq \left(\frac{2}{\kappa+1}\right)^{\frac{\kappa}{\kappa-1}} \tag{2.22}$$

$$\dot{m} = A_E \sqrt{\rho_0 p_0} \sqrt{\frac{2\kappa}{\kappa-1}\left(\left(\frac{p_1}{p_0}\right)^{\frac{2}{\kappa}} - \left(\frac{p_1}{p_0}\right)^{\frac{\kappa+1}{\kappa}}\right)} \; for \; \left(\frac{p_1}{p_0}\right) > \left(\frac{2}{\kappa+1}\right)^{\frac{\kappa}{\kappa-1}} \tag{2.23}$$

  where A_E is the efficient area, R is the gas constant, T is the temperature, p_0 and p_1 are pressures in the first and second volume respectively, ρ_0 and ρ_1 are gas density in first and second volume respectively, κ is the polytrophic exponent.

- Gas flows through a ring/groove or a ring/cylinder wall clearance
  This kind of phenomenon is shown in Fig. 1.19b and 1.19c. Laminar flow due to a small Reynolds number is assumed [30]:

$$\dot{m}_{cle} = \int_0^{2\pi} \dot{m}_{cle,n} d\theta \quad where \quad \dot{m}_{cle,n} = \rho \left(-\frac{h^3}{12\eta} \frac{\partial p}{\partial x} + U \frac{h}{2} \right) \tag{2.24}$$

  where θ is the section number (2.23). This kind of gas flow may be neglected due to the character of the piston ring motion - both clearances between a ring and a piston groove or cylinder wall are sealed the most of the time [40].
  For each time step, the rates of mass flowing in and out at each stagnation volume are determined. The mass conservation equation and the equation of state for an ideal gas are used as:

$$\frac{1}{RT} \left(V_n \frac{\partial p_n}{\partial t} + p_n \frac{\partial V_n}{\partial t} \right) = \sum \dot{m}_n \tag{2.25}$$

  where $\sum \dot{m}_n$ is the net mass flow rate of volume n, V_n is the volume and p_n is the pressure behind the segment n. The gas force $F_{g,i,n}$ which is exerting on the area $dA_{i,n}$ of the section n, the node i is obtained from:

$$F_{g,i,n} = p_{g,i,n} dA_{i,n} \tag{2.26}$$

2.4.5 Tension Force from installation of piston ring in the cylinder liner

In order to install the piston ring into the engine liner, the piston ring is compressed to fit the liner internal diameter. The pretension force can be represented by the surface force:

$$F_{k,i,n} = p_{k,i,n} dA_{i,n} \quad where \quad p_{k,i,n} = \frac{1}{2} \frac{E b^3 m}{l^2 d(d-b)} \tag{2.27}$$

where E is the Young modulus, b is the radial wall thickness, m is the total free gap and d is the nominal diameter. Other method of pretension force application is shown in section 3.4.

2.4.6 Torsion from piston ring twist

The torsion of the piston ring is a common phenomenon in rings with an unsymmetrical cross section such as tapper faced compression rings. Its evaluation is available in [30], [31] or [11]. Torsion can be calculated using the torsional stiffness, like it is presented in [32].

2.4.7 Governing equation

Forces and moments from the previous sections meet in the linear and angular momentum's equations as follows:

$$F_{x,n} = m_n \ddot{x}_n = F_{gx,n} + F_{h,x,n} + F_{ax,n} + F_{k,x,n} + F_{fhx,n} + F_{fax,n} \tag{2.28}$$

$$F_{y,n} = m_n \ddot{y}_n = F_{gy,n} + F_{h,y,n} + F_{ay,n} + F_{k,y,n} + F_{fhy,n} + F_{fay,n} \tag{2.29}$$

$$M_n = I_n \ddot{\theta}_n = M_{g,n} + M_{h,n} + M_{a,n} + M_{k,n} + M_{fh,n} + M_{fa,n} \tag{2.30}$$

where $\ddot{x}_n$ and $\ddot{y}_n$ are accelerations in the directions x and y, m_n is mass, I_n inertia moment and $\ddot{\theta}_n$ is the angular acceleration of the section n. In each time step, all force and moment exerting on the piston surface were put into the Newton's (2.28), (2.29) and the Euler's (2.30) equations and solved.

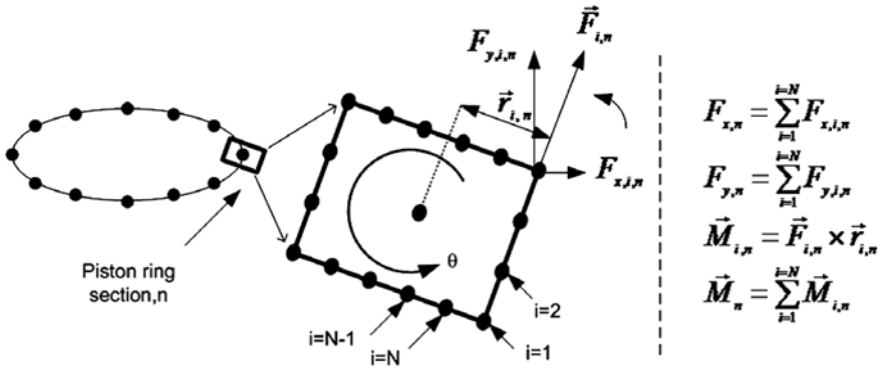

Fig. 2.29: Summation of forces and moments [30]

The simulation algorithm is executed (Fig. 2.30):
Step 1: The simulation started with initializing the parameters such as the starting position of the piston, the film thickness the engine liner, etc.
Step2: The piston position and the crevice pressure from the previous time step

were updated.

Step3: For each ring, the initial position of the piston ring in its groove was trialed. Then, the distance from the piston ring surface (from each calculation node) to the engine liner surface and to the groove surface were calculated.

Step4: Linear and angular accelerations of the piston ring sections were calculated.

Step5: The deflections of piston ring structures and force were calculated and stored in each calculation node.

Step6: The boundary condition of each piston ring was examined according to section 2.2. The calculated parameters, distance and surface pressure depending on boundaries condition, were stored in each calculation node.

Step7: All forces and moments mentioned-above were put into the linear and angular momentum equations (Newton's and Euler's equations). The summation of all terms from each equation is an error.

Step8: The trial position parameters minimizing the error are the solution of the piston ring motion for this time step. Hence, the secant iteration method may be used.

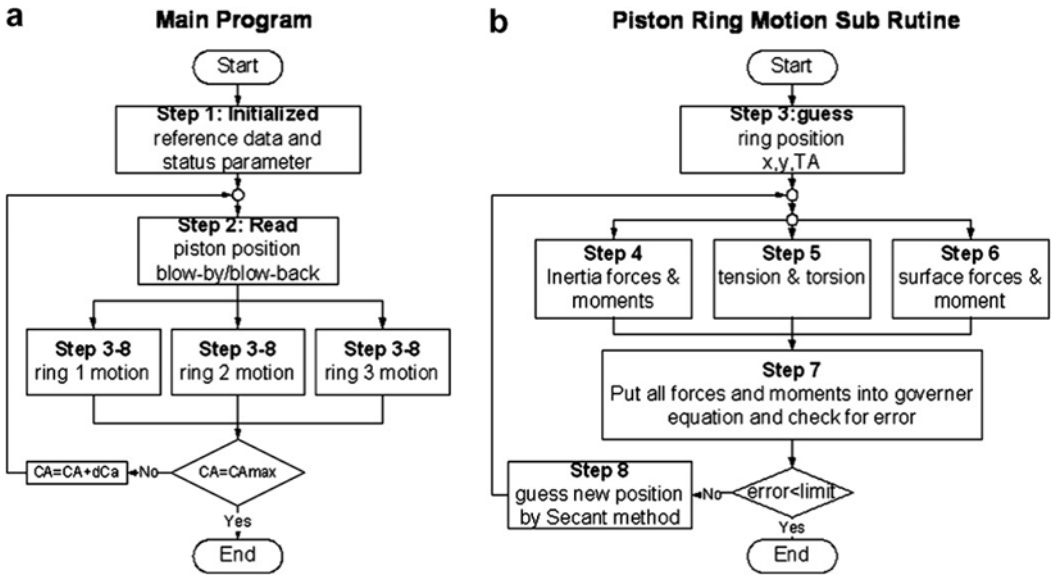

Fig. 2.30: Flowchart of piston ring dynamics simulation program [30]

This section was based on the study of Wannatong et al. [30], who performed the simulation by a network consisting of four personal computers, each with a configuration of Pentium IV, 1.66 GHz, and 512 MB of RAM. In the simulation program, each piston ring was divided into 11 sections. At each section, 400 calculation nodes were assigned to the piston ring surface. The calculation time step was equivalent

to 0.1 deg of the crank angle of engine revolution. From the numerical experiment results, the calculation time of the simulation program with parallel technique was four times faster than that performed by a single PC (8 s per time step).

The authors claim, that this is a simulation of the 3D piston ring motions. But, the 11 computed sections are separate and do not communicate with each other. The motion of one section will not affect the motion of another section directly. This confirms the fact, that no material definition was seen in the entire article which would define the deformation of the piston ring along the circumference. It can be said that this simulation model is quasi-3D.

Wolff et al. [40] used a 2D model analogous to the one described in this chapter, but they implemented resistance to the angular deformation of the piston ring by the addition of the torsional stiffness K into the angular momentum equation. This parameter depends on the piston ring geometry and material.

A fully functional 3D analysis of piston ring dynamics is in the hands of Federal Mogul [41]. It includes all the functions of the model mentioned above and in addition the 3D dynamic twist calculation is also possible, so is the fluttering detection (Fig. 2.32).

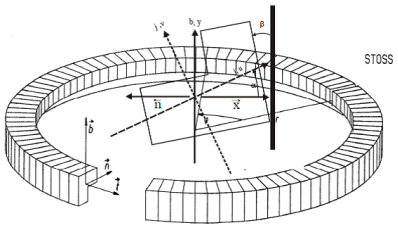

Fig. 2.31: Discretizated piston ring by Federal Mogul [41]

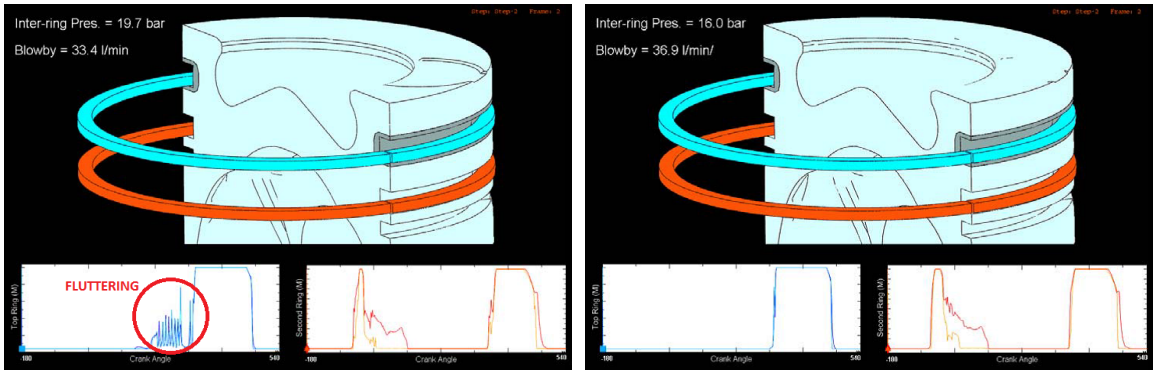

(a) Initial design (b) Modified design

Fig. 2.32: Optimized design due to 3D piston ring dynamic model [41]

3 SOLUTION

This master's thesis serves as a base for further piston ring motion and mechanical loss investigation. The goal is to create a flexible piston ring model and implement it into the multibody system (MBS) software. This may be done in various ways for instance by exporting modal neutral file (.mnf) from commercially available software using the finite element method (FEM) such as ANSYS. In order to prepare a flexible model in software, which will be afterwards used to simulate complex piston ring dynamics, the analytical solution is more effective, less engineer time demanding and less user's error sensitive. In a business talk, less different software licenses equals less expenditure.

3.1 Timoshenko beam theory

Stephen Timoshenko [58] is reputed to be the father of modern engineering mechanics. However, his theory has its limitations which have to be kept in mind:

- beam is defined by the neutral axis and cross section (Fig. 3.1),
- neutral axis is a continuous function in both, the underformed and the deformed state,
- cross section is a planar before and after loading – no warping or out-of-plane distortion occurs. Warping greatly complicates the behavior of the beam,
- all loads act through the centroid of the cross sectional area,
- many of bellow equations are derived with assumption of small deflections,
- beam is perfectly elastic – it recovers its original shape completely after unloading.

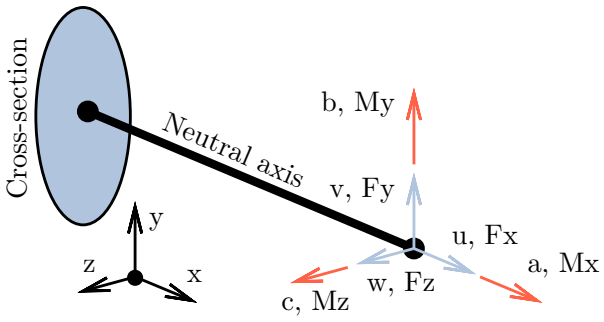

Fig. 3.1: Beam theory model (a, b and c are angles of rotation; u, v and w are deflections)

Robert Hooke [59] in 1678 confirmed by a direct experiment with the extension of prismatic (constant cross section) bars, that the elongation u is proportional to the axial force F_x in an elastic portion of loading. It is also proportional to the length of the bar l and inversely proportional to the cross sectional area A and to the modulus of elasticity E. Hooke's experimental law can be expressed as:

$$F_x = \frac{AE}{l}u \quad or \quad F_x = K_{11}u \tag{3.1a}$$

$$where \quad K_{11} = \frac{AE}{l} \tag{3.1b}$$

where K_{11} is the tensional stiffness.

Unlike the Bernoulli-Euler beam theory, Timoshenko does not neglect shear deformation effects for bending of beams. When the shear deformations are included, sections that are originally perpendicular to the neutral axis may not be perpendicular to the neutral axis after the deformation. If the beam is not slender, then shear strains will contribute significantly to the strain energy within the bent beam. The deformed shape of slender beams is different from the deformed shape of stocky beams, where the potential energy has a bending strain component and a shear strain component. In other words, the transverse deformation of a beam with shear and bending strains may be separated into a portion related to shear deformation and a portion related to bending deformation. The following shape functions satisfy the Timoshenko beam equations for transverse displacements [60]:

$$N_1 = \frac{1}{1+P_y}\left(1 - \frac{3x^2}{l^2} + \frac{2x^3}{l^3} + \left(1 - \frac{x}{l}\right)P_y\right) \tag{3.2a}$$

$$N_2 = \frac{l}{1+P_y}\left(\frac{x}{l} - \frac{2x^2}{l^2} + \frac{x^3}{l^3} + \frac{1}{2}\left(\frac{x}{l} - \frac{x^2}{l^2}\right)P_y\right) \tag{3.2b}$$

$$N_3 = \frac{1}{1+P_y}\left(\frac{3x^2}{l^2} - \frac{2x^3}{l^3} + \frac{x}{l}P_y\right) \tag{3.2c}$$

$$N_4 = \frac{l}{1+P_y}\left(-\frac{x^2}{l^2} + \frac{x^3}{l^3} - \frac{1}{2}\left(\frac{x}{l} - \frac{x^2}{l^2}\right)P_y\right) \tag{3.2d}$$

where P_y gives the relative importance of the shear deformations to the bending deformations:

$$P_y = \frac{12EI_z f_{s,y}}{GAl^2} \tag{3.3}$$

where G is the shear modulus of elasticity and $f_{s,y}$ is called a form factor for shear in y direction:

$$G = \frac{E}{2(1+\mu)} \tag{3.4}$$

$$f_{s,y} = \frac{A}{I_z^2} \int_A \frac{Q_z^2}{l_z^2} dA \tag{3.5}$$

where μ is the Poisson's ratio, Q_z is the first moment of a cross section area to be sheared by a force in the y direction and l_z is the cross section dimension in the z direction. Form factor values for typical cross sections are shown in Tab. 3.1.

Section	From factor
Rectangle	6/5
Circle	10/9
Thin tube	2

Tab. 3.1: Form factor for shear [58]

The elastic stiffness matrix can be derived from the strain energy [60]. With zero deformations at one node (cantilever beam) stiffness are:

$$F_y = \frac{12EI_z}{l^3\left(1+P_y\right)} v - \frac{6EI_z}{l^2\left(1+P_y\right)} c \quad or \quad F_y = K_{22}v - K_{26}c \tag{3.6a}$$

$$where \quad K_{22} = \frac{12EI_z}{l^3\left(1+P_y\right)} \quad and \quad K_{26} = \frac{6EI_z}{l^2\left(1+P_y\right)} \tag{3.6b}$$

where F_y is the transverse load to the axis of beam, I_z is the moment of inertia with respect to the z axis, v is the deflection, c is the angle of rotation, K_{22} and K_{26} are bending stiffness and:

$$M_z = -\frac{6EI_z}{l^2\left(1+P_y\right)} v + \frac{\left(4+P_y\right)EI_z}{l\left(1+P_y\right)} c \quad or \quad M_z = -K_{62}v + K_{66}c \tag{3.7a}$$

$$where \quad K_{62} = \frac{6EI_z}{l^2\left(1+P_y\right)} \quad and \quad K_{66} = \frac{\left(4+P_y\right)EI_z}{l\left(1+P_y\right)} \tag{3.7b}$$

where M_z is the bending moment, K_{62} and K_{66} are the bending stiffness. One can see, that with the increasing beam length l, the parameter P_y is reaching zero

($P_y \to 0$) so the effect of shear deflection due to shear force can be neglected and the Euler-Bernoulli stiffness matrices are obtained. In other words, Timoshenko beam theory is more universal and can be used for both slender and stocky beams. Analogically, bending stiffness K_{33}, K_{35}, K_{53} and K_{55} can be estimated like:

$$K_{33} = \frac{12EI_y}{l^3\left(1+P_z\right)} \tag{3.8}$$

$$K_{35} = K_{53} = \frac{6EI_y}{l^2\left(1+P_z\right)} \tag{3.9}$$

$$K_{55} = \frac{\left(4+P_z\right)EI_y}{l\left(1+P_z\right)} \tag{3.10}$$

$$where \quad P_y = \frac{12EI_y f_{s,z}}{GAl^2} \quad and \quad f_{s,z} = \frac{A}{I_y^2}\int_A \frac{Q_y^2}{l_y^2}dA \tag{3.11}$$

Torsion refers to the twisting of a straight bar when it is loaded by moments (or torques) that tend to produce rotation about the longitudinal axis of the beam. The angle of the twist (rotation) a of a bar of linearly elastic material can be related to the applied torque M_x with the use of Hooke's law in shear:

$$M_x = \frac{I_p G}{l}a \tag{3.12a}$$

$$or \quad M_x = K_{44}a \quad where \quad K_{44} = \frac{I_p G}{l} \tag{3.12b}$$

where M_x is the torque, K_{44} is the torsional stiffness and I_p is the polar moment of inertia:

$$I_p = I_y + I_z \tag{3.13}$$

where I_y and I_z are the cross section moments of inertia.

Putting all the above beam deformation relations into the system of linear equations, the following matrices are obtained:

$$\begin{bmatrix} F_x \\ F_y \\ F_z \\ M_x \\ M_y \\ M_z \end{bmatrix} = \begin{bmatrix} K_{11} & 0 & 0 & 0 & 0 & 0 \\ & K_{22} & 0 & 0 & 0 & -K_{26} \\ & & K_{33} & 0 & K_{35} & 0 \\ & & & K_{44} & 0 & 0 \\ & sym. & & & K_{55} & 0 \\ & & & & & K_{66} \end{bmatrix} \begin{bmatrix} u \\ v \\ w \\ a \\ b \\ c \end{bmatrix} \tag{3.14}$$

$$\begin{bmatrix} \frac{AE}{l} & 0 & 0 & 0 & 0 & 0 \\ & \frac{12EIz}{l^3(1+P_y)} & 0 & 0 & 0 & \frac{-6EI_z}{l^2(1+P_y)} \\ & & \frac{12EIy}{l^3(1+P_z)} & 0 & \frac{6EI_y}{l^2(1+P_z)} & 0 \\ & & & \frac{I_pG}{l} & 0 & 0 \\ & sym. & & & \frac{(4+P_z)EI_y}{l(1+P_z)} & 0 \\ & & & & & \frac{(4+P_y)EI_z}{l(1+P_y)} \end{bmatrix} \begin{bmatrix} u \\ v \\ w \\ a \\ b \\ c \end{bmatrix} \tag{3.15}$$

3.2 Piston ring discretization

The whole idea of piston ring discretization is depicted in Fig. 3.2 – the piston ring is divided into n rigid segments (gaps between segments are only for a better demonstration and do not appear in the real model). Each segment is connected with its neighbors by a 6 dimensional spring (6 DOF) characterized by the stiffness matrix presented in (3.15). This approach is greatly supported by MBS named MSC Adams. It allows the definition of such a stiffness matrix in the so-called Field elements. Length l is the distance between the segment cut ends – it can be said, that the piston ring stiffness is represented by a beam of regular convex polygon shape with n sides – n-gon.

For the initial simulations, a piston ring made of very basic structural steel is used: $E = 210000\ MPa$, $\mu = 0.3$ and $\rho = 7850\ kgm^{-3}$. The model of geometry can be seen in Fig. 3.3: $h = 1.2\ mm$, $b = 2.9\ mm$, $d = 76.5\ mm$ and $F_t = 10\ N$.

The local coordinate system is different for each field element and depends on the segment cut plane orientation: x-axis goes along the neutral axis, y-axis aims downward and z-axis points to the center of the piston ring (Fig. 3.2). With respect

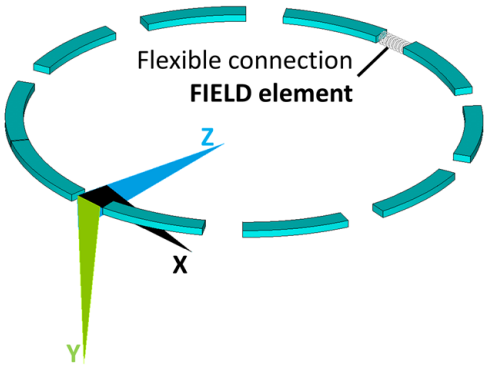

Fig. 3.2: Discretized piston ring model

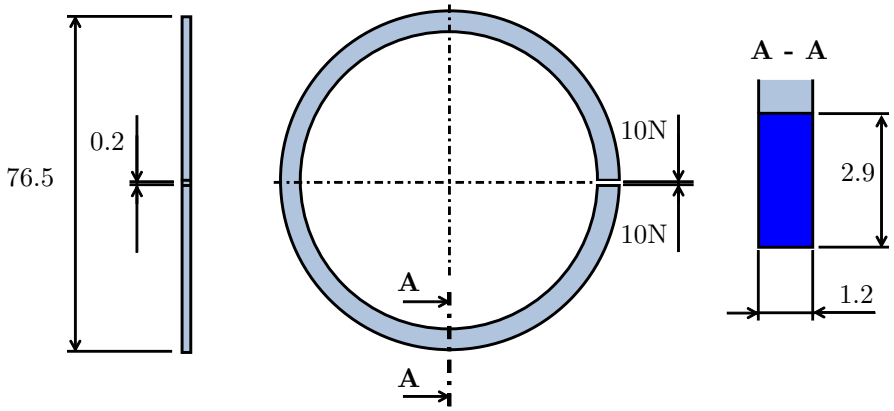

Fig. 3.3: Piston ring model of geometry

for this convection and for the rectangular cross section, the inertia moments can be expressed as follows:

$$I_y = \frac{hb^3}{12} \tag{3.16}$$

$$I_z = \frac{bh^3}{12} \tag{3.17}$$

According to Tab. 3.1 the form factors for rectangular cross section are:

$$f_{s,y} = f_{s,z} = \frac{6}{5} \tag{3.18}$$

All the geometrical and material properties had been listed, so the stiffness matrix (3.15) can be evaluated. Special attention has to be paid to the units:

$$\begin{bmatrix} Force[N] \\ Force[N] \\ Force[N] \\ Torque[Nm] \\ Torque[Nm] \\ Torque[Nm] \end{bmatrix} = \left[\begin{array}{cc} \frac{Force[N]}{Length[m]} & \frac{Force[N]}{Angle[rad]} \\ \hline \frac{Torque[Nm]}{Lenth[m]} & \frac{Torque[Nm]}{Angle[rad]} \end{array}\right] \begin{bmatrix} Length[m] \\ Length[m] \\ Length[m] \\ Angle[rad] \\ Angle[rad] \\ Angle[rad] \end{bmatrix} \tag{3.19}$$

3.3 Stiffness FEM validation

In the previous section, the piston ring was divided into n rigid sections connected by flexible field elements. To confirm the correctness of such an approach, the piston ring shown in Fig. 3.3 is discretized in the FEM software as well. The modal analysis is performed by the FEM and the MBS using a flexible piston ring, and natural frequencies up to 1100 Hz are compared as is explained bellow. The engine firing frequency of typical 4-stroke 4cylinder engine revving 6000 rpm is 200 Hz, which in this application equals to the up-and-down piston ring motion frequency.

For the vibrational modal analysis the equation of motion is mostly given for free vibration without damping as:

$$\mathbf{M}\ddot{\mathbf{U}} + \mathbf{K}\mathbf{U} = \mathbf{0} \tag{3.20}$$

where $\mathbf{M}$ is the mass matrix, $\ddot{\mathbf{U}}$ is the acceleration, $\mathbf{K}$ is the stiffness matrix and $\mathbf{U}$ is the displacement. Assume the displacement $\mathbf{U}$ in a form:

$$\mathbf{U} = \mathbf{U_0} e^{i\Omega t} \tag{3.21}$$

where $\mathbf{U_0}$ is the displacement amplitude, e is the Euler's number, i is the imaginary unit equal to $\sqrt{-1}$, Ω is the natural frequency and t is the time. The first and second derivative of displacement $\mathbf{U}$ are:

$$\dot{\mathbf{U}} = \mathbf{U_0} i\Omega e^{i\Omega t} \tag{3.22}$$

$$\ddot{\mathbf{U}} = \mathbf{U_0} i^2\Omega^2 e^{i\Omega t} \tag{3.23}$$

Using equations (3.23) and (3.21) in (3.20):

$$\mathbf{M}\mathbf{U_0}i^2\Omega^2 e^{i\Omega t} + \mathbf{K}\mathbf{U_0}e^{i\Omega t} = \mathbf{0} \tag{3.24}$$

$$e^{i\Omega t}\mathbf{U_0}\left(-\Omega^2\mathbf{M} + \mathbf{K}\right) = \mathbf{0} \tag{3.25}$$

$$\left(\mathbf{K} - \Omega^2\mathbf{M}\right) = \mathbf{0} \tag{3.26}$$

A non-trivial solution ($\mathbf{U_0} \neq \mathbf{0}$) is found when:

$$det\left(\mathbf{K} - \Omega^2\mathbf{M}\right) = 0 \tag{3.27}$$

The above equation leads to the estimation of the natural frequencies Ω. For the 1 dimension problem, natural frequency is reduced to the well know formula:

$$\Omega = \sqrt{\frac{k}{m}} \tag{3.28}$$

It is clear, that the undamped natural frequencies depend on the stiffness and the mass properties of the object. Discretizing the piston ring did not change its mass properties (no material removal). Therefore, the natural frequency can be used as the parameter suitable for comparing two different stiffness estimation methods while the mass characteristics remain the same.

For the modal analysis with the FEM software discretization, commercially available ANSYS is used. The element shape (tetrahedral, hexahedral etc.), DOF (displacements, rotations, temperature etc.), the order of approximation functions (first – linear, second – quadratic) and the specification (pretension, gasket etc.) defines the element type.

Analysis can be done by BEAM188 or linear SOLID185, but for the best accuracy the quadratic SOLID186 elements are chosen. Material data are listed in section 3.2 and the mesh density is shown in the Fig. 3.4 (75114 nodes and 57720 elements). The analysis is performed as free-free – no displacement constrains, no tangential loads and no symmetry. The first 6 natural frequencies are expected to be approximately zero, since these mode shapes are only the displacements and rotations of the model as a rigid unit. The first non-zero natural frequencies obtained by ANSYS are depicted in Fig. 3.5.

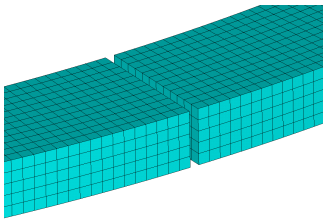

Fig. 3.4: Mesh density for FEM

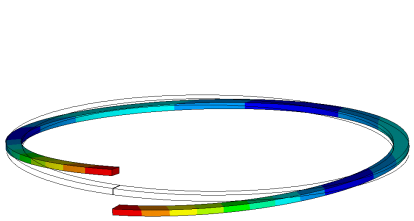

(a) 126 Hz

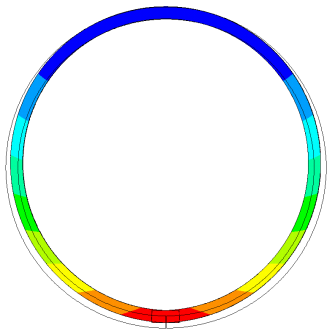

(b) 223 Hz

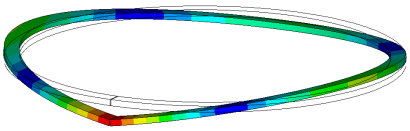

(c) 345 Hz

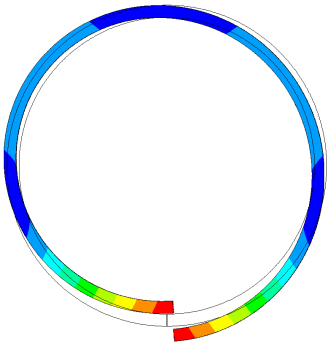

(d) 485 Hz

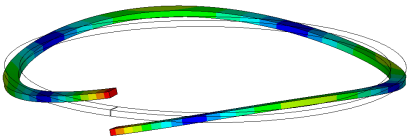

(e) 727 Hz

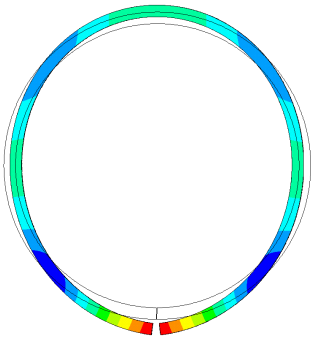

(f) 1089 Hz

Fig. 3.5: First 6 non-zero natural frequencies and mode shapes by FEM

Modal analysis with the same boundary conditions, model of geometry and material is done in MSC Adams using field elements. The piston ring segment count n dependence on the natural frequencies is investigated and shown in graphs Fig. 3.6. Adams natural frequencies limit values for $n \to \infty$ should be the same as those estimated by ANSYS. In case the of the second, fourth and sixth natural frequency it is perfectly true, but in the case of the first, third and fifth natural frequency asymptotes are different. This may be caused by an incorrect stiffness in a field connection of the MBS model.

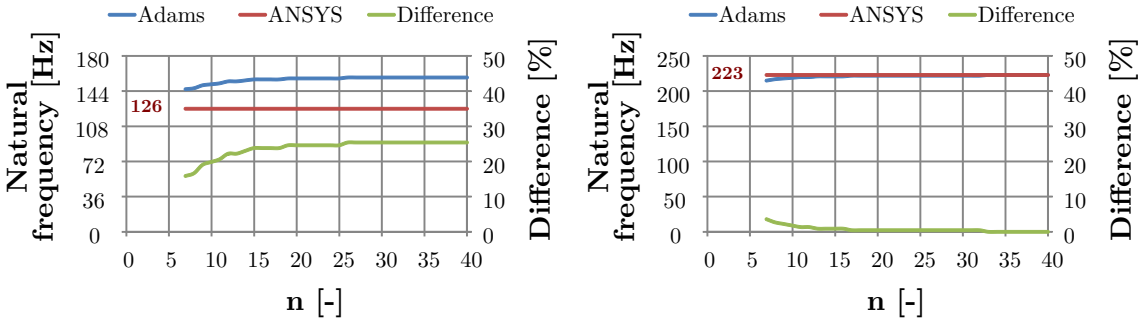

(a) First natural frequency

(b) Second natural frequency

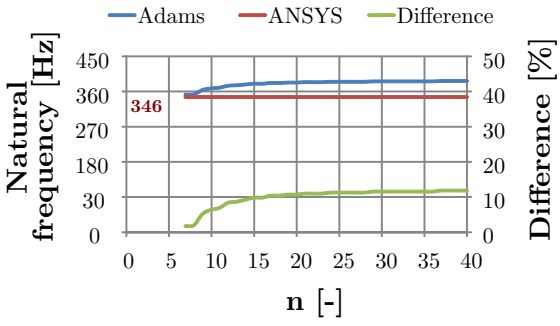

(c) Third natural frequency

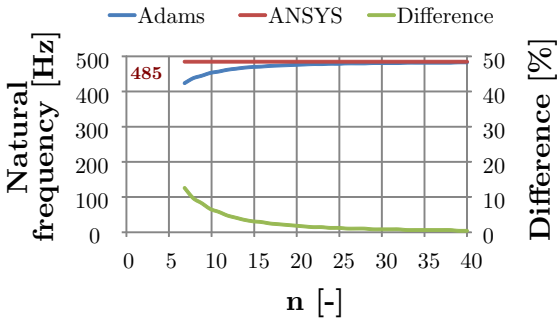

(d) Fourth natural frequency

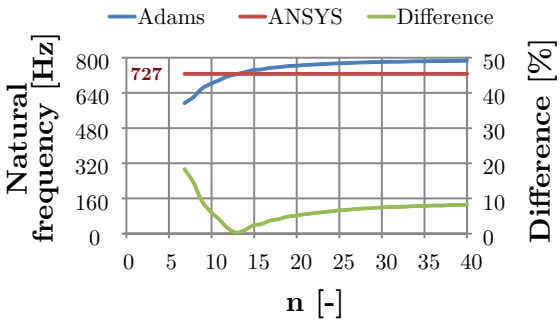

(e) Fifth natural frequency

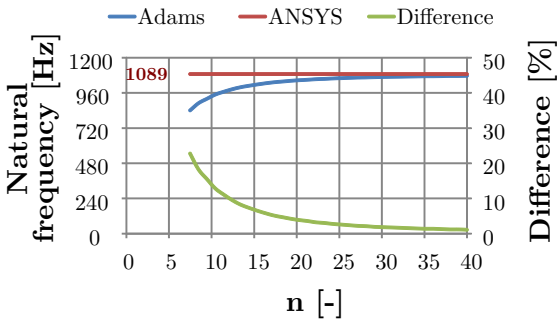

(f) Sixth natural frequency

Fig. 3.6: Adams and ANSYS natural frequencies comparison

The first, the third and the fifth mode shape (Fig. 3.5a, Fig. 3.5c and Fig. 3.10e) may be substituted for the force F_y applied to the ring gap pointing downward (Fig. 3.7) to simulate a similar strain energy. Next, internal forces and moments diagrams are made (Fig. 3.8) to find out which specific stiffness has an impact on this mode shape with an incorrect natural frequency estimated by Adams.

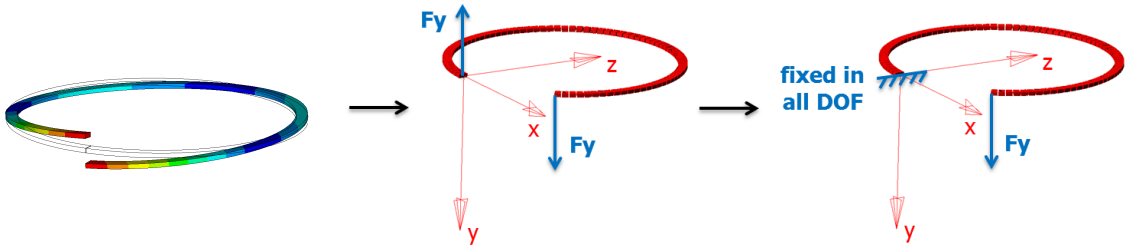

Fig. 3.7: First mode shape force substitution

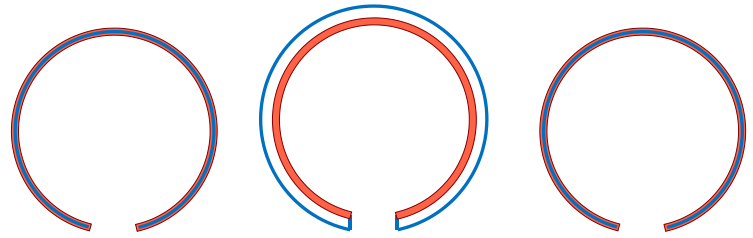

(a) Axial force N (b) Shear force V_y (c) Shear force V_z

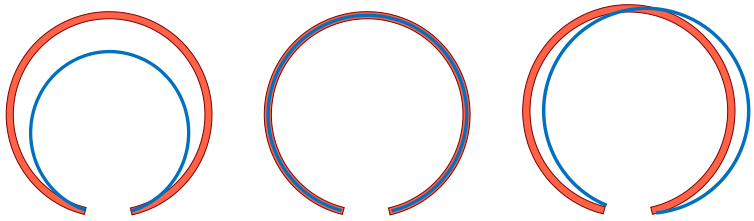

(d) Torque T (e) Bending moment M_y (f) Bending moment M_z

Fig. 3.8: Internal forces and moments diagrams for the first mode shape

The only non-zero portions of internal forces and moments are the shear force V_y, the torque T and the bending moment M_z. These loads are causing deformations v, a and c. Hence, they can be found in K_{22}, K_{26} (K_{62} respectively), K_{44} or K_{66}:

$$\begin{bmatrix} N \\ \mathbf{V_y} \\ V_z \\ \mathbf{T} \\ M_y \\ \mathbf{M_z} \end{bmatrix} = \begin{bmatrix} K_{11} & 0 & 0 & 0 & 0 & 0 \\ & \mathbf{K_{22}} & 0 & 0 & 0 & \mathbf{-K_{26}} \\ & & K_{33} & 0 & K_{35} & 0 \\ & & & \mathbf{K_{44}} & 0 & 0 \\ & sym. & & & K_{55} & 0 \\ & & & & & \mathbf{K_{66}} \end{bmatrix} \begin{bmatrix} u \\ \mathbf{v} \\ w \\ \mathbf{a} \\ b \\ \mathbf{c} \end{bmatrix} \tag{3.29}$$

The same methodology is used for the second mode shape (Fig. 3.5b).

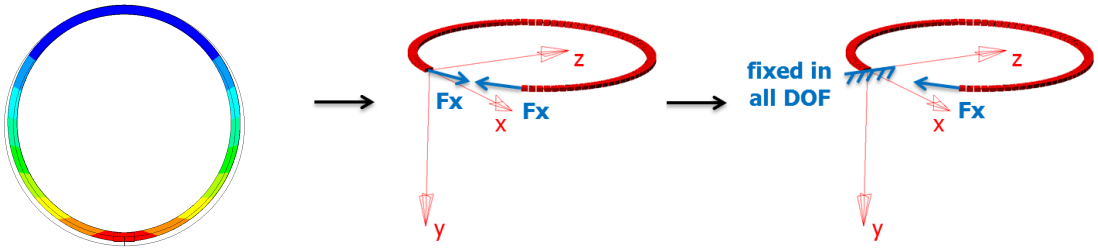

Fig. 3.9: Second mode shape force substitution

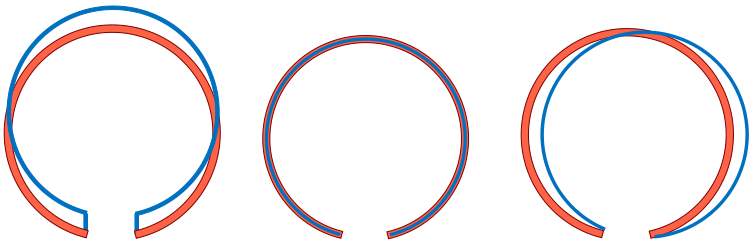

(a) Axial force N (b) Shear force V_y (c) Shear force V_z

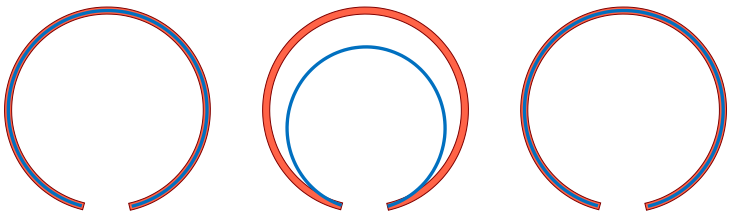

(d) Torque T (e) Bending moment M_y (f) Bending moment M_z

Fig. 3.10: Internal forces and moments diagrams for the second mode shape

In this case the axial force N, the shear force V_z and the bending moment M_y are causing u, w and b deformations. Therefore, only the stiffness K_{11}, K_{33}, K_{35} (K_{53} respectively) and K_{55} take account:

$$\begin{bmatrix} \mathbf{N} \\ V_y \\ \mathbf{V_z} \\ T \\ \mathbf{M_y} \\ M_z \end{bmatrix} = \begin{bmatrix} \mathbf{K_{11}} & 0 & 0 & 0 & 0 & 0 \\ & K_{22} & 0 & 0 & 0 & -K_{26} \\ & & \mathbf{K_{33}} & 0 & \mathbf{K_{35}} & 0 \\ & & & K_{44} & 0 & 0 \\ & sym. & & & \mathbf{K_{55}} & 0 \\ & & & & & K_{66} \end{bmatrix} \begin{bmatrix} \mathbf{u} \\ v \\ \mathbf{w} \\ a \\ \mathbf{b} \\ c \end{bmatrix} \tag{3.30}$$

The second Adams natural frequency is approaching the ANSYS one as discussed before – the stiffness highlighted in (3.30) are correct. The bending stiffness K_{33}, K_{35} (K_{53} respectively) and K_{55} in this mode shape were estimated in the same way (see (3.15)) as the bending stiffness in the first mode, hence K_{22}, K_{26} (K_{62} respectively) and K_{66} are correct as well.

With this elimination method, the only possibly wrong stiffness is the torsional stiffness K_{44} calculated by (3.12b) where the polar moment of inertia I_p is the sum of moments of inertia I_y and I_z (3.13). It is important to emphasize, that this approach can be used only for the torsion of circular bars and tubes, but it is restricted for bars of other shapes. Non-circular bars, such as rectangular bars, behave quite differently. For instance, their cross sections do not remain plane and their maximum stresses are not located at the farthest distances from the midpoints of the cross sections. Thus, these bars require more advanced methods of analysis.

Vlasov [62] presented a method for non-circular bars torsion investigation. For the rectangular shape, a modified polar moment of inertia I_p is used:

$$I_p = \beta b h^3 \tag{3.31}$$

where β is dependent on the b/h ratio as follows:

$\frac{b}{h}$	2	4	6	8	10 and more
β	0.229	0.281	0.3	0.307	$\frac{1}{3}$

Tab. 3.2: β coefficient [62]

The modal analysis in Adams is rerun with the corrected polar moment of inertia value. Results are depicted in Fig. 3.11 and reflect very good correlation between

discretization in MBS and in FEM software. All natural frequencies bellow 1100 Hz estimated by Adams have limit values equal to the frequencies obtained from ANSYS. The piston ring model with segment count n up to 9 have an additional mode shape, which does not appear in the FEM results – insufficient n. On the other hand, too many rigid segments increase the computing time rapidly. Therefore segment count $n = 20$ is estimated as the best compromise between accuracy and computing time, since the differences between Adams and ANSYS results of all 6 natural frequencies are bellow 5 %.

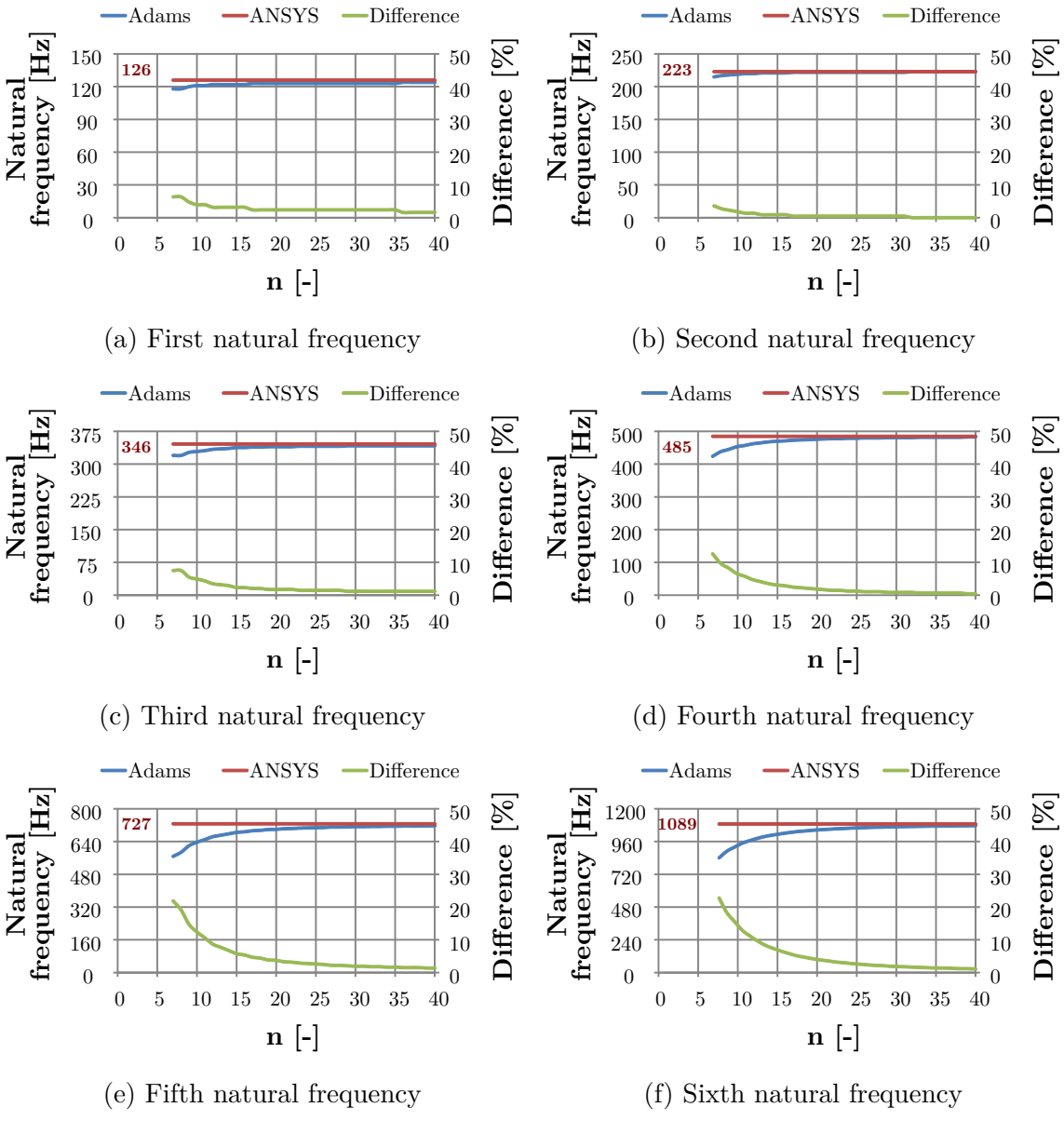

(a) First natural frequency

(b) Second natural frequency

(c) Third natural frequency

(d) Fourth natural frequency

(e) Fifth natural frequency

(f) Sixth natural frequency

Fig. 3.11: Adams and ANSYS natural frequencies comparison after correction for non-circular torsion

3.4 Pretension

Discretized model in MBS was investigated in the closed shape (as shown in Fig. 3.3) without any loads applied so far. However, the closed shape is achieved only from the free shape, where the pretension force is present. The question is, whether the free piston ring shape can be represented by the piston ring in a closed shape with the pretension of opposite direction.

ANSYS is used to gain the free piston ring shape (Fig. 3.12b) from the closed one, by the opposite pretension force (Fig. 3.12a). Then, the strain energy of the free ring shape is set to zero and the geometry is used as an input into the analysis with the correct pretension direction (Fig. 3.12c). This results in another closed shape, but computed as a deformed geometry (Fig. 3.12d). To confirm the substitutability of the free shape by the closed shape with the opposite pretension force, deformed geometry has to be the same as the initial undeformed.

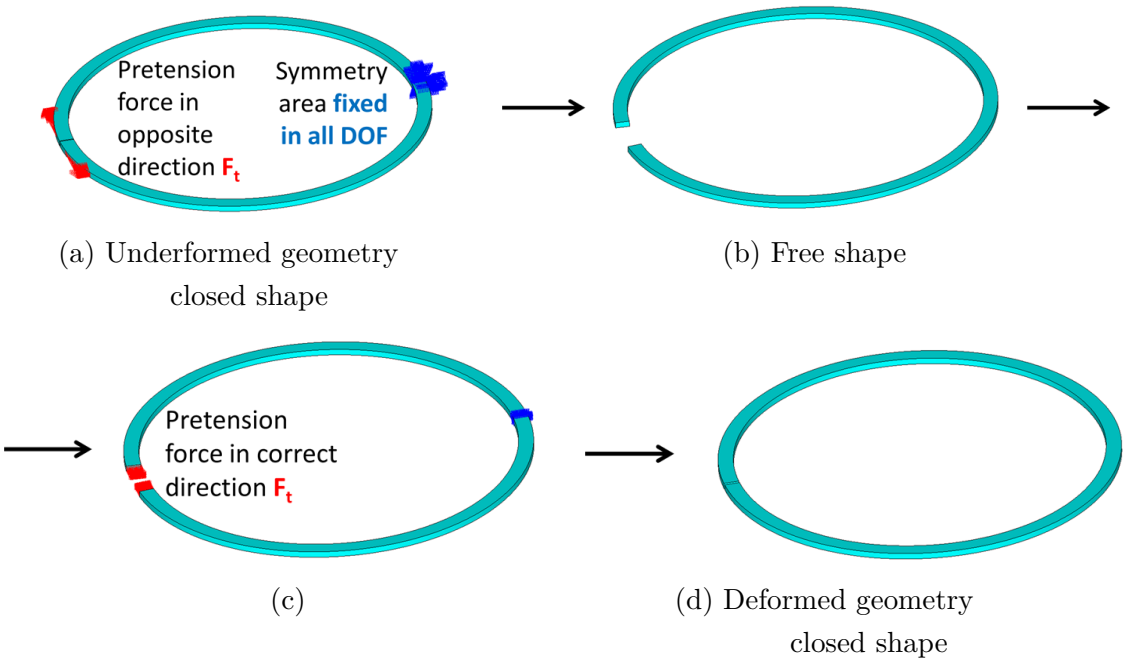

(a) Underformed geometry closed shape

(b) Free shape

(c)

(d) Deformed geometry closed shape

Fig. 3.12: ANSYS iterations for closed geometry creation

The results are represented by the nodes of the inner circumference. The undeformed and deformed geometry lines (Fig. 3.13) are almost the same and the biggest difference is in the ring gap region which may be caused by very close surrounding of the applied force. Since the pretension force is in most cases set with a tolerance of ±20 %, the difference between the results is negligible and it can be said that *free shape = closed shape + pretension in opposite direction.*

It has to be kept in mind that the closed shaped piston ring with the opposite pretension (3.12a) has a totally different strain energy than the free shaped geometry closed by the correctly directed pretension (3.12c). In the first case, the outer fibers are pushed and the inner fibers are pulled (Fig. 3.14a), while in the other case it is the exact opposite (Fig. 3.14b). Fortunately, this phenomenon does not affect the dynamics and external behaviour of the piston ring so a closed shaped piston ring with an opposite pretension can be used as it is presented. To simplify the text further, consider the term "pretension" as "pretension in opposite direction".

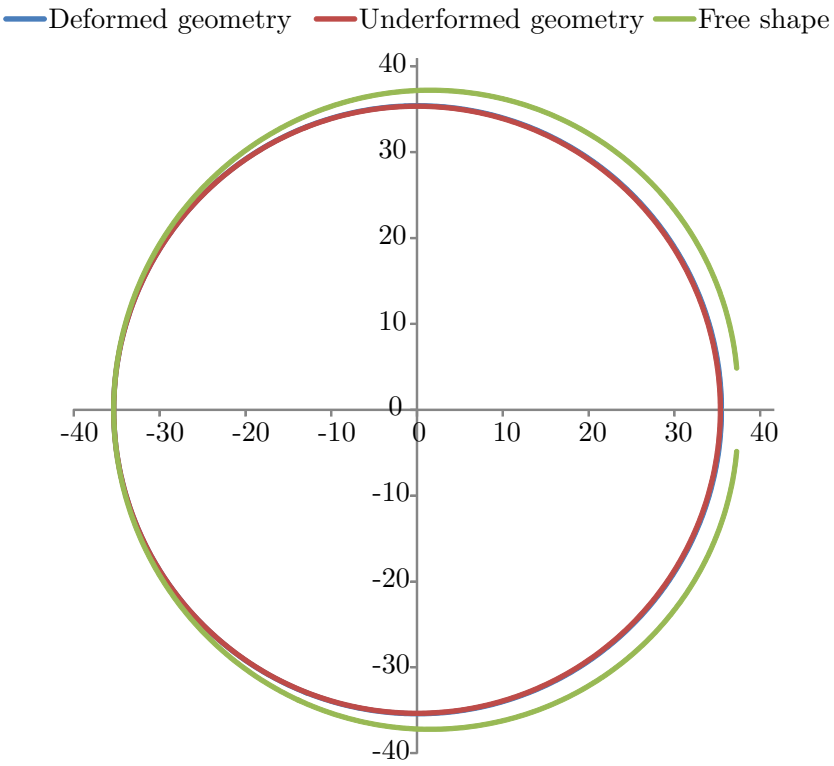

Fig. 3.13: Underformed and deformed piston ring geometry comparison

Two ways of the piston ring pretension modeling are feasible - a force and field method. The force method uses the application of pretension forces on the ring gaps in neutral axis directions like depicted in Fig. (3.12). The unconventional field method creates pretension via the field element with an adequate pretension force. For determining the best method, the following comparison analysis are done.

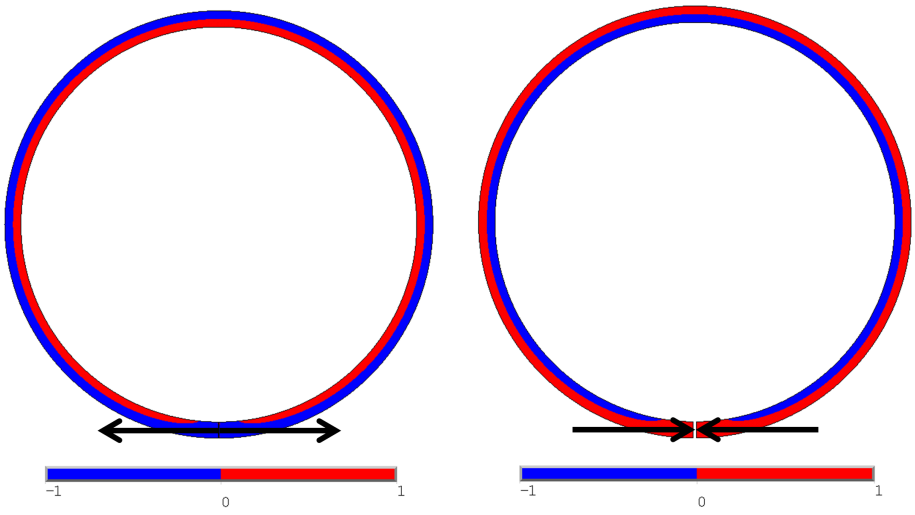

(a) Closed geometry with opposite pretension

(b) Free geometry with correct pretension

Fig. 3.14: Stress distribution

3.4.1 Axial loading

First of all, an FEM solution in ANSYS is performed. The boundary conditions are indentical to Fig. 3.12a. The analysis with the same conditions is simulated in Adams, one with the force pretension and the other with the field pretension. Then, the axial ring gap openings on the inner circumference x_a (Fig. 3.15) are compared. ANSYS should result in the the biggest opening distance, because this region is highly affected by boundary conditions – force applied. On the other hand, Adams should give a smaller x_a than ANSYS since the model of rigid segment suppresses the boundary conditions effect on the near surroundings – Saint-Venant's principle.

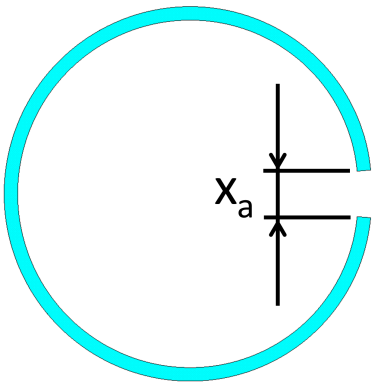

Fig. 3.15: Ring gap opening x_a

	ANSYS	Adams – force pretension	Adams – field pretension
x_a	9.72 mm	9.42 mm	9.71 mm
Difference	-	3.07 %	0.07 %

Tab. 3.3: Ring gap opening after axial loading for different methods

At first glance, better results are obtained via the Adams field pretension. However, to make a final statement, more investigation is needed.

3.4.2 Combined loading

Combined loading is meant as the axial (force and field pretension) and the lateral force applied simultaneously (Fig. 3.16). The observed parameter is the axial ring gap opening on the inner circumference and the top side x_c in the direction shown in Fig. 3.17. The free shape piston ring geometry is used for the ANSYS simulation, taking into account the previously confirmed substitutability. Three cases for the different lateral loads are investigated.

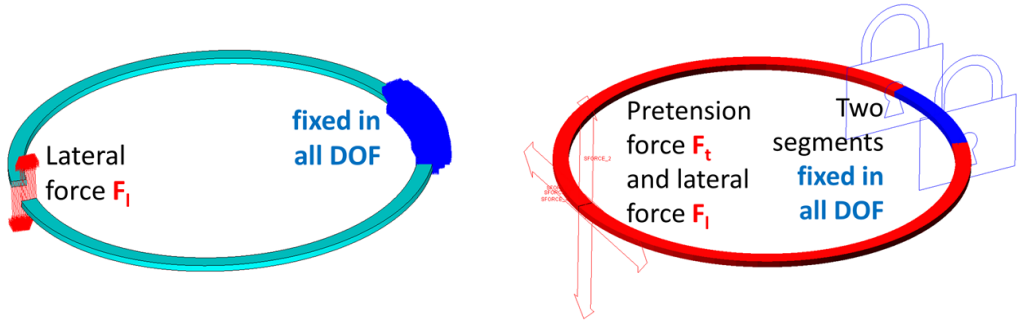

(a) ANSYS (b) Adams

Fig. 3.16: Boundary conditions for combined loading analysis

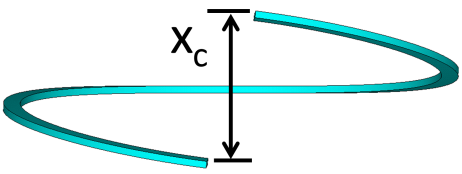

Fig. 3.17: Ring gap opening x_c

Tab. 3.4 does not reflect such optimistic results in the case of a field pretensioned piston ring, like it was in the axially loaded analysis. The difference is almost 44 %.

A field element applies a translational and rotational action-reaction force between two locations. Adams creates markers (coordinate systems) at each location. The marker specified on the first location is called the I marker. The marker specified on the second location is called the J marker. Adams computes all variables and time derivatives in the J marker coordinate system [61]. This explains the higher opening distance in the case of field pretensioning. The pretension force applied on the J marker side of the piston ring gap is in the direction of the neutral axis. But it is not for the I marker side, since it is twisted by some angle – a portion of the pretension force becomes the lateral load (Fig. 3.18). In the case of force pretension, it stays perpendicular to both piston ring gap faces through any deformation.

F_l		ANSYS	Adams – force pret.	Adams – field pret.
5 N	x_c	25.01 mm	25.44 mm	32.78 mm
	Difference	-	1.72 %	31.07 %
0.1 N	x_c	0.513 mm	0.515 mm	0.737 mm
	Difference	-	0.39 %	43.64 %
0.006 N	x_c	0.0308 mm	0.0309 mm	0.0442 mm
	Difference	-	0.39 %	43.65 %

Tab. 3.4: Ring gap opening after combined loading for different methods

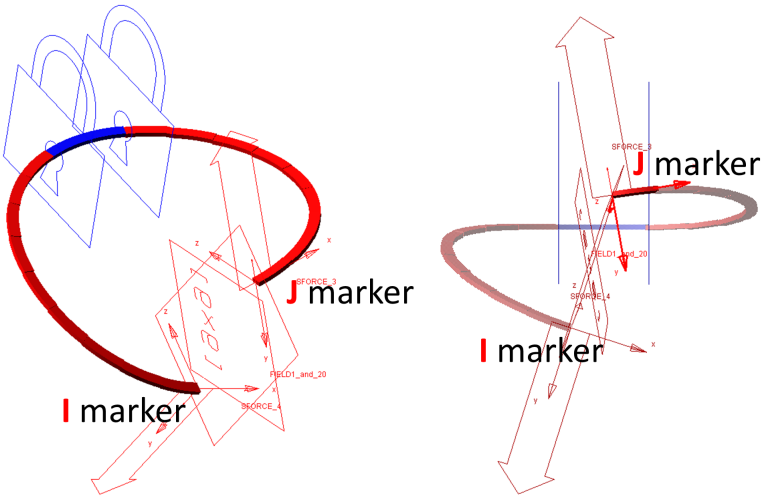

Fig. 3.18: Field element behaviour

The lateral force 0.006 N is not set by coincidence. Side clearance between the piston ring gap and the piston ring groove is usually 0.03 mm for this piston ring size. With the field pretensioned model, the lateral force causing the piston ring to

get stuck would be much smaller and would not represent reality. For a very good correlation between FEM model, the force pretension is recommended and used in next simulations.

3.4.3 Contact analysis

Contact analysis between the piston ring/cylinder liner (same diameter as a piston ring) is performed in order to discover differences between the contact pressure distribution estimated by the FEM and the MBS software. The results are augmented by an analytical solution (1.3). In ANSYS, a rigid target and pretension force applied to the close shaped piston ring are used. In addition, the analysis takes advantage of symmetry (Fig. 3.19a). For Adams, the piston ring uses force pretension and has a constrained motions parallel to the cylinder liner axis. Symmetry boundary condition is also applied (three segment nodes in the middle are constrained to move only within the symmetry plane) as depicted in Fig. 3.19b.

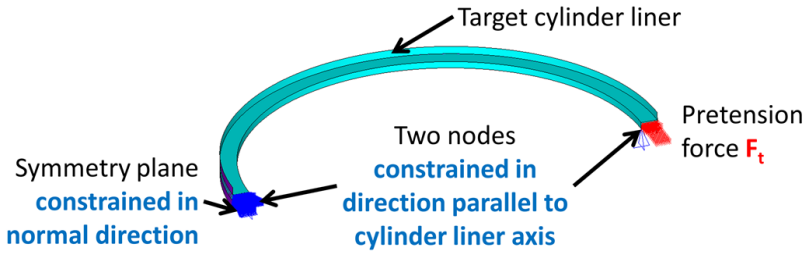

(a) ANSYS

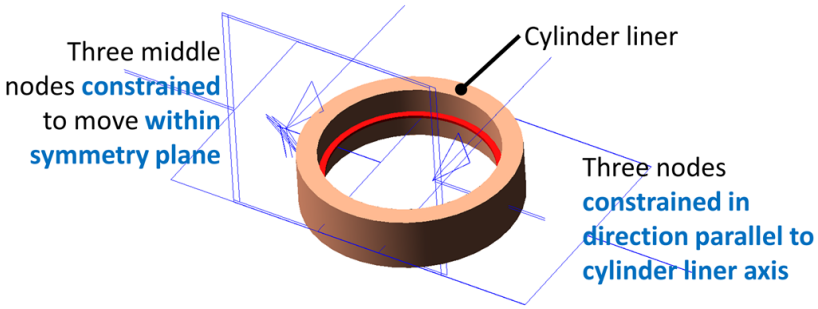

(b) Adams

Fig. 3.19: Boundary conditions for contact analysis

The contact pressure computed by Adams is very sensitive to the cylinder liner geometry – surface segment count (Fig. 3.20, not to be mistaken for the rigid piston ring segments count n). For the segment count bellow 400, contact pressure varies along the circumference. Segment count above 500 shows stabilized results and therefore this count is used in the next analysis.

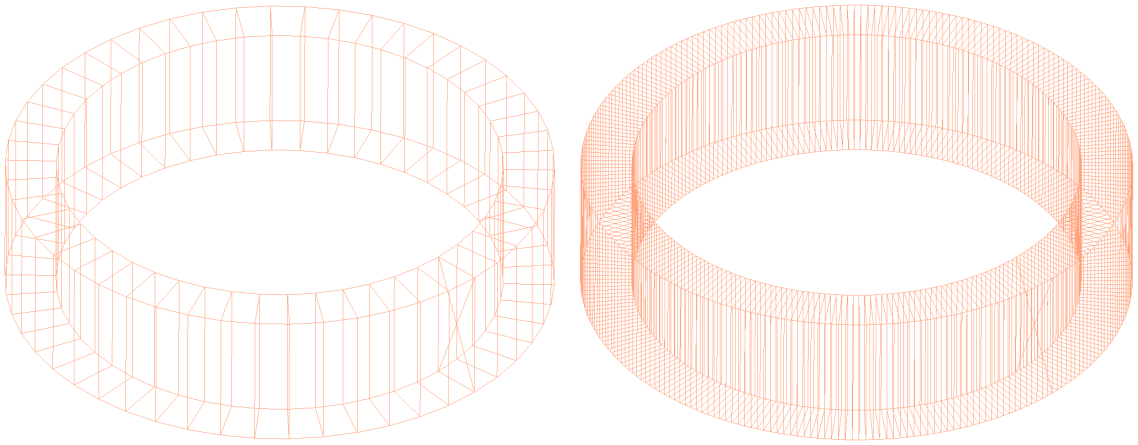

(a) Segment count 50 (b) Segment count 250

Fig. 3.20: Cylinder liner geometry

Results available in Fig. 3.21 correlate very well with each other – the piston ring discretization in MBS is adequate and does represent a much larger FEM model with only $n = 20$ rigid piston ring segments excelently. The ring gap region (0 deg and 360 deg) is the most affected area by the force applied, hence there is the biggest difference in comparison with the analytical solution.

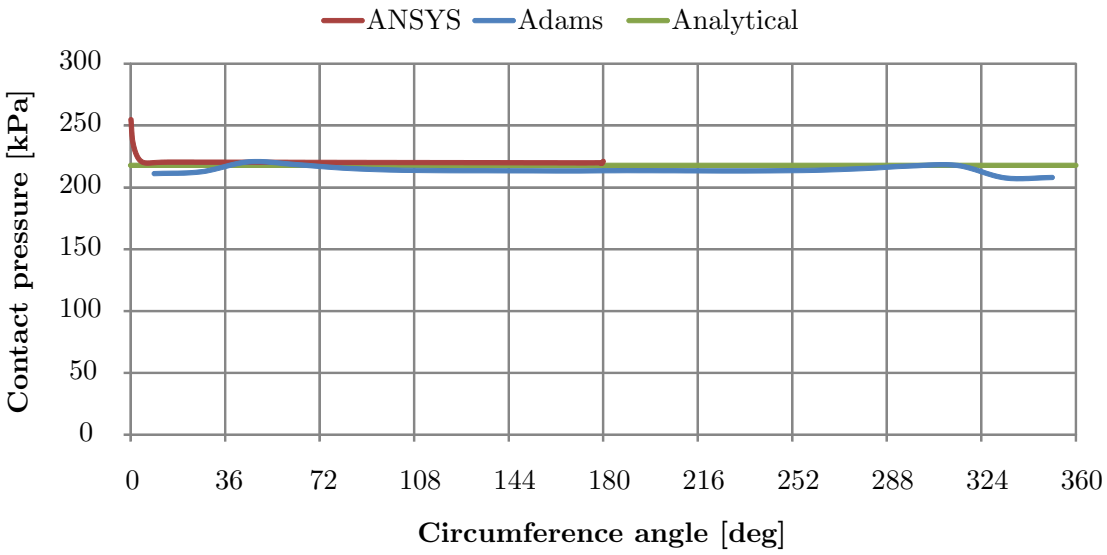

Fig. 3.21: Contact pressure

3.5 Piston assembly/cylinder liner model

The piston ring behaviour is investigated on the model depicted in Fig. 3.22a (cylinder liner is drawn only as a plane, but the actual shape is hollowed cylinder – Fig. 3.20). To simulate the worst case, the piston ring and piston dimensions were set, according to the tolerances, to create the biggest possible gaps (Fig. 3.22b). The piston is constrained to move only vertically and the motion is applied as the displacement function of the crank mechanism in the piston pin (1.6). Half of the stroke is $r = 43.45\ mm$ and the rod length $l = 130\ mm$. The initial piston position is TDC (Fig. 3.23) and at the start of the simulation, the piston ring lays on the bottom side of the piston ring groove.

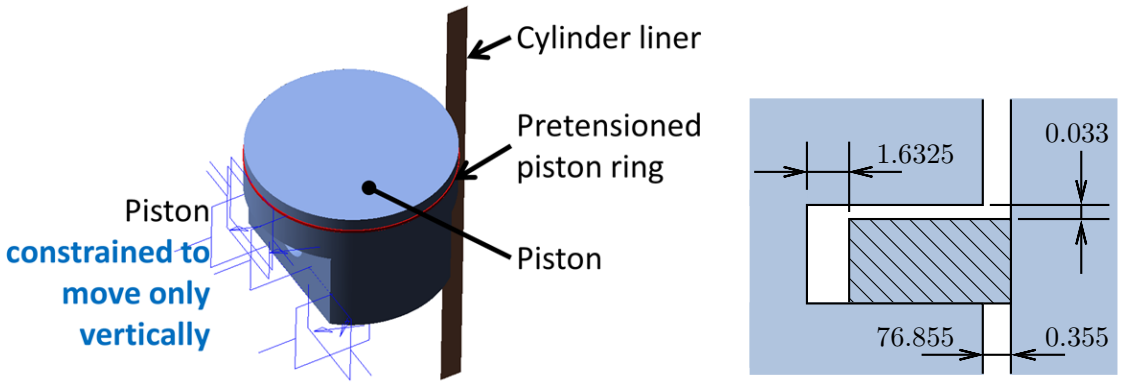

(a) Boudary conditions (b) Gap dimensions

Fig. 3.22: Assembly model

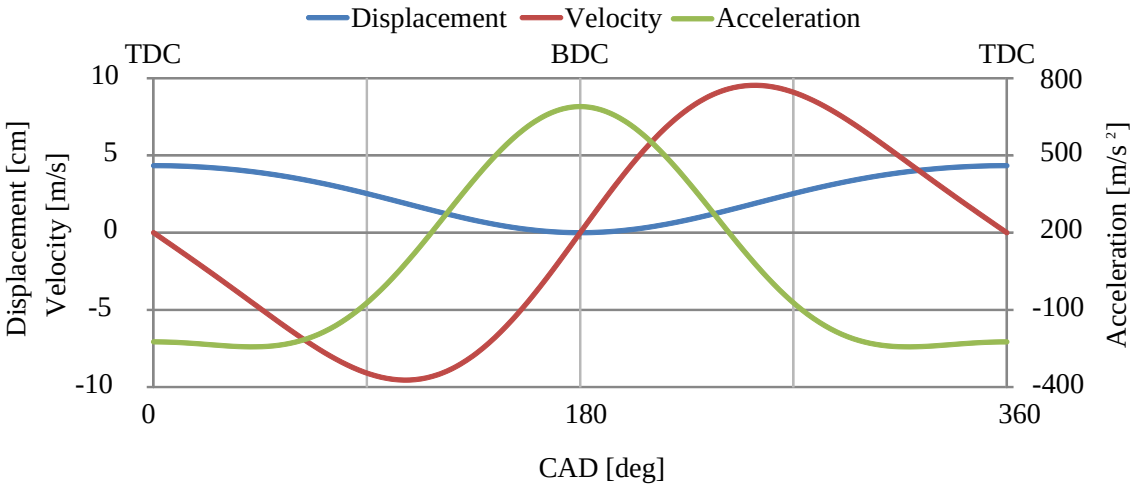

Fig. 3.23: Piston motion characteristics for $n = 1000\ rpm$

3.5.1 Assembly model with inertia only

No friction and no gas pressure is present. The predicted piston ring motion is a slap-motion from the bottom to the top position in the piston groove. This prediction is fulfilled in the case of higher rotary speed $n = 1000\ rpm$ (Fig. 3.24), where the piston ring motion reflects the piston acceleration – whenever the piston changes the acceleration from positive to negative and reversely, the piston ring changes its position as well. For the low rotary speeds ($n = 40\ rpm$), inertia forces are insufficient to cause such motion and the piston ring gets angularly stuck (Fig. 3.25 and Fig. 3.26).

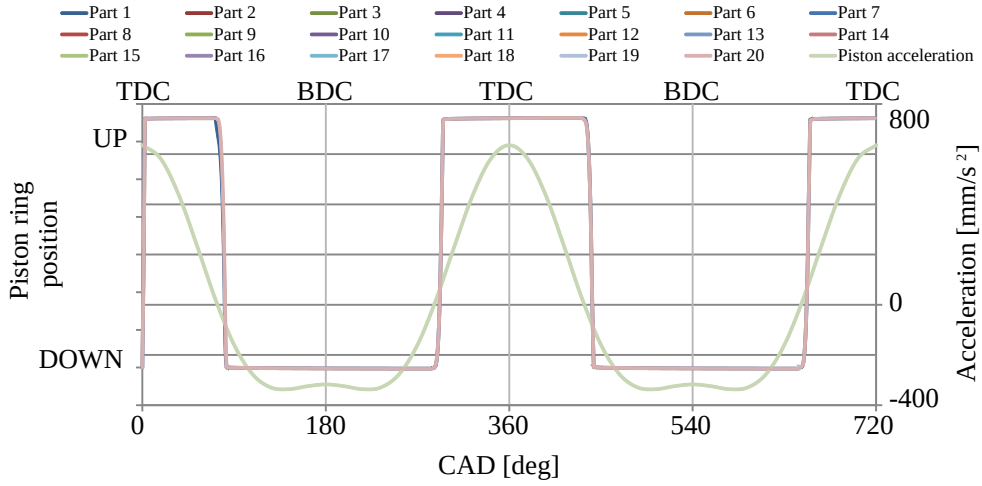

Fig. 3.24: Inertia piston ring motion for $n = 1000\ rpm$

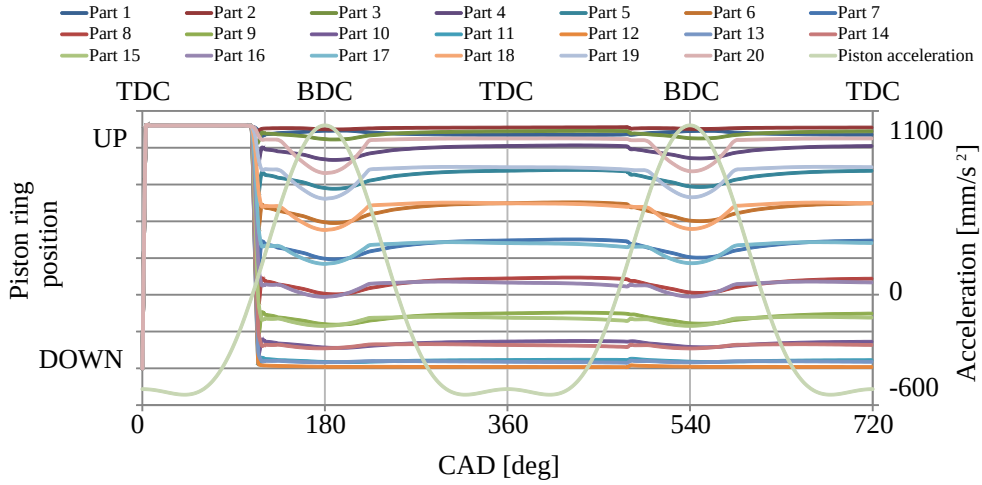

Fig. 3.25: Inertia piston ring motion for $n = 40\ rpm$

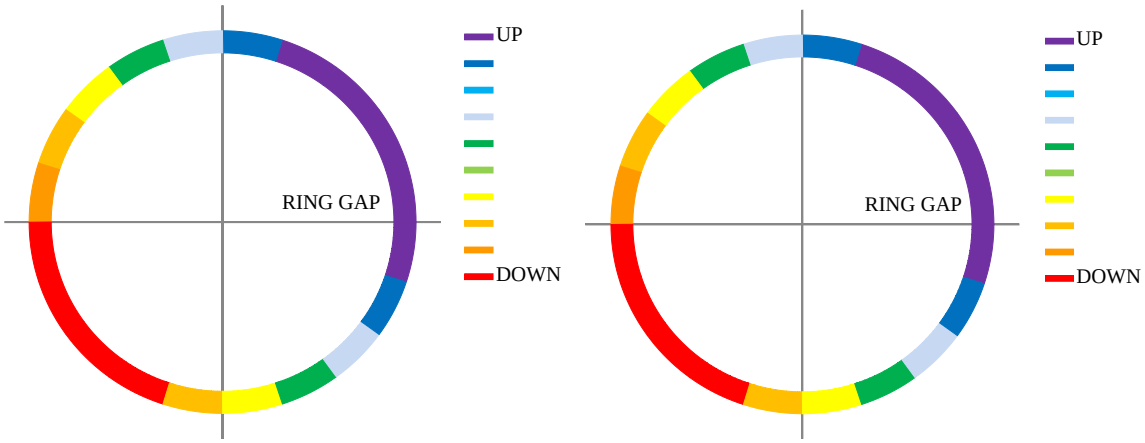

(a) $CAD = 180\ deg$ (b) $CAD = 360\ deg$

Fig. 3.26: Stuck piston ring

3.5.2 Assembly model with friction

The friction force is specified by the coefficient of friction (2.8), considered as a constant value $C = 10$ according to Andersson et al. [1]. The piston ring motion should reflect the piston velocity, unlike the previous model. Whenever the piston changes its velocity from positive to negative, the friction force changes its orientation as well and therefore tends to move the piston ring in the opposite direction. It is confirmed by simulation results (Fig. 3.27).

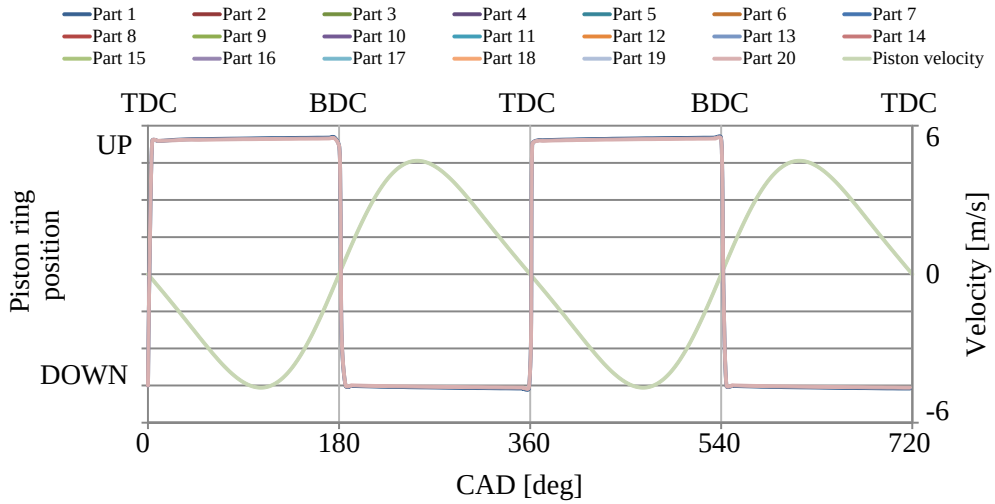

Fig. 3.27: Friction piston ring motion for $n = 1000\ rpm$

3.5.3 Assembly model with friction and gas pressure

Three gas pressure forces are applied on the piston ring surfaces (Fig. 3.28). First of all, the gas pressure force behind the first piston ring in the axial direction $F_{a,P3}$ is applied to the top side of the ring. Next, the gas pressure force behind the first piston ring in the radial direction $F_{r,P3}$ is applied to the back side of the ring. Last of all, the gas pressure force behind the second piston ring in the axial direction $F_{a,P5}$ is applied to the bottom side of the ring. All forces are applied in the center of gravity. Gas pressure values are depicted in Fig. 1.6.

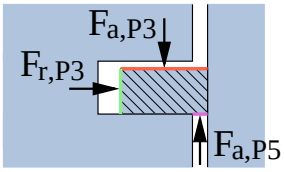

Fig. 3.28: Gas pressure forces

The gas pressure forces are equal to the pressure acting on the constant surface. And that is the stumbling block of this approach. The piston ring area affected by the gas pressure varies throughout the engine operation cycle and it is not constant at all. During the intake stroke, the piston ring should be sucked to the top side of the piston groove like Isarai et al. [53] presented (Fig. 2.13). Since the force $F_{a,P5}$ is applied on a much smaller area than the force $F_{a,P3}$ having the opposite direction, it is unable to cause the piston ring to move vertically even if it has the support of the friction and inertia forces (Fig. 3.29).

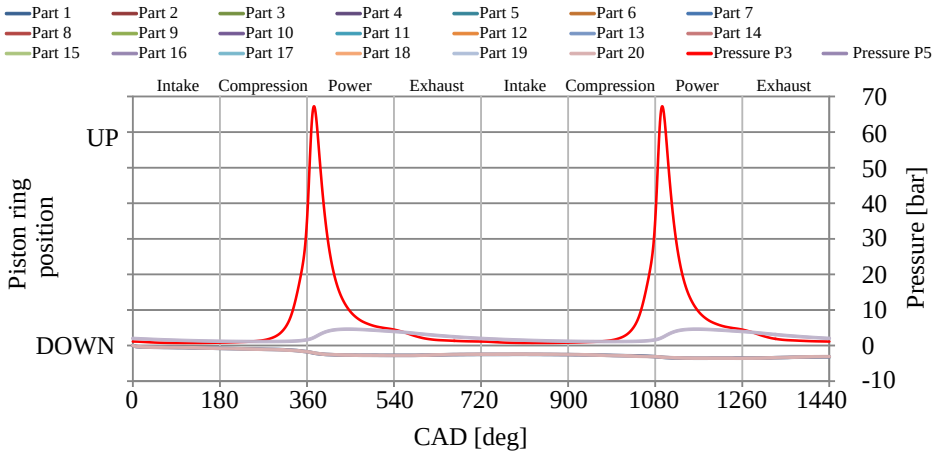

Fig. 3.29: Piston motion with friction and gas pressures applied for $n = 1000\ rpm$

When higher rotary speed is present ($n = 6000\ rpm$), the inertia and friction forces after a certain threshold overcome the force $F_{a,P3}$ and the piston ring moves upwards (Fig. 3.30). This happens only at the end of the exhaust and the beginning of the intake stroke - the proportion of the cycle, where the acceleration is big and conversely, the $P3$ pressure is small. The active gas pressure areas are changed, but since the forces $F_{a,P3}$ and $F_{a,P5}$ are calculated from the initial state, the piston ring moves downward whenever the gas pressure $P3$ is higher.

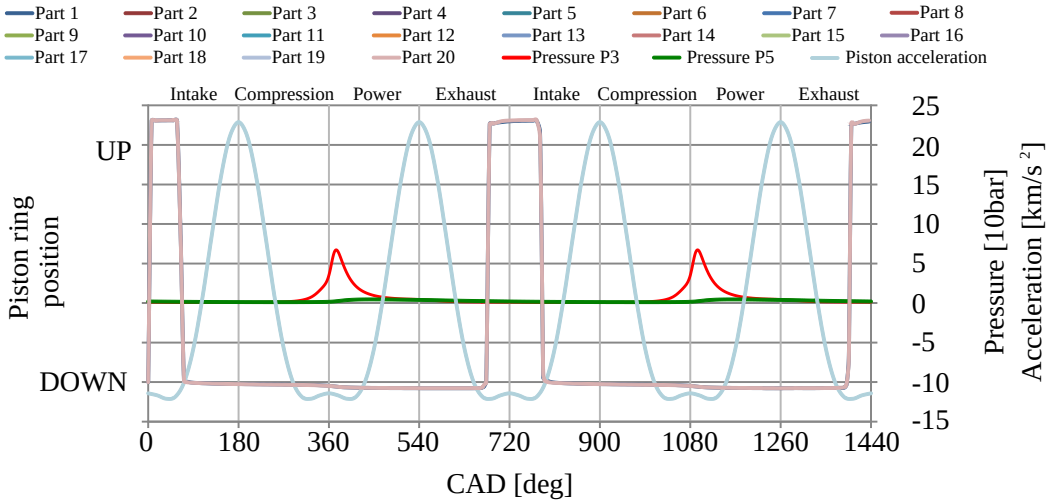

Fig. 3.30: Piston motion with friction and gas pressures applied for $n = 6000\ rpm$

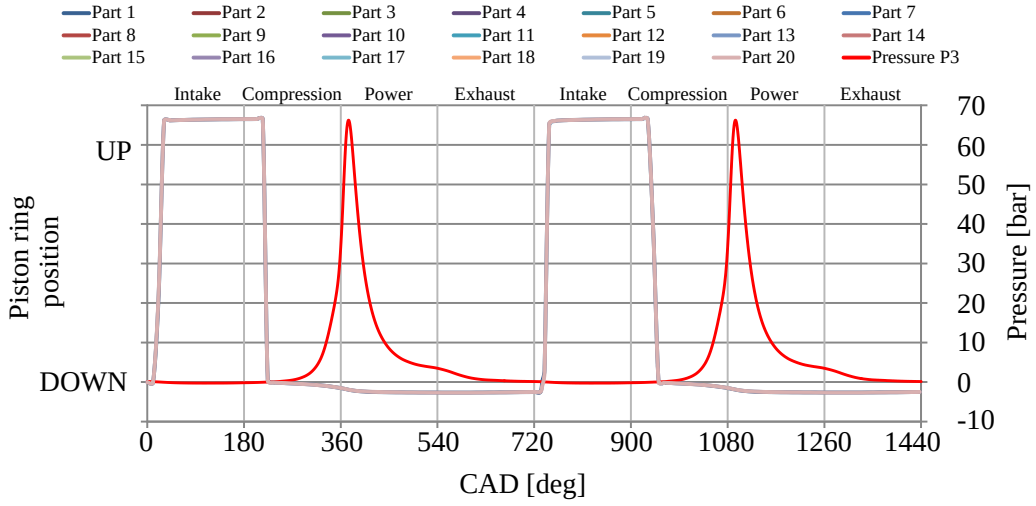

Fig. 3.31: Piston motion with friction and decreased gas pressure applied for $n = 1000\ rpm$

For the suction simulation, the gas pressure behind the compression ring $P3$ is lowered by the atmospheric pressure 1 *bar* – pressure behind the first piston ring is negative during the intake stroke and therefore should cause an upward piston ring motion. Pressure behind the second ring $P5$ is in this case neglected (set to zero).

Results in Fig. 3.31 confirm that the piston ring is able to get sucked to the top side after a sufficient gas pressure effect application. To ensure proper behavior, the iterative gas pressure force evaluation, depending on the active area, is mandatory.

4 CONCLUSION

In the first part of the thesis, current research is presented to see how the engineering society deals with this very actual piston ring dynamics issue. However, the main contribution of the thesis is the flexible piston ring model – the piston ring is discretized by n rigid segments connected by flexible elements, which use the Timoshenko beam theory for the stiffness matrix estimation. The reason for such an approach is to keep the piston ring model within a single software to minimize possible user errors and the number of licenses needed. In addition, the developed method is very quick and automatized, because the whole algorithm is programmed in the command file. The inputs are the piston ring radial wall thickness b, the axial width h, the closed gap distance, the nominal diameter d, the pretension force F_t, the material characteristics E, ρ and μ and the segment count n.

The vibrational modal analysis are performed in order to find out the segment count's impact on the piston ring stiffness. With $n \to \infty$, the natural frequencies from MBS are reaching the values estimated by FEM (Fig. 3.11). For the best compromise between accuracy and computing time, the segment count is set to $n = 20$ – up to a 5 % difference between the Adams and the ANSYS results of the first 6 natural frequencies.

For pretension modelling, the force method is prefered. The field method of pretensioning results in incorrect deformations caused by the essential behavior of the field element. Next, the contact analysis is performed to compare the three different contact pressure evaluation methods – FEM, MBS with the flexible piston ring and analytical. All three methods give approximately the same values as depicted in Fig. 3.21.

The developed and validated flexible piston ring model serves as a base for further more complex piston ring dynamics modeling, which should be similar to the one presented in section 2.4. On each piston ring rigid segment, i nodes (markers, local coordinate systems) are generated and then equilibrium equations are formed and solved. Such an approach leads to a model able to work with distorted bore shapes or able to include the twist effects of the unsymmetrical ring cross sections (L-shaped, tapered etc.).

Suggested improvements :

- iterative gas pressure active area evaluation (Fig. 3.28),
- lubrication force implementation (Reynolds' equation solution needed),
- blow-by model improvement by estimation of the actual flowing volume near the piston ring,
- piston tilt motion (Fig. 1.14),

- model with a distorted bore shape – structural and thermal deformation,
- observation of other ring shapes,
- graphics user interface for inputs entering.

BIBLIOGRAPHY

[1] Andersson, P., Tamminen, J., Sanström, C., Piston ring tribology, VTT Research Notes 2178, 2002. [ISBN 951-38-6107-4]

[2] Hebei Jitie Group Company, *Piston ring* [online]. 2011, [cit. 2014-03-08]. Available at URL: <http://www.jitiegroup.com/detail_16.html>.

[3] European Commission, *Road transport: Reducing CO2 emissions from vehicles* [online]. 2014, [cit. 2014-03-12]. Available at URL: <http://ec.europa.eu/clima/policies/transport/vehicles/index_en.htm>.

[4] Cummins Ltd., *What is Euro 6?* [online]. 2011, [cit. 2014-03-12]. Available at URL: <http://www.cumminseuro6.com/customise/upload/files/20_a.pdf>.

[5] Novotný, P., Píštěk, V., Svída, D., Solution of powertrain friction losses by virtual engine. MECCA - Journal of Middle European Costruction and Design of Cars. 2010. p. 12 - 61. [ISSN 1214-0821]

[6] Skytte af Sätra, Wear of piston rings in hydrostatic transmissions. Doctoral thesis, Royal Institute of Technology Stockholm, 2005. [ISBN 91-7178-148-X]

[7] Ramsbottom, J., On an improved piston for steam engines, Proc. Instn. Mech. Eng. 1854 70–74.

[8] Ramsbottom, J., On the construction of packing rings for pistons, Proc. Inst. Mech. Eng. 1855 206–208.

[9] Miller, G. M., On a packing for pistons of steam engines and pumps, Proc. Inst. Mech. Eng. 1862.

[10] Richardson, D. E., Comparison of measured and theoretical inter-ring gas pressure on a diesel engine, Society of Automotive Engineers, Inc., 1996, SAE Technical Papers Series 961909, pp. 7–20.

[11] Mikhail A. E., Harold J. S., Lawrence J. B., Modeling of ring twist for an IC engine, Society of Automotive Engineers, Inc., 1998, SAE Technical Paper 982693.

[12] Furuhama, S., Ichikawa, H., L-Ring Effect on Air-Cooled Two-Stroke Gasoline Engines, Society of Automotive Engineers, Inc., 1973, SAE Technical Paper 730188.

[13] Federal Mogul, *Piston Ring Handbook* [online]. 2004, [cit. 2014-03-08]. Available at URL: <http://korihandbook.federalmogul.com/en/index.htm>.

[14] Ortjohann, T., Simulation der Kolbenringdynamik auf der Basis expliziter FEM-Software, Dissertation. Aachen, 2006.

[15] Dowson, D., Piston assemblies; background and lubrication analysis. In: Taylor, C.M. (ed.). Engine Tribology. Elsevier, Tribology series, 26, pp. 213–240, 1193. [ISBN 0-444-89755-0]

[16] Tomanik, E., Piston Ring Conformability in a Distorted Bore, Society of Automotive Engineers, Inc., 1996, SAE Technical Paper 960356. z

[17] Rauscher, J., Vozidlové motory. VUT FSI Brno, 2004.

[18] Haddad, S. D., Tjan, K. T., An analytical study of offset piston and crankshaft designs and the effect of oil film on piston slap excitation in a diesel engine. Mechanism and Machine Theory, 30(1995)2, pp. 271–284.

[19] Rauscher, J., Spalovací motory. VUT FSI Brno, 2005.

[20] NMCA, *The Ring of Fire* [online]. [cit. 2014-03-15]. Available at URL: <http://www.nmcadigital.com/2012/03/29/the-ring-of-fire/>.

[21] Mohannad Abdullah Hakeem, Intricate Dynamics and hydrodynamic frictional losses of the piston-ring assembly in internal combustion engines. PH.D. dissertation, Wayne State University Detroit, Michigan, 2011.

[22] Taylor, C. M., Automobile Engine Tribology – Design Considerations for Efficiency and Durability, Wear, 1998, Vol. 221, pp. 1-8.

[23] Dowson, D., Ruddy, B. L., Economou, P. N., The Elastohydrodynamic Lubrication of Piston Rings, Proceedings of the Royal Society of London, 1983, Vol. A386, pp. 409-430.

[24] Yilmaz, E., Sources and Characteristics of Oil Consumption in a Spark-Ignition Engine. PH.D. dissertation, Massachusetts Institute of Technology, 2003.

[25] Ariga, S., Observation of transient oil consumption with in-cylinder variables. Society of Automotive Engineers, Inc., 1996, SAE Paper 961910, pp. 21–32.

[26] De Petris, C., Giglio, V., Police, G., Some insights on mechanisms of oil consumption. 1996. Society of Automotive Engineers, Inc., 1996, SAE Technical Paper Series 961216. 13 p.

[27] Esser, J., Oil control rings and their effect on oil consumption. MTZ Worldwide, 63(2002)7–8, pp. 22–25 / MTZ, 63(2002)7–8, pp. 592–601.

[28] Shayler, P., Allen, A., Leong, D., Pegg, I., Brown, A., Dumenil, J. C., Characterizing Lubricating Oil Viscosity to Describe Effects on Engine Friction. SAE Technical Paper 2007-01-1984, SAE International 2007.

[29] Gamma Technologies, Inc.: Software GT-POWER User's Manual version 6.2, September 2006.

[30] Wannatong, K., Chanchaona, S., Sanitjai, S., Simulation Algorithm for Piston Ring Dynamics, Simulation Modelling Practice and Theory, Vol. 16, pp. 127-146, 2008.

[31] Tain, T.,Noordzij, L. B., Wong, V., Heywood, J. B., Modeling piston ring dynamics, blow-by, and ring-twist effects, ASME, J. Eng. Gas Turbines Power, 120, pp. 843–854, 1998.

[32] Mittler, R., Mierbach., A., Richardson, D., Understanding the fundamentals of piston ring axial motion and twist and the effects on blow-by, ASME 2009 Internal Combustion Engine Division Spring Technical Conference, pp. 721-735.

[33] Novotný, P., Píštěk, V., Drápal, L., Modeling of piston ring pack dynamics, Journal of Middle European Construction and Design of Cars. Vol. 9, Iss. 2, pp. 8–13, 2012. [ISSN 1214-0821]

[34] Vyas, Prerit, Effects of Stochastic (Random) Surface Roughness on Hydrodynamic Lubrication of Deterministic Asperity. Master's thesis, University of Kentucky, 2005.

[35] Patir, N, Cheng, H. S., An Average Flow Model for Determining Effects of Three Dimensional Roughness on Partial Hydrodynamic Lubrication. ASME Journal of Lubrication Technology, 100, p 12-17.

[36] Novotný, P., Píštěk, V., Drápal, L., Ambróz, R., Modern computational approaches to powertrain mechanical loss solution. Perners' Contacts. 2010. pp. 159-458. [ISSN 1801-674X]

[37] Greenwood, J. A., Tripp, J. H., The Contact of two Nominally Flat Rough Surfaces, In: Proc. Instn. Mech., 1970.

[38] Yun, J. E., Chung, Y., Chun, S. M., Lee, K. Y., An Application of Simplified Average Reynolds Equation for Mixed Lubrication Analysis of Piston ring Assembly in an Internal Combustion Engine, SAE Paper 952562, 1995.

[39] Arcoumanis, C., Ostovar, P., Mortler, R., Mixed Lubrication Modeling of Newtonian and Shear Thinning Liquids in a Piston-Ring Configuration, Society of Automotive Engineers, Inc., 1997, SAE Technical Paper 972924.

[40] Wolff, A., Piechna, J., Numerical simulation of piston ring pack operation with regard to ring twist effects, The Archive of Mechanical Engineering, Vol. LIV, No. 1, pp. 65-99, Warsaw 2007.

[41] Federal Mogul, *Optimization of piston ring dynamics by direct 3D analysis of dynamic effects* [online]. 2009, [cit. 2014-04-15]. Available at URL: <`http://www.federalmogul.com/en-US/Media/Documents/18AachenerKolloqium_FM3D.pdf`>.

[42] Chen, S., Flynn, P., Development of a Single Cylinder Compression Ignition Research Engine, Society of Automotive Engineers, Inc., 1965, SAE Technical Paper 650733.

[43] Pipitone, E., A New Simple Friction Model for S. I. Engine, Society of Automotive Engineers, Inc., 2009, SAE Technical Paper 2009-01-1984.

[44] KISTLER, *ThermoCOMP ®Quartz Pressure Sensor* [online]. 2014, [cit. 2014-05-02]. Available at URL: <`http://www.intertechnology.com/Kistler/pdfs/Pressure_Model_6125B.pdf`>.

[45] Sandoval, D., An Improved Friction Model For Spark Ignition Engines. Bachelor's thesis, Massachusetts Institute of Technology, 2002.

[46] Chochulowski, C., Simulationsrechnung der Kolbensekundarbewegung. Ph.D. Thesis,Technische Universität München, München, 1985.

[47] Nilsson, Y., Eriksson, L., Determining TDC Position Using Symmetry and Other Methods. Society of Automotive Engineers, Inc., 2004, SAE Technical Paper 2004-01-1458. [ISSN 0148-7191]

[48] Pipitone, E., Beccari, A., Beccari, S., The Experimental Validation of a New Thermodynamic Method for TDC Determination. Society of Automotive Engineers, Inc., 2007, SAE Technical Paper 2007-24-0052. [ISSN 0148-7191]

[49] Pipitone, E., Beccari, A., Beccari, S., Reliable TDC position determination: a comparison of different thermodynamic methods through experimental data and simulations. Society of Automotive Engineers, Inc., 2008, SAE Technical Paper 2008-36-0059.

[50] Sethu, Ch., Leustek, M., Bohac, S., Filipi, Z., Assianis, D., An Investigation in Measuring Crank Angle Resolved In-Cylinder Engine Friction Using Instantaneous IMEP Method. Society of Automotive Engineers, Inc., 2007, SAE Technical Paper 2007-01-3989.

[51] Fuente, D., Friction Measurements of Sleeve Valve Engine in the Piston/Sleeve Interfaces. MSc Thesis, Cranfield University, 2009.

[52] Rai, H. S., Brunt, M. F., Loader C. P., Quantification and Reduction of IMEP Errors Resulting from Pressure Transducer Thermal Shock in an S.I. Engine, Society of Automotive Engineers, Inc., 1999, SAE Technical Paper 1999-01-1329.

[53] Isarai, R., Sugino, M., Moritsugu, M., Kato, N., Nakamura, M., Strain and Motion Measurement for Piston, Piston Ring and Connecting Rod of High Speed Running Engines using New Digital Telemeter. Society of Automotive Engineers, Inc., 2008, SAE Technical Paper 2008-01-1042. [ISSN 0148-7191]

[54] Sonthalia, A., Kumar, C. R., The Effect of Compression Ring Profile on the Friction Force in an Internal Combustion Engine, Tribology in Industry, Vol. 35, No. 1, pp. 74-83, 2013.

[55] Kai Liao, Yang Liu, Dallwoo Kim, Paulo Urzua, Tian Tian, Practical challenges in determining piston ring friction, Proceedings of the Institution of Mechanical Engineers, Part J: Journal of Engineering Tribology, February 2013, vol. 227, no. 2, pp. 112-125.

[56] Kim, K., Godward, T., Takiguchi, M., Aoki., S., Part 2: The Effects of Lubricating Oil Film Thickness Distribution on Gasoline Engine Piston Friction, Society of Automotive Engineers, Inc., 2007, SAE Technical Paper 2007-01-1247.

[57] Macek, J., Fuente, D., and Emrich, M., A Simple Physical Model of ICE Mechanical Losses, Society of Automotive Engineers, Inc., 2011, SAE Technical Paper 2011-01-0610.

[58] Timoshenko, S. P., Gere, J. M., Mechanics of Materials. Third SI edition. London: Chapman & Hall, 1991. 807 p. [ISBN 0-412-36880-3]

[59] Robert Hooke, De Potentia restitutiva, London, 1678.

[60] Gavin, H. P., *Structural Element Sti?ness and Mass Matrices* [online]. 2014, [cit. 2014-04-25]. Available at URL: <`http://people.duke.edu/~hpgavin/cee541/StructuralElements.pdf`>.

[61] MSC Software. MSC. ADAMS/View 2013r2. [User's manual], 2013.

[62] Vlasov, V. Z., Tenkostěnné pružné pruty. 1. vyd. Praha: SNTL, 1962. 569 s.

LIST OF SYMBOLS, PHYSICAL CONSTANTS AND ABBREVIATIONS

$ATDC$	After Top Dead Center
BDC	Bottom Dead Center
$BMEP$	Brake Mean Effective Pressure
CAD	Crank Angle Degree
CNG	Compressed Natural Gas
DOF	Degree of Freedom
FEM	Finite Element Method
FLE	Floating Liner Engine
$FMEP$	Friction Mean Effective Pressure
IES	Instantaneous Engine Speed
$IMEP$	Indicated Mean Effective Pressure
MAP	Manifold Absolute Pressure
MBS	MultiBody System
RMS	Root Mean Square
SI	Spark Ignited
TDC	Top Dead Center
WOT	Wide Open Throttle

a, b, c	angles of rotation, deg
A	cross sectional area, m^2
a, b, c, A, B, C, D	constants for Chenn & Flynn model
A_E	efficient area, m^2
a	acceleration, ms^{-2}
b	radial piston ring wall thickness, m
C	coefficient of friction
d	nominal diamater, m
e	Euler's number
E	modulus of elasticity, Pa
$E*$	reduced modulus of elasticity, Pa
$f_{S,y},\ f_{S,z}$	form factor for shear
F_a	asperity contact force, N
$F_{a,P3},\ F_{a,P5}$	gas pressure force in axial direction, N
F_{fa}	asperity contact friction force, N
F_{fh}	viscous friction force, N

F_{fM}	mixed lubrication friction force, N
F_g	blow-by gas force, N
F_h	hydrodynamic force, N
F_i	inertia force, N
F_M	mixed lubrication force, N
F_N	normal force, N
$F_{r,P3}$	gas pressure force in radial direction, N
F_t	pretension or tangential force, N
F_x	axial force, N
F_y	transverse load, N
G	shear modulus, Pa
h	axial width or nominal film thickness, m
h_{min}	minimal film thickness, m
$\bar{h_T}$	averaged film thickness, m
i	imaginary unit
$I_y,\ I_z,\ J$	cross section moment of inertia, m^4
I_p	polar moment of inertia, m^4
k	conformability coefficient
$\mathbf{K}$	stiffness matrix
K_{11}	tensional stiffness, Nm^{-1}
$K_{22},\ K_{26},\ K_{62},\ K_{66},$ $K_{33},\ K_{35},\ K_{53},\ K_{55}$	bending stiffness
K_{44}	torsional stiffness, $Nrad^{-1}$
l	rod or beam length, m
l_z	cross section dimension in z direction, m
m	total free gap, m
$\dot{m}$	mass flow, kgs^{-1}
$\mathbf{M}$	mass matrix
M_i	inertia moment, Nm
M_k	torsion from piston ring installation, Nm
M_x	torque, Nm
M_z	bending moment, Nm
M_T	engine torque, Nm
n	rotational speed or segment count, rpm
N	axial force, N
O	ring ovality parameter, m
p	contact pressure, Pa
$\bar{p}$	mean hydrodynamic pressure, Pa
P	nominal pressure, Pa

p_{max}	in-cylinder maximum pressure, Pa
Q_z	first moment of cross section area, m^3
r	half of the stroke, m
R	gas constant, $Jkg^{-1}K^{-1}$
s	displacement, m
So	Sommerfeld number
t	time, sec
T	torque or temperature, Nm or K
u	instantaneous velocity, ms^{-1}
u, v, w	deflections, m
$\mathbf{U}$	displacement, m
$\dot{\mathbf{U}}$	velocity, ms^{-1}
$\ddot{\mathbf{U}}$	acceleration, ms^{-2}
$\mathbf{U_0}$	displacement amplitude, m
v	velocity, ms^{-1}
V_1	volume of one engine cylinder, m^3
V_y, V_z	shear force, N
x	number of cylinders
x_a, x_c	piston ring gap opening, m
α	crank angle degree, rad
β	radius asperity summit or torsion coefficient, m
$\delta_1,\ \delta_2$	local film roughness of surface
η	dynamic viscosity, Pas
η	surface density of asperity peaks, m
γ	surface pattern parameter
λ	half of stroke to rod ratio
μ	Poisson's ratio
ω	angular speed, $rads^{-1}$
$\phi_{fp},\ \phi_{fs}$	shear stress factor
ϕ_s	shear factor
ϕ_x	flow factor
ρ	density, kgm^{-3}
σ	compoisite root mean square roughness, m
σ_S	composite summit height standard deviation, m
τ	shear stress, Pa